STUDY OF TUNGSTEN NANOWIRES GROWN BY FIELD EMISSON INDUCED METHOD

YOU GUO FENG

(M. Eng. *NTU*)

A THESIS SUBMITTED

FOR THE DEGREE OF DOCTOR OF PHILOSOPHY

DEPARTMENT OF ELECTRICAL AND COMPUTER ENGINEERING

NATIONAL UNIVERSITY OF SINGAPORE

2010

Acknowledgement

First of all, I would like to express my gratitude to my supervisor Associate Professor John Thong Thiam Leong for his constant guidance, encouragement and especially his hare brained ideas. For without them, all this work would not have materialized.

I would like to thank Professor Andrew Wee for his passion and support to this project. I would also like to thank Assoc. Prof. Gong Hao for valuable discussion and significant contribution to *in situ* TEM experiment. Prof. Eugen Rabkin from Technion, Israel has also contributed to helping me analyzing the grain grooving mechanism.

Thanks are also due to all the staff and students in CICFAR lab for their helps, supports and fruitful discussions. In particluar, I would like to thank Mrs. Ho Chiow Mooi, Mr. Koo Chee Keong, Dr. Oon Chin Hin, Dr. Yeong Kuan Song, Dr. Hao Yu Feng, Mr. Wang Lei, Mr. Khong Siong Hee.

Most imporatantly I would like to thank my wife for her unwavering support all the time.

Table of Content

Summary

This thesis concerns tungsten nanowires grown by the field-emission-induced growth technique. The method allows individual nanowires to be grown at intended locations, and has the potential for nanowiring of nanodevices. The objective of the current work is to study the nanowire properties such as structural morphology and electrical resistivity.

From transmission electron microscope (TEM) imaging, the nanowires are polycrystalline and contain grains of variable sizes depending on the nanowire diameter. 4-terminal current-voltage measurements of nanowires of diameters ranging from 10 to 50nm show size effects in which the resistivity is much higher than that of bulk tungsten due to enhanced electron scattering at both nanowire surface and grain boundaries. Analyses of the experimental results reveal grain boundary scattering to be the dominant contributor to increased resistivity.

Morphology studies conducted *in situ* in the TEM show the processes of grain growth and grain grooving in nanowires as a result of annealing. The polycrystalline tungsten nanowires transform to bamboo-like structure, with transversal grain boundaries normal to the nanowire axis, at particular temperatures which depend on the nanowire diameter. As a result of grain grooving, a bamboo-like nanowire eventually breaks up at developed grain grooves, giving rise to a form of morphological instability peculiar to polycrystalline nanowires at elevated temperatures. We also experimentally identified that breakage occurs at grains with a larger initial aspect ratio of grain length to grain diameter of about 3, which is in good

agreement with theoretical predictions based on the kinetic process of atomic diffusion at the grain surface. In addition, we propose a methodology to estimate the surface diffusion coefficient of one-dimensional nanowires structure.

By overcoating a carbonaceous layer onto the nanowire surface, the grain grooving process in the tungsten-carbon core-shell structure can be prevented due to inhibition of surface diffusion. As a result, the morphology stability of nanowire can be improved, and the nanowire can sustain considerably higher current density and temperature arising from Joule heating, until another form of instability takes place, finally leading to nanowire failure by electromigration.

Oxidation of polycrystalline tungsten nanowire was carried out by heating in a low-pressure oxygen environment. The oxidation is shown to be kinetically limited and the metallic core is seen to shrink to an asymptotically small diameter, arising from accumulated stress in oxide. Theoretical analysis suggests that this self-limited oxidation mechanism is mainly due to a reduction of the oxidation rate by the compressive stress at tungsten/oxide interface.

The results from this project provide useful directions for further explorative studies on the application of polycrystalline metallic nanowires.

Nomenclature

AAO: Anodic Aluminum Oxide

BF: Bright Field Image

CVD: Chemical Vapor Deposition

DF: Dark Field Image

EBL: Electron Beam Lithography

EDX: Energy Dispersive X-ray Spectrum

EELS: Electron Energy Loss Spectroscopy

FEIG: Field Emission Induced Growth

FIB: Focus Ion Beam

MBE: Molecular Beam Epitaxy

MT: Melting Point

MTTF: Median Time to Electromigration-Induced Failure

PECVD: Plasma Enhanced Chemical Vapor Deposition

RIE: Reactive Ion Etching

SAED: Selected Area Electron Diffraction

SADP: Selected Area Diffraction Pattern

SEM: Scanning Electron Microscopy

SMU: Source Measurement Unit

TEM: Transmission Electron Microscopy

VLS: Vapor Liquid Solid

VSS: vapor-solid-solid

List of Tables

List of Figures

Chapter 1 Introduction

1.1 Background

Nanostructured materials have attracted much interest as the results of their peculiar and fascinating properties. Their unique electrical, optical, and thermal properties are the results of the restrictions imposed on the movement of electrons, and therefore nanostructure materials can be classified according to the degrees of freedom for the electrons: 2D (nanofilm), 1D (nanowires, nanotubes, nanorods) and 0D (quantum dots). Among different nanostructures, one-dimensional nanostructures, have become the focus of intensive research owing to their unique properties in studying mesoscopic physics and in fabricating nanoscale devices [Nalwa 2000]. In the past decade, a lot of investigations in fabrications and applications of nanowires have been carried out [Xia 2003]. Although semiconductor nanowires and carbon nanotubes have captured most of attention in the nanowire research community, metallic nanowires nevertheless play a very important role in nanoscale electronic devices as interconnects [Wang 2001, Lieber 2007].

An extensive array of techniques has been developed for synthesizing metallic nanowires. However most of techniques normally produce a large amount of randomly distributed nanowires on the substrate. To make nanowire interconnects, additional techniques are generally required to assemble the nanowires on pre-fabricated electrodes. As such, the fabrication of nanowire interconnects is complicated and it is thus desirable to explore alternative techniques.

On the other hand, as electrical interconnects, a good understanding of the electrical properties of nanowires is essential. In fact, as a consequence of diameter

scaling down to nanometer levels, the electrical properties of metallic nanowires are quite different from those of their bulk counterparts. Therefore, in addition to the development of techniques for fabricating nanowire interconnects, a number of studies have also been conducted on the electrical characteristics of metallic nanowires [Walter 2002, Kim 2006]. However, for the specific example of tungsten nanowire of diameter in the range of 10-50 nm, which is the subject of study in this thesis, to best of our knowledge, the electrical properties of this nanowire have not been carefully studied.

Moreover, the demands of metallic nanowires for use as interconnects raise reliability issues since nanowire interconnects have to meet the challenge of handling increasing current density that can cause significant temperature rise as a result of Joule heating, and hence accelerate failure. One of the reliability issues for metallic nanowire interconnects is associated with the failure caused by electromigration manifested in the form of voids or hillocks which arise as a result of momentum transfer between the electron wind and the diffusing metal atoms [Ho 1989]. This mass transport, in principle, takes place along different diffusion paths, such as the lattice, grain boundaries, and surfaces, which all have distinct electromigration activation energies [Hu 1999, Lloyd 1999]. It is widely accepted that electromigration failure is much more serious in polycrystalline wires than in their single-crystal counterparts due to the additional presence of grain boundary diffusion [Pascoli 2000]. On the other hand, another important reliability issue of cylindrical crystal nanowires originates from Rayleigh instability [Rayleigh 1878], where a single crystalline nanowire breaks into isolated sections at temperatures much lower than the melting point [Sun 2003]. Therefore, it is important to understand the nanowire structural morphology before addressing the reliability issues faced by nanowire interconnects.

Moreover, polycrystalline metallic nanowires always contain grains and grain boundaries that possess large excess free energy, which provides a significant driving force for grain boundary diffusion leading to phase transitions and grain growth [Fecht 1990]. Therefore, polycrystalline metallic nanowires have a strong tendency to transform into a typical configuration with coarser grain size and fewer interfaces at elevated temperature [Klement 1995]. Such structural transformation may also introduce an additional factor that can cause nanowires to fail at high current densities. However, at the present time, studies in the structural transformation in polycrystalline nanowires have been mainly based on theoretical predictions and lack supporting experimental evidence.

1.2 Motivation and Thesis outline

Based on the motivation of using metallic tungsten nanowires as nanoscale interconnects, this thesis focuses on several important aspects, including growth of nanowire, fabrication of interconnects, structural and electrical behavior, and structural transformation of tungsten nanowires.

The thesis consists of six chapters. In chapter 2, some important growth techniques and strategies for the fabrication of nanowires are reviewed with a focus on metallic and tungsten nanowires.

For realizing nanowire interconnects, the technique should demonstrate the ability to grow nanowires of controllable dimensions and material composition, assemble nanowires to the desired location, as well make a good electrical contact to another electrode in the wiring hierarchy. Thus Chapter 3 provides detailed experimental procedures for the growth of tungsten nanowires in tungsten carbonyl ambient through a field-emission induced growth (FEIG) method. Using this method, site-

specific growth of tungsten nanowires can be achieved so that the nanowires are directly grown on the patterned electrode. The morphologies of the as-grown tungsten nanowires are studied via Transmission Electron Microscopy (TEM) methods. Bright-field and dark-field imaging, and electron diffraction are carried out for nanowires of different diameters. In order to make ohmic contacts between the nanowire and an electrode, the Focused Ion Beam (FIB) deposition technique is used in the project. The electrical resistivity is also measured and analyzed.

Since high current density may cause an increase in temperature in nanowire interconnects, structural transformation in nanowires can take place as a result of Joule heating. Therefore Chapter 4 addresses an important issue associated with phase transformation, growth of nanosized grains and migration of atoms in the nanowire at an elevated temperature. In the chapter, structural and morphological changes including grain growth and grain grooving processes are studied in detail through *in situ* observations in the TEM. The experimental results are analyzed based on prior related theoretical work in the literature. In order to improve the reliability of nanowire interconnects, a tungsten-carbon core-shell nanowire is then introduced which shows enhanced current-carrying performance.

If the tungsten nanowire is used in the presence of oxygen, oxidation of the tungsten nanowires is unavoidable, and as a consequence, the formation of tungsten oxides may cause changes in electrical and electronic behaviour. Chapter 5 carefully studies the formation mechanisms of tungsten oxides. Tungsten nanowires are oxidized at temperatures between 400-500°C. The morphology of the oxide is characterized by TEM for different oxidation periods. From the experimental results, the influence of the stress state on the oxidation rate is analyzed based on prior models in the literature.

Concluding remarks on this research are given in Chapter 6 and recommendations for future studies are also provided in this chapter.

Reference

Abudukelimu G., Guisbiers G., and Wautelet M., (2006), *J. Mater. Res.* **21**, 2829.

Fecht H. J., (1990), *Phys. Rev. Lett.* **65**, 610.

Ho P. S., Kwok T., (1989)**,** *Rep. Prog. Phys.* **52**, 301.

Hu C. K., Rosenberg R., Lee K. Y., (1999), *Appl. Phys. Lett.* **74**, 2945.

Huang Q. J., Lilley C. M., Divan R. S., (2009), *Nanotechnology* **20**, 075706.

Kim K., Yoon S. J., and Kim D., (2006), *Optics Express* 14, 12419.

Klement U., Erb U., Sherik A. M. E., Aust K. T., (1995)**,** *Mater. Sci. Eng. A* **203**, 177

Kuan C. C., Chien N. L., Wen W. W., Lih J. C., (2007), *Appl. Phys. Lett.* **90**, 203101.

Lai S. L., Guo J. Y., Petrova V., Ramanath G., and Allen L. H., (1996),*Phys. Rev. Lett.* **77**, 99.

Lieber, C. M. Z. L. Wang, (2007), *MRS Bull.* **32**, 99.

Lloyd J. R., Clemens J., Snede R., (1999), *Microele. Reliab.* **39**, 1595.

Miao L., Bhethanabotla V. R., and Joseph B., (2005), *Phys. Rev. B* **72**, 134109.

Nalwa H. S., (2000), "*Handbook of Nanostructured Materials and Nanotechnology*" ed: Academic Press, New York

Nanda K. K., Sahu S. N., and Behera S. N., (2002),*Phys. Rev. A* **66**, 013208

Rayleigh L.. (1878), *Proc London Math Soc.* **10**, 4.

Sun Y., Mayers B., Xia Y., (2003), *Nano lett.* **3**, 675.

Y. Xia, P. Yang, Y. Sun *et al*., *Advanced Materials* (2003), **15** (5), 353.

Walter E. C., Penner R. M., Liu H., Ng K. H., Zach M. P., and Favier F., (2002), *Surface And Interface Analysis* **34**, 409.

Wang F., and Zhang J., (2001), *J. Appl. Phys*. **89** (7), 3847.

Chapter 2 Literature Review

A significant growth in interest in one-dimensional nanostructures (nanowires, nanotubes, nanorods and the like) could be observed since the discovery of the carbon nanotube (CNT) by Ijima [Ijima 1991]. This discovery led to a huge research effort to grow, characterize, manipulate and utilize CNTs. At the same time, parallel interest in non-carbon nanowires has also emerged. Nanowires can be made out of a variety of materials, which in turn gives them great flexibility in their application.

In this chapter, we will review different approaches to the fabrication of nanowires, focusing on metallic nanowires, and in particular tungsten nanowires which are the main subject this thesis. Related to this, tungsten oxide nanowires will also be reviewed towards the end of this chapter.

2.1 Fabrication of nanowires

Nanowires constitute a broad class of one-dimensional (1D) nanostructures at the forefront of nanoscience and nanotechnology [Lieber 2001]. As nanowires can be rationally and predictably synthesized with all key parameters controlled during growth, including chemical composition, diameter, length, doping, growth direction, and possibly surfaces [Cui 2000, Duan 2001], nanowires thus represent one of best defined and controlled classes of nanoscale building blocks [Lieber 2007].

Different techniques have been developed to synthesize nanowires with predictable control over the key structural, chemical, and physical properties. Examples include laser ablation, chemical vapor deposition, vapor-liquid-solid (VLS) growth, vapor-solid growth, template-assisted growth and size reduction methods, and so on [Xia 2003, Lu 2006].

For the growth of semiconducting nanowire, growth via the VLS mechanism is highly popular. Since the original proposal by Wagner *et al.* [Wagner 1964], the VLS growth mechanism has been re-examined and various synthesis approaches developed over past two decades by Lieber [Yang 1996, Morales 1998], Yang [Wu 2001], and Samuelson [Björk 2002] among many other groups. In VLS growth, the metal nanoclusters (acting as catalysts) are heated to above the eutectic temperature for the metal–semiconductor system of choice in the presence of a vapor-phase source of the semiconductor, resulting in a liquid droplet of the metal/semiconductor alloy. The continued feeding of the semiconductor reactant into the liquid droplet supersaturates the eutectic, leading to nucleation of the solid semiconductor. The solid–liquid interface forms the growth interface, which acts as a sink causing the continued semiconductor incorporation into the lattice and, thereby, the growth of the nanowire with the droplet riding on the top. The gaseous semiconductor reactants can be generated through decomposition of precursors in a chemical vapor deposition (CVD) process or through momentum and energy transfer methods such as pulsed laser ablation [Morales 1998] or molecular beam epitaxy (MBE) [Liu 1999] from solid targets. Thus a broad range of semiconductor nanowires with diameters of only a few to a few tens of nanometres can be produced through this way – for example, Si [Sunkara, 2001], Ge [Wu 2000], GaN [Chen 2001], InAs [Martensson 2007], CdS [Barrelet 2003] and others [Radovanovic 2005, Johansson 2006]. Moreover, the VLS synthesis approach allows the formation of heterostructures at the individual device level in a controlled fashion. Heterostructured nanowires could be realized in either axial or radial configurations [Gudiksen 2002]. These novel hetrostructured nanowires have been used as functional components in transistors [Zheng 2004, Li 2006],

photovoltaic devices [Kempa 2008, Tian 2007, Leiber 2008], and light emitting devices [Qian 2004, 2005, Konenkamp 2004].

Although semiconducting nanowires dominate the literature alongside carbon nanotubes, metallic nanowires have also attracted considerable attention in past ten years because of their novel physical properties and potential application as interconnects in nanoscale electronics. There are several methods for preparing metallic nanowires with controlled length and diameter.

Top-down approaches, which include ion-beam and electron beam nano-lithographic patterning, represent a classic means to realize metallic nanowires with controllable diameter and length [Chou 1994; Hehn 1995; Cerrina 1996; Matsui 1996; Wu 1998]. However the main drawback serial patterning methods is the relatively slow process involved thereby rendering such approaches expensive and unsuitable for large-scale production in practice.

Another novel approach for fabrication of metallic nanowires with the diameter down to few tens of nanometers is through self-assembly of nanoparticles or by external manipulation of nanoparticles with a field (such as electric field), For example, Wyrwa *et al.* demonstrated that gold nanoparticles self-assemble into chains that could be subsequently fused into bundles in solution [Wyrwa 2002]. Hermanson and co-workers showed that metallic nanoparticles suspended in a liquid medium could be assembled into nanowires via dielectrophoresis [Hermanson 2001]. In their approach, mobility and attractive interaction between nanoparticles were induced by an alternating electric field.

However, the most published approach is to use porous membrane as a template, pioneered by Martin's group [Foss 1992, Martin 1994, 1996, 1999 Sapp 1999,

Hulteen 1997] and others [Preston 1993, Whitney1993]. With this technique, metallic nanowires are synthesized by depositing metal into nanosized pores in the membrane followed by removal of the membrane [Wang 2003].

Various types of porous membranes have been used including molecular sieves [Ozin 1992], track-etched polymer [Martin 1994], nanochannel-array glass [Tonucci 1992], and radiation track-etched mica [Possin 1970]. However, one of the most commonly used templates is the anodic aluminum oxide (AAO) membrane which comprises hexagonally ordered pores fabricated via anodization of aluminum foils in an acid medium [Furneaux 1989]. Its popularity stems from the fact that the pore distribution is regular, while its high pore density and high pore aspect ratio can be precisely controlled during the fabrication of the membrane.

The use of templates requires that the material be filled into the pores using a suitable deposition method. Several techniques have been used to fill metal into AAO pores. With the pressure injection technique, low melting-point metal (such as Bi, Sn [Zhang 1998]) are melted and injected into the pores through the application of high pressure. Physical and chemical vapor deposition techniques are often employed for pore filling and fabricating nanowires. For example, Bi nanowires in AAO template have been synthesized by introducing Bi vapor into the pores of the AAO template, which is then solidified by cooling [Heremans 2000]. In another approach, nanowires can be synthesized by filling the template with colloidal dispersions that are usually prepared through sol-gel techniques. The porous template is placed in a stable sol for an appropriate length of time to drive the sol into the pores by capillary forces [Lakshimi 1997].

Electrochemical deposition is regarded as the most popular method for pore filling with metals to obtain continuous arrays of metallic nanowires with its

advantages of simplicity, low cost and high yield. A variety of metallic nanowires with diameter in the range of a few tens of nanometers have been synthesized by this route (e.g. Au [Zhang 2001b], Ag [Sauer 2002], Cu [Gao 2002], Fe [Peng 2000], Co [Zeng 2000], Ni [Nielsch 2001], Bi [Yin 2001] and so on [Sellmyer2001]). Although nanowires prepared are usually polycrystalline, single-crystalline nanowires have also been obtained under carefully-controlled conditions. For example, single-crystalline nanowires of low melting-point metal (e.g. Au [Tian 2003], Cu [Molares 2001], Bi [Zhang 2002]) and later high-melting point metal (such as Ni, Co [Pan 2005]) can be synthesized if a low electrodeposition overpotential is used during deposition. Tian *et al.* [Tian 2003] attributed the growth of single-crystalline nanowire to a mechanism based on 2D-like nucleation: it is considered that the crystalline nanowires are favorably grown under conditions of a larger critical dimension (N_c) of nucleus size, [Paunovic 1998] which can be increased by lowering the overpotential of electrochemical deposition.

It is worth mentioning that CNT with at least one end opened could also be used as a template to fabricate nanowires with small diameters (< 10nm). Molten metal could be filled into the CNT through capillary reaction [Ugarte 1996]. Zhang *et al.*, [Zhang 2000a] evaporated metal onto CNTs to form metallic nanowires of less than 10nm in diameter. Due to the small diameter of CNTs, it is difficult to achieve complete filling, and the filled length is usually limited to a few hundred nanometers [Govindaraj 2000, Zhang 2000b]. More recently, Kitaura *et al*, [Kitaura 2009] reported the preparation of ultra-thin nanowires by simply placing the CNT and metal powder into a glass tube under vacuum with heating. Through this so-called nano-filling reaction, metallic nanowires of low sublimation temperature (e.g. Eu) with

diameters down to only 1-4 atomic chains have been synthesized with a high filling fraction (>80%).

In addition to the porous templating, other forms of templating have been used for the synthesis of nanowires. For example, Pierce *et al.* evaporated the desired metal along step edges on crystals as templates [Pierce 2002]. Penner demonstrated the growth of metal nanowires by templating against the steps present on a highly oriented pyrolytic graphite (HOPG) using eletrodepostion [Penner 2002].

Microstructures or nanostructures themselves could also be exploited as templates to fabricate nanowires of various materials by using evaporation or etching [Madou 1997, Kohler 2003]. For example, Jorritsma *et al*. fabricated metallic nanowires as thin as 15nm by shadow sputtering metal on an array of V-grooves etched on the surface of a Si(100) wafer [Jorritsma 1996]. Sordan *et al.* [Sordan 2001] used vanadium-pentaoxide nanowires as an etch mask on a gold palladium thin film to produce gold-palladium nanowires.

2.2 Electrical properties of metallic nanowires

One of the reasons to continuously study metallic nanowires is raised from unusual behavior compared to bulk material with respect to their physical (electrical, thermal, magnetic, optical, etc.) properties. Here we highlight various features of the electrical properties of metallic nanowires.

1D nanostructures (nanowires) have two confined dimensions and one unconfined dimension. Therefore, the electrical transport property of nanowires may be expected to be different from that of their bulk counterparts. As we known, for macroscopic metallic wires, electrical transport is in the diffusive transport regime, following the classical Ohm's law relationship. However when the wires are small enough

(dimensions comparable to the Fermi wavelength ~Ă) [Costa 1997], then the electrical transport enters into the ballistic transport regime, and the resistance exhibits discrete values due to the quantum confinement of the electronic wave functions by the wire surface. Transport in this regime can be described by the well-established Landauer-Buttiker formalism and the conductance is quantized into integral multiples of $2e^2/h$ [Landuarer 1995, Datta 1995]. Investigations into ballistic type transport are normally observed using fine metallic nanowires or a contact conjunction of wire with diameter of a few atoms [Smith 1996]. For example, Wang *et al.* observed the quantum conductance in Ti nanowire of diameter less than 1nm, which also includes the effect of electronic density of states (DOS) manifested in some discrete peaks [Wang 2001]. Li *et al.* demonstrated quantized conductance in a narrow conjunction point in a Cu wire fabricated by electrochemical etching [Li 1999].

In the mesoscopic size regime, where a nanowire has dimensions of the order of the electron mean free path (~ nm), the electrical transport behavior is between the diffusive and ballistic regimes. In such cases, the electrical resistivity is higher compared to that of the bulk material. Investigation of this size effect dates back to 1938, when Fuchs [Fuchs 1938] derived an expression for the resistivity of a thin film. In his model, the size effect was originally ascribed to diffused scattering at the surface boundaries such as the thin film surface, which essentially imposes a restriction on the mean free path. This is known as the Fuchs-Sondheimer theory (FS theory). Subsequently, after deviations had been observed, an alternative model was proposed by Mayadas and Shatzkes (MS theory) [Mayadas 1969, 1970]. In this model, the enhanced resistivity of thin films is attributed to grain boundary scattering, with a small contribution from surface scattering. Although the FS and MS scattering theories were originally based on thin films, they can also be applied in analyzing the

size effect for nanowires. For example, single- and polycrystalline- Cu nanowires have been studied by Molares *et al*. [Molares 2003]. It was found that at room temperature, the resistivity of Cu nanowires is about 10 times higher than that of bulk Cu. The large value is assumed to be the result of surface size effect. Similar surface size effects have been reported in Mo [Zach 2000], and Pt [Lin 2003]. Durkan *et al.*, [Durkan 2000] observed the size effect in polycrystalline Au nanowires and explained the phenomenon using the MS model, which means that the enhanced resistance of the nanowire is mainly due to the grain boundary scattering. Similarly, Bietsh *et al.* [Bietsch 2002] studied the size and grain-boundary effect of Au wires based on topographic and electrical data provided by conducting AFM metrology.

2.3 Tungsten nanowire and its synthesis

Among different metals, tungsten has a notably high melting point, high evaporation temperature, low sublimation pressure, high resistance to chemical corrosion, and superior mechanical performance [Lassner 1998]. Thus tungsten has a number of applications that exploit its properties. For example, tungsten metal is a good candidate for field emitter [Choi 2002, Umnov 2003], photonic crystals, [Fleming 2002] as an absorbing layer in X-ray mask [Itoh 1991] and is used as a diffusion barrier in semiconductor interconnect structures [Ahn 1987].

The synthesis of tungsten nanowires structures became an interesting research topic since last several years. One approach using a vapor phase technique was reported by Vaddiraju *et al* [Vaddiraju 2003] in which a tungsten filament was heated up to 1750°C in a CVD chamber in O_2 ambient which resulted in bundles of tungsten nanowires of 50nm in diameter at the filament surface. They attributed the growth mechanism to the transportation of tungsten chemical vapor on the filament surface,

in which tungsten vapor is decomposed from tungsten oxide at a higher temperature, (e.g. >1450 °C) leading to nucleation and growth of tungsten nanowires. This technique can also be extended to the synthesis of other transition metallic nanowires such as Cu nanowires [Choi 2004].

Later, Wang *et al* [Wang 2007] reported the synthesis of single crystalline tungsten nanowire by Ni-catalyzed vapor-phase method at much low temperature. With this method, they annealed a mixture of WO_3 and $NiWO_4$ powder at 850°C in a tube furnace with H_2 gas. First, Ni nanoparticles are formed arising from the reduction of $NiWO_4$. The existence of the gaseous $WO_2(OH)_2$ which is produced by the reaction between WO_3 and water vapor provides a vapor-phase source containing the W element. The Ni particle catalysts then promote the preferential decomposition of gaseous $WO_2(OH)_2$ and provide sites on which the growth of single crystalline W nanowire is induced. The synthesis temperature of 850°C is much lower than the eutectic temperature of the Ni-W binary system (1495°C) and the melting point of Ni (1453°C), which means that the growth of W nanowires is governed by the vapor-solid-solid (VSS) mechanism [Kamins 2001].

Compared to above two vapor phase methods by decomposing WO_3 and metal catalyzed-induced VSS growth, another technique for producing tungsten nanowires reported by Lee *et al* [Lee 2002] appears much simpler. In their approach, discrete tungsten nanowires are transformed from a continuous tungsten thin film by directly annealing the sample at 850°C in a CVD chamber with Ar and H_2 gas purge. The nanowires have diameters ranging from 10 to 50nm and showed perfect straightness and well-defined bcc crystalline structure.

Another approach established by Hassel's group [Hassel 2006] involves the fabrication of tungsten nanowire arrays through directional solidification of eutectic

NiAl-W alloy at a solidification temperature of 1700°C [Hassel 2006]. The directional solidification method also allows one to fabricate other kinds of metallic nanowires such as Au, Cu and Mo nanowires [Milenkovic 2006, Brittman 2007, Milenkovic 2009].

2.4 Tungsten oxide nanowire and its synthesis

It is well known that tungsten is a metal which is easily oxidized to tungsten oxide (WO_x) under ambient conditions, and such oxidation in tungsten nanostructure is much outstanding due to a high surface to volume ratio. [Kwon 2004]

Tungsten oxide is intrinsically an n-type semiconductor and has been widely used in many applications. For example, amorphous tungsten oxide films, with transparent characteristics in the visible region owing to a large bandgap of 2.5-3.5 eV, exhibits excellent electrochromic property [Wittingham 1990] and is thus used in display devices or smart windows [Bechinger 1996, Granqvist 1999, Santato, 2001]. Another important application for tungsten oxide is its use in gas sensors [Solis 2001]. Recently, the use of tungsten oxide nanowire for gas sensing has attracted some attention since their gas sensing performance (such as sensitivity and response time) is substantially improved due to the larger surface area [Teoh 2003]. In additional, recent research also found that tungsten oxide nanowires give rise to stable and uniform field emission with a low threshold field [Li 2003, Liu 2005, Zhou 2005],which implies that this material has potential application in field emission and flat panel displays.

Compared to tungsten nanowires, the fabrication of tungsten oxide nanowires seems much easier as they can be obtained by direct thermal treatment of tungsten metal. For example, Zhu *et al* [Zhu 1999] firstly synthesized “tree-like” tungsten

oxide microscale structures by heating a tungsten foil partly covered with a SiO_2 plate in argon atmosphere at 1600°C. Later Liu's group [Gu 2002, Qi 2003] reported their method of preparing tungsten oxide nanowires by directly heating tungsten tips and plates at 700°C in Ar and O_2 environment. Similar methods can be found in numbers of publications. For example, Z. W Liu *et. al*, [Liu 2003] prepared tungsten oxide nanowires by heating tungsten wire wrapped with B_2O_3 at around 1200°C. Hong *et al* produced tungsten oxide nanoribbons with a highly crystalline structured by heating a tungsten plate in water vapor at a much lower temperature of around 650°C [Hong 2005]. Wang *et al* prepared $W_{18}O_{49}$ by oxidizing a sputter-deposited W_2C film, while Zhou *et al* synthesized tungsten oxide nanowire networks by the thermal evaporation of tungsten powders in the presences of oxygen [Zhou 2005].

Unlike the conventional VLS growth for semiconducting nanowires, in which the metal particles are required to serve as eutectic media (catalysts) and size-confined template, in the above experiments, it is accepted that growth of tungsten oxide nanowires follows a vapor-solid growth mechanism [Yang 1997] in which small tungsten oxide particles are initially formed at the substrate and serve as nucleation sites, leading to the anisotropic growth of tungsten oxide nanowires from a tungsten oxide vapor source.

2.5 Assembly of nanowires into device structures

In the above, we have reviewed some important strategies for synthesizing tungsten nanowires and tungsten oxide nanowires. However, most of these approaches often produce nanowires in large quantities that are randomly distributed on the substrate. In addition, to fabricate nanowire-based device, it is desirable to assemble these nanowires into functional and highly integrated material systems at precise locations.

The most popular technique of making connections to such nanowires is by dispersing nanowires on a substrate, followed by lithographic techniques to delineate electrodes to the nanowires [Huang 2001a, Bachtold 2001]. Apart from this general approach, other methods have demonstrated to assembly nanowires on pre-fabricated electrodes, including the use of electric [Smith 2000, Zhang 2001] and magnetic fields [Hangater 2005], laminar flow in microfluidic channels [Huang 2001b, Messer 2000], Langmuir–Blodgett compression [Yang 2003, Tao 2008].

Recently the 3D manipulation technique has become an active area of research in precise positioning to the single nanowire and assembling it onto electrodes. One possible approach is to manipulate nanowire with optical tweezers — tightly focused laser beams capable of holding and moving microscopic dielectric objects in three dimensions [Grier 2003]. A variation of this technique is the use of optoelectronic tweezers [Chiou 2005] addressing individual semiconducting and metallic nanowires with diameters less than 20 nm, through the optically induced dielectrophoresis force. Other approaches can also be found in review works by Alaca *et al* and Lieber *et al*. [Alaca 2009, Lieber 2007]. However, all these manipulation techniques are the post-process of nanowires fabrications.

In this thesis, we will synthesize tungsten nanowires by using a field emission induce growth technique in which a single nanowire can be grown directly at a

specific location so that synthesis and assembly of nanowire can be integrated into one process.

Reference

Ahn K. Y., (1987), *Thin Solid Films* **153**, 469.

Alaca B. E., (2009), *Inter. Mater. Rev.* **5**(21), 2349

Bachtold A., Hadley P., Nakanishi T., Dekker C., (2001), *Science* **294**, 1317.

Barrelet C. J., Wu Y., Bell D. C., & Lieber C. M., (2003), *J. Am. Chem. Soc.* **125,** 11498–11499.

Bechinger C., Wirth E., and Leiderer P., (1996),*J. Appl. Phys.* **68**, 2834.

Björk M. T., Ohlsson B. J., Sass T., Persson A. I., Thelander C., Magnusson M. H., Deppert K., Wallenberg L. R., and Samuelson L., (2002), *Appl. Phys. Lett.* **80,** 1058.

Bietsch A. and Michel B., (2002), *Appl. Phys. Lett.* **80** (18), 3346.

Brittman S., A. Smith J., Milenkovic S., and Hassel A. W., (2007), *Electrochimica Acta*, **53**, 324.

Cahn R. W., (1970), *"Physical Metallurgy"* ed: North Holland Publ. Co., Amsterdam.

Cerrina F., Marrian C., (1996), *MRS Bull.* **21**, 56.

Choi S. H., Wang K. L., Leung M. S., *et. al.*, (2000), *J. Vac. Sci. Technol. A* **18**, 1326.

Choi C. H., Jang Y. T., Ju B. K., Lee Y. H., Oh M. H., Ahn J. H., and Min N. K., (2002), *SID Digest* **3301**, 369.

Choi H., Park S. H., (2004), *J. Am. Chem. Soc.* **126**, 6248.

Chou S. Y., Wei M., Krauss R. P., Fisher B. P. (1994),*J. Vac. Sci. Technol. B* **12,** 3695.

Cimalla V., Rohlig C. C., Pezoldt J., Niebelschutz M., Ambacher O., Bruckner K., Hein *et al.* (2008), *Journal of Nanomaterials***V2008**, 638947.

Costa K. J. L., Garcia N. and Olin H., (1997), *Phys. Rev. Lett*. **78**, 4990.

Cotterill P., and Mould P. R., (1976), *"Recrystallization and grain growth in metals"* ed: *Surrey University Press*, IBSN 0903384

Cui Y., Duan X., Hu J., and Lieber C.M., (2000), *J. Phys. Chem. B* **104,** 5213.

Datta S., (1995) "*Electronic Transport in Mesoscopic System"* ed: Cambridge University Press.

Duan X. and Lieber C.M., (2001), *Adv. Mater.* **12**, 298.

Durkan A. and Welland M. E., (2000),*Phys. Rev. B.* **61**(20), 14215.

Fleming J. G., Lin Kady S. Y., I. E., Biswas R., and Ho K. M., (2002), *Nature* **417**, 52.

Foss C. A., Tierney M. J., Martin C. R., (1992), *J. Phys. Chem*. **96**, 9001.

Fuchs K., (1938), *Proc. Cambridge Philos. Soc.* **34**, 100.

Funahashi R., Matsubara I., Shikano M., (2001), *Chem. Mater*. **13**, 4473.

Furneaux R. C., Rigby W. R., Davidson A. P., (1989), *Nature* **337**, 147.

Gao T., Meng G. W., Wang Y. W., Sun S. H., Zhang L. D., (2002**)**, *J. Phys.: Condens. Matter.* **14,** 355.

Govindaraj A., Satishkumar B.C., Nath M., Rao C.N.R., (2000), *Chem. Mater.* **12**, 202.

Granqvist C. G., (1999), *Electrochim. Acata.* **44**, 3165.

Gu G., Zheng B., Han W. Q., Roth S., Liu J., (2002), *Nanoletters* **2**, 849.

Gudiksen M. S., Lauhon L. J., Wang J., Smith D. C., and Lieber C. M., (2002), *Nature,* **415,** 617.

Hangater C. M., Myung N. V., (2005), *Chem. Mater.* **17**, 1320.

Hassel A. W., Smith A. J., Milenkovic S., (2006), *Electrochimica Acta*. **52**(4), 1799.

Hehn M., Ounadjela K., Bucher J., Rousseaux F., Deeanini D., Bartenlian B., Chappert C., (1995), *Science* **272**, 1782.

Heremans J., Thrush C. M., Lin Y. M., Cronin S., Zhang Z., Dresselhaus M. S., Mansfield J. F., (2000), *Phys. Rev. B*, **61**, 2921.

Hermanson K. D., Lumsdon S.O., Williams J.P., Kaler E.W., Velev O.D., (2001), *Science* **294**, 1082.

Hong K. Q., Yiu W. C., Wu H. S., Gao J. and Xie M. H., (2005), *Nanotechnology* **16**, 1608.

Hu J., Odom T.W., and Lieber C.M., (1999), *Acc.Chem. Res.* **32,** 435.

Huang Y., Duan X., Wei Q., and Leiber C. M., (2001a), *Science* **291**, 630

Huang Y., Duan X., Cui Y., Lauhon J., Kim K.H. and Lieber C.M., (2001b), *Science* **294**, 1313

Hulteen J. C., Martin C.R., (1997), *J. Mater. Chem.* **7**, 1075.

Ijima S., (1991), *Nature* **354,** 56.

Itoh M., Hori M., and Nadahara S., (1991),*J. Vac. Sci. Technol. B* **9**, 149.

Johansson J., *et al.* (2006), *Nature Mater.* **5,** 574–580.

Jorritsma J., Gijs M.A.M., Kerkhof J.M., Stienen J.G.H., *Nanotechnology* (1996), **7**, 263

Kamins T. I., Williams R. S., Basile D.P., Hesjedal T., Harris J. S., (2001), *J. Appl. Phys.* **89**, 1008.

Kempa T. J., Tian B., Kim D., Hu J., Zheng X. and Lieber C. M., (2008), *Nano Lett.* **8**, 3456.

Kitaura R., Nakanishi R., Saito T., Yoshikawa H., Awaga K., Shinohara H., (2009), *Angew. Chem. Int. Ed.* 48, 8298.

Kohler M., Fritzsche W., (2004), "*Nanotechnology"* ed: Wiley-VCH press. Weinheim.

Konenkamp R., Word R.C., Schlegel C., (2004), *Appl. Phys. Lett.* **85**, 6004.

Kwon Y. S., Gromov A. A., Ilyin A. P., Alexander A.D., Kim J. S., Park S. H., Hong M. H., (2004), *International Journal of Refractory Metals and Hard Materials* **22**(6), 235.

Lakshmi B. B., Dorhout P. R., Martin C. R., (1997),*Chem. Mater.* 9, 857.

Landauer R., (1995), *IBM J. Res. Dev.* **1**, 223.

Lassner E., Schubert W. D., (1998), *"Tungsten : properties, chemistry, technology of the elements, alloys, and chemical compounds"* Ed: Plenum Press, New York.

Lee Y. H., Choi C. H., Jang Y. T., Kim E. K., Ju B. K., (2002), *Appl. Phys. Lett.* **81**, 745.

Lee Y. H., Kim D. H., Choi C. H., Jang Y. T., Ju B. K., (2004), *Appl. Phys. Lett.* **85**(24), 5977.

Li C. Z., Bogozi A., Huang W., Tao N. J., (1999), *Nanotechnology* **10**, 221.

Li Y. B., Bando Y., Golberg D., (2003), *Adv. Mater.* **15**, 1294.

Li Y., Xiang J., Qian F., Gradecak S., Wu Y., Yan H., Blom D. A., Lieber C. M., (2006), *Nano Lett.* **6**, 1468.

Lieber C. M., (2001), *Sci. Am.* **285,** 58.

Lieber C. M., Wang Z. L., *et. al* (2007), *MRS BULLETIN* **32**, 99.

Lin J. F. and Bird J. P. *et. al*., (2003), *Appl. Phy. Lett.* **82** (5), 802.

Liu J. L., Cai S. J., Jin G. L., Thomas S. G. and Wang K. L., (1999), *J. Cryst. Growth* **200,** 106.

Liu Z. W., Bando Y. H., Tang C. C., (2003), *Chem. Phys. Lett.* **372**, 179.

Liu J. G., Zhang Z. J., Zhao Y., Su X., Liu S., Wang E. G., (2005), *Small* **1**, 310.

Liu B., Zeng H. C., (2004), *J. Am. Chem. Soc.* **126**, 8124

Lu J. G., Chang P. C., Fan Z. Y., (2006), *Materials Science and Engineering R* **52**, 49

Lu W. and Lieber C. M., (2006), *J. Phys. D: Appl. Phys*. **39,** 387.

Martensson T., *et al.* (2007), *Adv. Mater.* **19,** 1801–1806.

Masuda H., Fukuda K., (1995), *Science***268**, 1466.

Martin C. R., (1994), *Science* **266**, 1961.

Martin C. R. (1996),*Chem. Mater.* **8**, 1739.

Martin C. R., Dermody D. J., Reiss B. D., Fang M., Lyon L. A., Natan M. J., Mallouk T. E., (1999), *AdV. Mater*. **11**, 1021.

Matsui S., Ochiai Y., (1996), *Nanotechnology* **7**, 247

Mattern C. R., (1995), *Acc. Chem. Res*. **28**, 61.

Mayadas A. F. and Shatzkes M. *et al,* (1969), *Appl. Phys. Lett.* **14**, 345.

Mayadas A. F. and Shatzkes M., (1970), *Phys. Rev. B.* **1**, 1382.

Messer B., Song J. H., and Yang P., (2000),*J. Am. Chem. Soc.* **122,** 10232.

Milenkovic S., Hassel A. W., and Schneider A., (2006), *Gold Bulletin*. **39**, 185.

Milenkovic S., Smith A. J., and Hassel A. W., (2009), *Journal of Nanoscience and Nanotechnology* **9**, 3411.

Morales A. M., Lieber C. M., (1998), *Science* **279,** 208–211.

Molares M. E. T., Buschmann V., Dobrev D., Neumann R., Scholz R., Schuchert I. U., Vetter J., (2001), *Adv. Mater*. **13**, 62.

Molares M. E. T., (2003), *Appl. Phy. Lett.* **82** (13).

Nielsch K., Wehrspohn R. B., Barthel J., Kirschner J., Gosele U., S. F., Ficher H., Kronmuller, (2001), *Appl. Phys. Lett.* **79**, 1360.

Okuyama F., (1971),*J. Appl. Phys.* **42**, 256.

Okuyama F., (1974),*J. Appl. Phys.* **45** ,4239.

Okuyama F., (1975),*J. Appl. Phys.* **46**, 3255.

Ozin G. A., (1992), *Adv. Mater.* **4**, 612.

Paunovic M., Schlesinger M., (1998), "*Fundamentals of Electrochemical Deposition*" ed: Wiley: New York, pp 108-109.

Peng Y., Zhang H. L., Pan S. L., Li H. L., (2000), *J. Appl. Phys.* **87**, 7405.

Penner R. M., (2002), *J. Phys. Chem. B.* **106**, 3339.

Pierce J. P., Plummer E. W. and Shen J., (2002), *Appl. Phys. Lett.* **81**(10), 1890

Possin G. E., (1970), *Rev. Sci. Instrum.* **41**, 772.

Preston C. K., Moskovits M., (1993), *J. Phys. Chem.* **97**, 8495.

Qi H., Wang C. Y., Liu J., (2003), *Adv. Mater*. **15**, 411.

Qian F., Li Y., Gradecak S., Wang D. L., Barrelet C. J., Lieber C. M., (2004), *NanoLetter* **4**, 1975.

Qian F., Gradecak S., Li Y., Wen C. Y., Lieber C. M., (2005), *NanoLetter* **5**, 2287.

Radovanovic P. V., Barrelet C. J., Gradečak S., Qian F., & Lieber C. M., (2005), *Nano Lett.* **5,** 1407–1411.

Sapp S. A., Mitchell D. T., Martin C. R., (1999), *Chem. Mater*. **11**, 1183.

Sauer G., Brehm G., Schneider S., Nielsch K., Wehrspohn R. B., Choi J., Hofmeister H., Gosele U., (2002), *J. Appl. Phys.* **91**, 3243.

Sellmyer D. J., Zheng M., Skomski R., (2001), *J. Phys.: Condens. Matter.* **13**, R433

Smith C. G. (1996), *Rep. Prog. Phys.* **59,** 235.

Smith P. A., *et al.* (2000), *Appl. Phys. Lett.* **77,** 1399.

Sordan R., Burghard M., Kern K., (2001), *Appl. Phys. Lett.* **79**(13), 2073.

Tao A. R., Huang J., Yang P., (2008),*Acc. Chem. Res.* **41,** 1662.

Teoh L. G., Hung I. M., Shieh J., Lai W. H., and Hon M. H., (2003), *Electrochem. Solid-State Lett.* **6**, G108.

Tian M., Wang J., Kurtz J., Mallouk T. E., Chan M. H. W., (2003), *Nano Lett.* **3**, 919.

Tian B., Zheng X., Kempa T. J., Fang Y., Yu N., Yu G., Huang J. and Lieber C. M., (2007), *Nature* **449**, 885.

Tonucci R. J., Justus B. L., Campillo A. J., Ford C. E., (1992), *Science* **258**, 783.

Trentler T.J., Hickman K.M., Goel S.C., Viano A.M., Gibbons P.C., and Buhro W.E., (1995), *Science* **270,** 1791.

Trentler T.J., Goel S.C., Hickman K.M., Viano A.M., Chiang M.Y., Beatty A.M., Gibbons P.C., and Buhro W.E., (1997), *J. Am. Chem. Soc.* **119,** 2172.

Ugarte D., Chatelain A., Heer W. A. D, (1996), *Science*, **274**, 1897.

Umnov A.G., Shiratori Y., Hiraoka H., (2003),*Appl. Phys. A* **77**, 159.

Vaddiraju S., Chandrasekaran H., Sunkara M. K., (2003), *Journal of the American Chemical Society*. **125**(36), 10792.

Wagner R.S. and Ellis W.C., (1964), *Appl. Phys. Lett.* **4** , 89.

Wang X. F., Zhang J., Shi H. Z., Mang Y. W., Meng G. W., Peng X. S., Zhang L. D., Fang J., (2001), *J. Appl. Phys*. **89**, 3847.

Wang B., Yin S., Wang G. and Zhao J. (2001), *J. Phys.: Condens. Matter*. **13**, L403.

Wang H. H., Han C. Y., Willing G. A., and Xiao Z., (2003), *Materials Research Society Symposium Proceedings* **775**, 107.

Wang S. L., He Y. H., Zou J., Jiang Y., Xu J., Huang B. Y., Liu C. T., Liaw P. K., (2007), *Journal of Crystal Growth* **306**, 433.

Weisbuch C. and Vinter B., (1991), "*Quantum Semiconductor Structures*" ed: Boston: Academic

Whitney T. M., Jiang J. S., Searson P. C., Chien C. L., (1993), *Science* **261**, 1316.

Wittingham M. S., (1990), "*Recent Advances in Fast Ion Conducting Materials and Devices*" Edited by B. V. R. Chowdary, Q. G. Liu, and L. Q. Chen , World Scientific, Singapore,.

Wu W., Cui B., Sun X., Zhang W., Zhuang L., Kong L., Chou S. Y., (1998), *J. Vac. Sci. Technol. B* **16**, 3825.

Wu Y., Yang P., (2000),*Chem. Mater.* **12,** 605–607.

Wu Y., Yang P., (2001), *J. Am. Chem. Soc.* **123,** 3165–3166

Wyrwa D., Beyer N., Schmid G., (2002), *Nanoletters* **2**, 419.

Xia Y., Yang P., Sun Y., Wu Y., Mayers B., Gates B., Yin Y., Kim F., Yan H., (2003), *Adv. Mater*. **15**(5), 353.

Xue D. S., Zhang L. Y., Gui A. B., Xu X. F., (2005), *Appl. Phys. A. Mater. Sci. Process.* **80**, 439.

Yang P. D. and Lieber C.M., (1996), *Science* **273,** 1836.

Yang P. D. and Lieber C. M., (1997), *J. Mater. Res.* **12**,2981.

Yang P. D., (2003), *Nature* **425,** 243.

Yin A. J., Li J., Jian W., Bennett A. J., Xu J. M., (2001), *Appl. Phys. Lett.* **79**, 1039.

Zach P., Ng K. H., and Penner R. M., (2000), *Science* **290**, 2120.

Zeng H., Zheng M., Skomski R., Sellmyer D. J., Liu Y., Menon L., Bandyopadhyay (2000), S., *J. Appl. Phys.* **87**, 4718.

Zhang Z., Ying J. Y. and Dresselhaus M. S., (1998), *J. Mater. Res.* **13**, 1745

Zhang Y. and Dai H., (2000a), *Appl. Phys. Lett.* **77**, 3015.

Zhang Z. L., Li B., Shi Z. J., Gu Z. N., Xue Z. Q., Peng L. M., (2000b), *J. Mater. Res.* **15**, 2568.

Zhang Z., Sun X., Dresselhaus M.S., Ying J.Y.,(2000c), *Phys. Rev. B* **61**, 4850.

Zhang Y., Cheng A., J Cao., Wang Q., Woong K., Li Y., Morris N., Yenilmez E., Kong J., and Dai H., (2001a), *Appl. Phys. Lett.* **79**(19), 3155.

Zhang X. Y., Zhang L. D., Lei Y., L. Zhao X., Mao Y. Q . (2001b), *J. Mater. Chem.* **11**, 1732.

Zhang J., Wang X., Peng X., Zhang L., (2002), *Appl. Phys. A* **75**, 485

Zheng G. F., Lu W., Jin S., Lieber C. M., (2004),*Adv. Mater.* **16**, 1890.

Zhou J., Ding Y., Deng S. Z., Gong Li., Xu N. S., Wang Z .L., (2005), *Adv. Mater.* 17, 2107.

Zhu Y. Q., Hu W., Hsu W. K., Terrones M., Grobert N., Hare J. P., Kroto H. W., Walton D. R. M., Terrones H., (1999**)**, *Chem. Phys. Lett*. **309**, 327.

Chapter 3 Field Emission Induced Growth of Tungsten Nanowire

3.1 Background

One approach to grow conductive nanowires is based on the technique of glow discharge. In the 1970s, Linden *et al.* [Linden 1978] and Neumann *et al.* [Neumann 1980] observed the formation of needles of carbon in a corona discharge involving benzonitrile. Linden *et al.* [Linden 1978] first discovered the formation of W dendritic structures at the cathode area in a glow discharge in tungsten hexacarbonyl ($W(CO)_6$) ambient. A series of similar works were then carried out on the growth of metallic needles by Okuyama's group [Okuyama 1979, 1980a, 1980b, 1982, 1984, 1991] using various metal carbonyls (such as W, Mo and Cr carbonyls). Figure 3.1 shows a typical tungsten needle grown at a room temperature. In these studies, needle structures were deposited on an electron emission pointed cathode. It was also discovered that when the cathode temperature increased from 300K to above 1500K, the shape and the structure of the needles changed from dendritic and polycrystalline needles to straight single crystalline whiskers as shown in Figure 3.2.

The growth mechanism of the wire through glow discharge was proposed by Okuyama *et al.* [Okuyama 1980b]. It was believed that the charged metallic ions were attracted to and deposited on the cathode. It was postulated that when electrons are field-emitted from surface projections on the cathode, these electrons are accelerated by the electric field and finally gained enough energy to dissociate metal carbonyl molecules. The resulting metal ions are attracted towards the field emitting projections, and needles or whisker start to grow axially at the protruding portions of the deposits. As a needle elongated, the field strength at its tip increases, leading to enhanced deposition of metal atoms.

A similar growth mechanism was proposed by Kent *et al.* [Kent 1993], who observed the formation of a nanofilament at the end of a negatively–biased scanning tunneling microscope (STM) tip when it was used for electron beam induced deposition using $Fe(CO)_5$ to form magnetic dots. They suggested that field-induced molecular dissociation contributes to the growth of nanofilament.

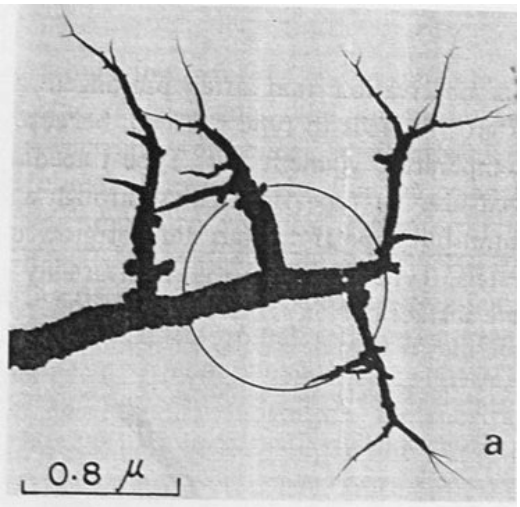

Figure 3.1 TEM micrograph of a typical dendritic needle grown at room temperature [Okuyama 1980b].

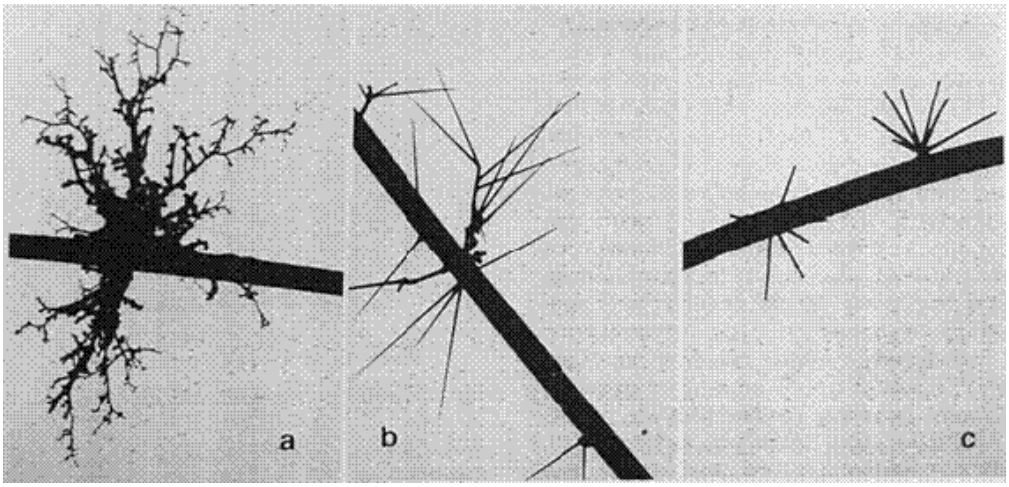

Figure 3.2 TEM micrograph of tungsten microneedles grown on a heating wire at different temperature a) 300K, b) ~1250K and c) ~1500K. For scale, the thickness on the main wire is 10μm [Okuyama 1980b].

3.2 Introduction to Field-Emission Induced Growth

Based on the earlier work by Okuyama *et al*., a controllable method to grow single nanowires was reported by Oon *et al.* [Oon 2002b] and was subsequently called "Field-Emission Induced Growth" (FEIG). By limiting the field emission current, the technique is able to grow individual nanowires up to tens of micrometers long, unlike the glow discharge method where the field emission current is not confined, which results in massive bunches of whiskers

The growth of nanowires is carried out in the chamber of an environmental scanning electron microscope to enable immediate viewing during and after growth. The precursor gas of metal carbonyl is introduced into the chamber through a nozzle. The cathode can be a sharp tungsten tip or tip-like "asperity" on a flat surface which is capable of field emitting under bias between an anode and the cathode. Figure 3.3 shows the basic experimental setup. A feedback control loop to a high voltage supply allows one to maintain constant current operation during nanowire growth.

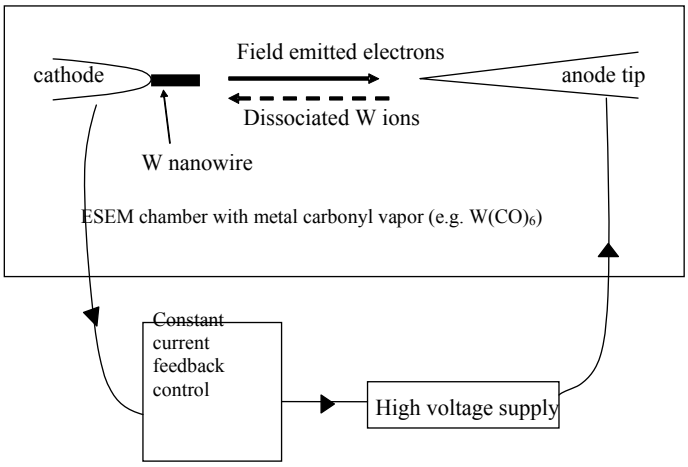

Figure 3.3 Schematic of field-emission induced growth for synthesis of tungsten nanowires.

During nanowire growth, a high voltage of a few hundred volts is applied between the electrodes – this will extract electrons from the grounded cathode through field emission (Figure 3.4). A localized decomposition region will then be formed between the cathode and anode. The proximity of the anode to the cathode, typically between the 1-100 μm, is much less than the mean free path of a few mm for gas molecules at about 0.01mbar. This significantly reduces the likelihood of forming secondary ions and electron avalanches that is characteristic of a glow discharge. In this situation, most of the ions are formed in the decomposition region by direct electron impact from the field-emitted electrons. In the formation of a nanowire through this mechanism, we need to consider the interaction of the field-emitted electron with metal carbonyl molecule, the trajectory of the product of interaction and the processes involved in the deposition and growth of the nanowire.

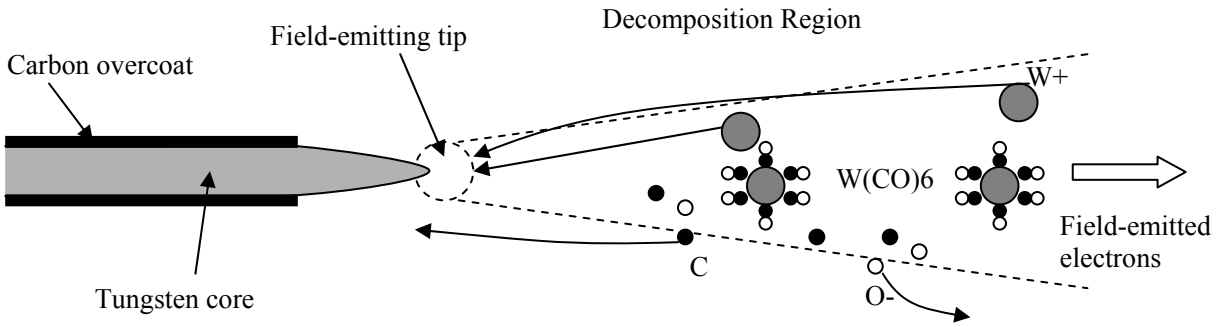

Figure 3.4 Schematic showing the initiation and continual growth of tungsten nanowire at the base tip.

In this region, taking tungsten carbonyl ($W(CO)_6$) as an example, electrons with at least ~8.5eV energy [McDaniel 1964, Cantone 1966] ionize and crack the $W(CO)_6$ molecules, and generate dissociation reactions. The dissociated W^+ ions are attracted back to the field-emitting area of the cathode by electrostatic forces. These W^+ ions are eventually deposited on the sharpest portion on the cathode corresponding to the highest local electrical field. Thus nanowires are formed and the areas of field-

emission are then continually constrained to the nascent sharp tip end of the nanowire (as shown in Figure 3.4). Once the growth starts, the voltage required to maintain the same current will be reduced due to the much smaller tip radius of the growing nanowires. In this manner, the so-called field-emission induced growth of tungsten is sustained and axial nanowire deposition continues.

Three criteria have to be satisfied for the above FEIG mechanism:

1) The electrons that are emitted by the tip must be sufficiently energetic to ionize or crack the precursor involved.
2) The ions that return to the tip must be able to land at the correct destination (the tip of the nanowire). If the ions return and land randomly, a nanowire would not form, but a film would be deposited instead.
3) The ions must land at the correct energy. If the energy of the ion is not suitable, it may bounce off or even sputter the tip instead of depositing on it.

A detailed discussion of these criteria can be found in a paper and thesis by Oon *et al*. [Oon 2002].

Apart from dissociated W^+ ions being created by electron impact, the carbonyl ligands are also believed to be dissociated into CO molecules. These CO molecules undergo further electron dissociation to form C as follows:

$$CO + e^- \rightarrow C + O^- \qquad (3.1)$$

The negatively charged O^- ions will probably be attracted towards the anode and do not influence the growth. The resulting carbon then condenses on the substrate. Since most of the carbon atoms formed are not charged, they are not attracted back by the electrostatic field and focused to the field-emitting tip. However some of C atoms could possibly deposit on the nanowire surface and result in a carbonaceous overcoat (Figure 3.4).

3.3 Direct growth of nanowire on flat surface using FEIG method

The FEIG method was initially used to grow the nanowires on field-emission tips [Oon 2002]. In this project, the technique was extended to grow nanowires on flat substrates. To achieve localized growth of a nanowire on a substrate, several key issues had to be resolved:

1) The electric field has to be localized into the vicinity of the desired site on the substrate. Without localizing the electric field, nanowires would grow on other sharp protrusions on the substrate.
2) A sharp tip has to be created on the substrate to provide a point of initiation of the nanowire. The tip has to be sharp and robust enough to field emit and easily fabricated at the desired site.
3) The nanowire is grown vertically upwards with only one end attached to the substrate (the starting end). The free end (the growing end) has to be attached to another desired site (ending site) on the substrate. For example, this ending site could be a electrode for electrical measurement of the grown nanowire.
4) A gas nozzle should be positioned near to the substrate in order to provide an adequate supply of precursor vapor to the field emission area during nanowire growth.

3.3.1 Experimental Set-up

Based on above requirements, the experimental set up is shown in Figure 3.5 The set up is mounted in a Philips XL30 FEG Environmental Scanning Electron Microscope (ESEM). A sharp electrochemically etched tungsten tip anode is used to localize the electric field to the location where the nanowire is to be grown. The tungsten tip anode is mounted on a Kleindiek Nanotechnik MM3A-EM 3-axis

nanomanipulator. A gas nozzle, close to the substrate die, is used to introduce the precursor gas. Typically the distance between the gas nozzle and substrate die is about 1 mm. SEM imaging is used in positioning the substrate and the anode tip. The anode tip is connected to a Keithley model 237 Source Measurement Unit (SMU) via a 100 MΩ resistor in series. The resistor is used to protect the sensitive electronics of the SMU from damage in the event of an arc discharge. It also helps maintain a constant current while field emitting since an increase in current through the resistor will automatically result in a voltage reduction at the anode.

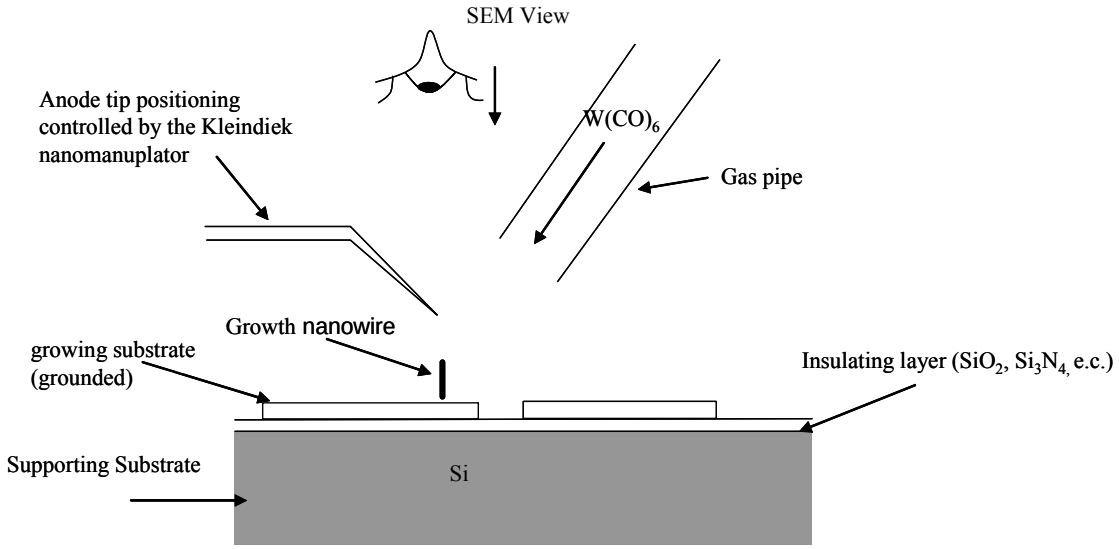

Figure 3.5 Schematic of set-up used for selective growth of nanowires by field emission.

Three kinds of substrate were used in the experiment. The first type, used to grow the nanowire for electrical measurement purpose, is a custom-made (100) Si die with SiO_2 layer (400 nm thick) deposited by plasma enhanced chemical vapor deposition method (PECVD). Gold (100nm) on titanium (10nm) metallization is delineated by electron-beam lithography and lift-off to create electrode patterns on the SiO_2 layer. Au acts as the conducting layer while the Ti is for adhesion between the

Au and Si_3N_4. Gaps between electrodes range from 2 to 10 μm. The nanowire is directly grown over to straddle the electrodes. The die is bonded to a small IC package (24-LCC) and the package is either grounded to an SEM specimen stub via carbon tape or inserted into an IC socket for *in situ* electrical measurements. Figure 3.6 shows a photograph of the set up for growing the nanowire on this die.

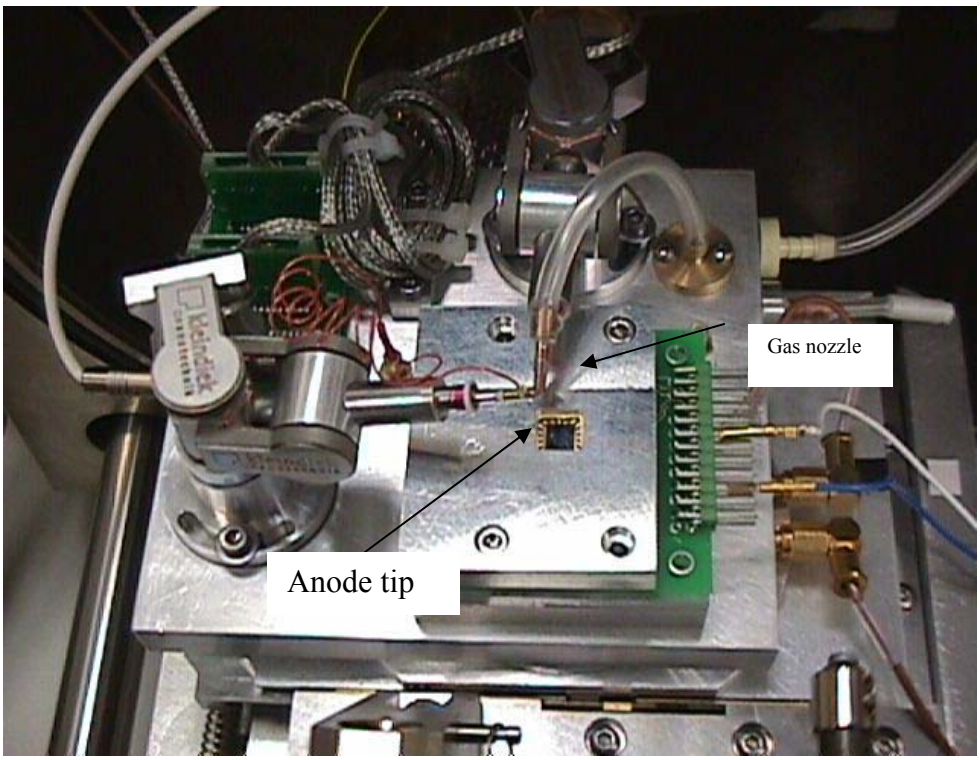

Figure 3.6 Top view of the set-up used for growing nanowire on electrode patterned sample. Two nanomanipulators are used, with the second being used use to position the nozzle.

The second type of substrate is used to grow the nanowire for TEM characterization. It is a copper TEM grid (3 mm diameter, 200 mesh) coated with Quantifoil® holey-carbon membrane (supplied by SPI Supplies Inc.[#]). The nanowires are directly grown on the electrically grounded grid and straddle holes in the carbon membrane.

[#] Detail information of Quantifoil® holey-carbon membrane can be found in company website: http://www.2spi.com/catalog/grids/quantifoil-carbon-films.php

The third is a custom-made silicon die (3×3 mm^2) that fits into the TEM holder. The die was made from a (100) silicon substrate with silicon nitride layers of 50nm deposited by PECVD on both sides (Figure 3.7(a)). Figures 3.7(b)-(f) illustrate the fabrication process. First, a window of about 200μm × 200μm at the center of the back silicon nitride layer was patterned by contact photolithography. The silicon nitride within the window was then removed through reactive ion etching (RIE) using SF_6 as shown in Figures 3.7(b-c). Using anisotropic KOH etching, the exposed Si substrate was etched through, terminating at the top silicon nitride layer, leaving a suspended silicon nitride membrane (100×100 μm^2 in size and 50 nm thickness) as shown in Figure 3.7(d). Finally, electrode patterns were delineated in PMMA resist using electron-beam lithography (EBL), and gold (100nm) on titanium (10nm) (Au/Ti) metallization evaporated and lifted-off as shown in Figures 3.7 (e)-(f), to form bond pads at the die periphery with electrodes leading into the vicinity of the suspended nitride membrane. Figure 3.8 shows an optical micrograph of the TEM die with silicon nitride membrane in the center (outlined by a dashed line) and nearby Au/Ti electrodes. The design of such silicon die had already been applied in structural and electrical studies for some 1D nanostructures. (e.g. Au nanowires [Xu 2006], CNT [Mølhave 2006]) In this work, the die is used to grow tungsten nanowires for both TEM characterization and electrical transport measurement.

The Au/Ti electrodes serve a dual purpose. For the FEIG growth process, one grounded electrode (cathode) is needed from which the nanowire grows. In addition, this Au/Ti electrode in combination with other electrodes allow 2- or 4-point electrical measurements to be performed, as the nanowire is directed to grow over and straddle the parallel Au/Ti electrodes as shown in the inset image in Figure 3.8. Prior to FEIG nanowire growth, a focused ion beam (FIB) was used to sputter-etch several through-

slots of approximately 5µm width in the membrane as shown in the inset image in Figure 3.8. These slots allow un-obscured imaging of the straddling nanowires by the TEM electron beam.

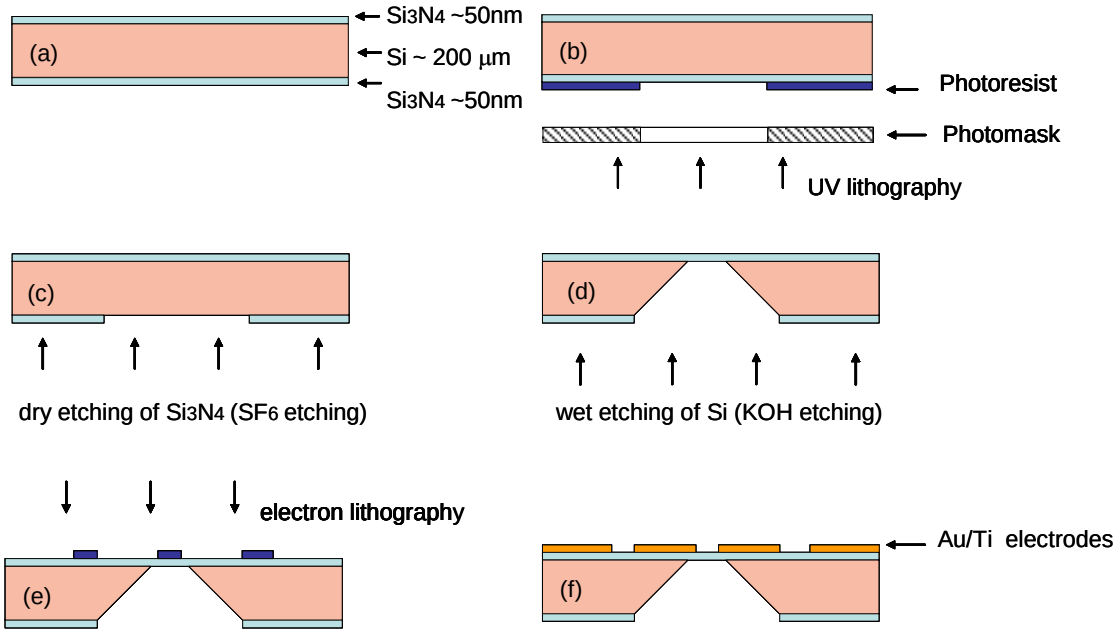

Figure 3.7 Schematic of the fabrication process for TEM membrane sample

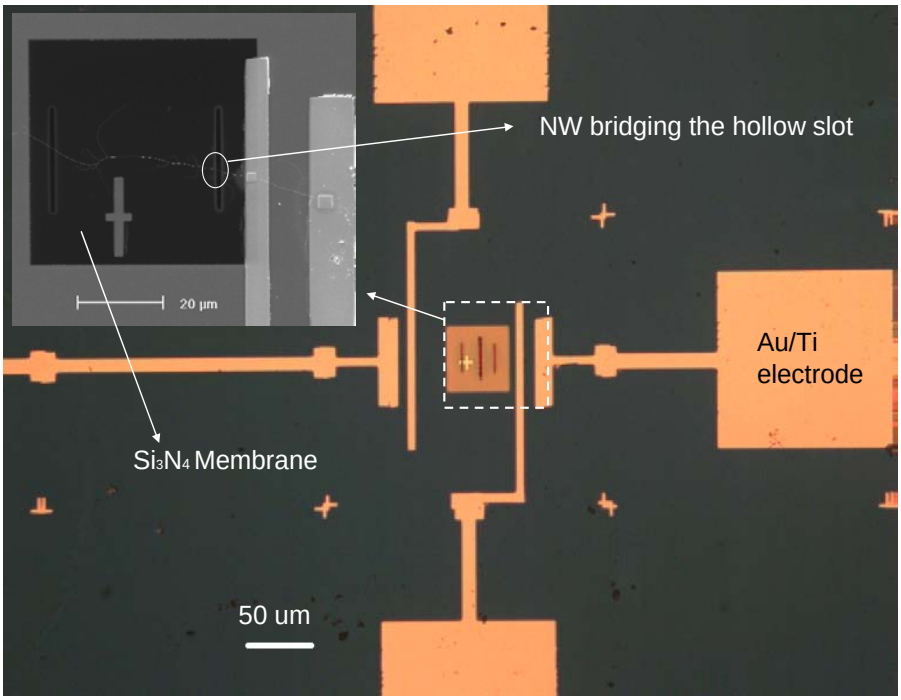

Figure 3.8 Micrographs of prepared TEM sample coated with electrode patterns. Inset SEM image shows nanowire grown on top of the Si_3N_4 membrane

Figure 3.9 shows the set up for growing the nanowire on copper grid, which is grounded to the SEM stube via carbon tape. Alternatively, for the silicon nitride membrane TEM die, grounding is achieved by using a grounded tip positioned by another nanomanipulator. The gas nozzle is fixed on the SEM specimen stub within 1mm of the growth area.

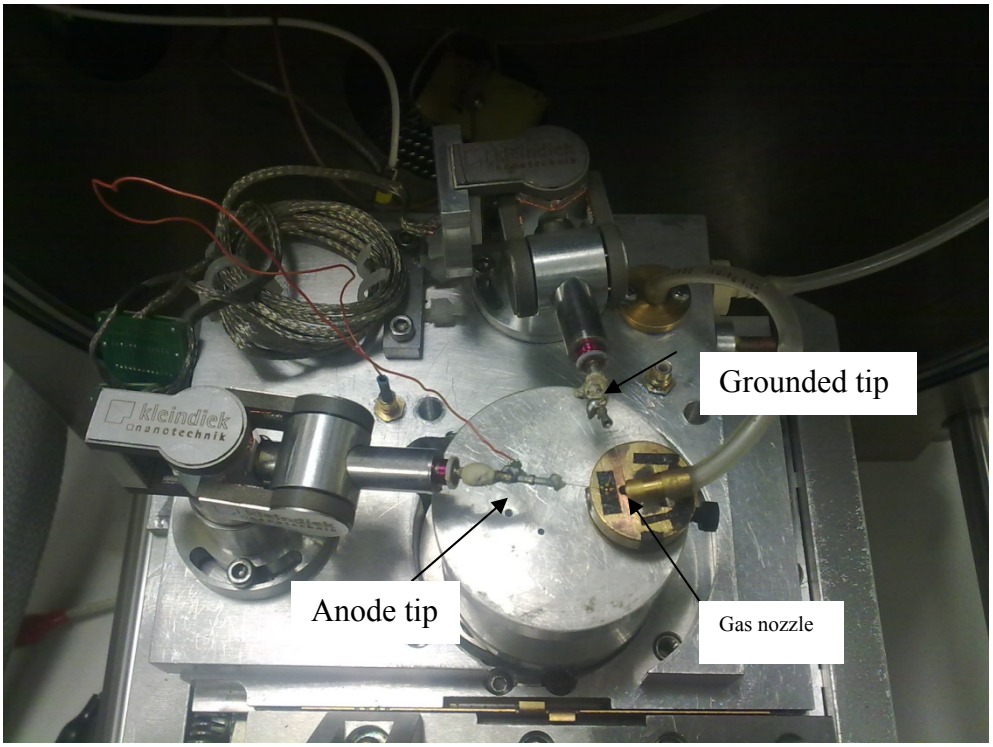

Figure 3.9 Top view of set-up used for growing nanowire on TEM sample (copper grid and silicon nitride membrane die).

3.3.2 Nanowire growth methodology

To initiate field emission induced nanowire growth, a sharp field emission protrusion on the flat substrate is required. One technique we adopted to create a sharp protrusion on the substrate is by arc discharge. To do this, the tungsten tip anode probe is approached to contact the ground substrate (either metal electrode or TEM substrate) directly. Typically, the SMU is set to source a current of 1 μA with a compliance voltage of 1000 V. A potential drop of 100V will be formed across the

100 MΩ buffer resistor. Tungsten carbonyl vapor is introduced into the chamber via the nozzle and adjusted by the leak valve until the chamber pressure is about 5×10^{-5} mbar. The anode tip is then slowly moved up till the contact between the substrate and anode probe is broken. Upon breaking the contact, a potential of 100V will immediately form between the substrate and the anode probe resulting in an arc discharge, forming a sharp stumpy tip at the substrate (cathode). The formation of the tip can be observed by the rapid reduction of the voltage at the SMU indicating a field emission source had formed at the electrode. The voltage from the SMU is immediately terminated and a short and sharp field emission tip has now been formed at the electrode.

Growth of the nanowire can then proceed in the same way as described in section 3.2. Figure 3.10 shows the SEM image of a tungsten nanowire grown on a silicon die initiated from the starting site by arc discharge. This technique often results in considerable crater-like damage at the starting site.

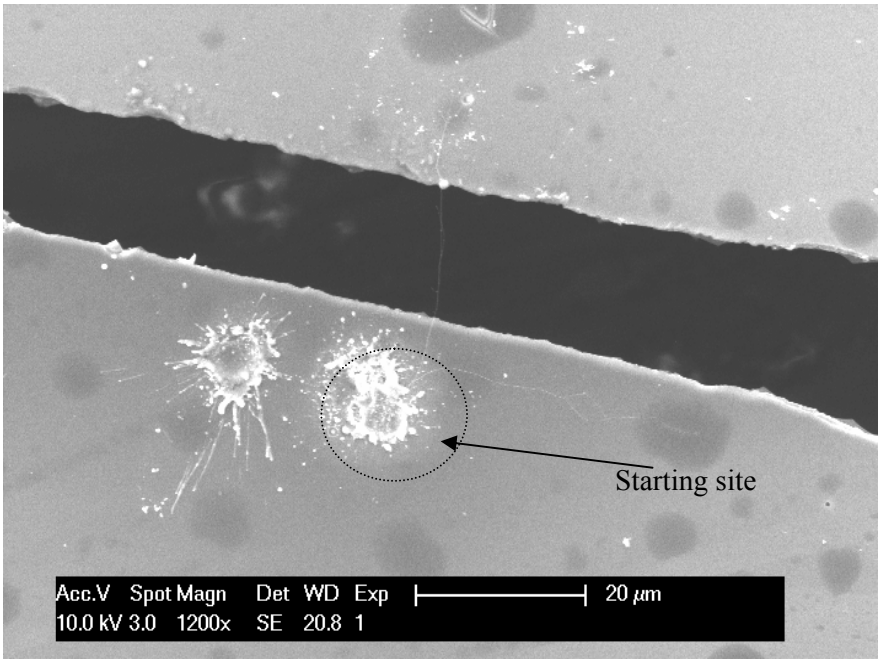

Figure 3.10 Nanowire initiated by arc discharge

The damage of the cathode surface is caused by hot (~6000°C) arc spots generated by the arc discharge. It is known that the random motion of arc spots influences the eroded crater size [Daalder 1979, 1983]. As the arc spot moves under the electric field between the cathode substrate and anode tip, it is expected that if the distance between the tip and surface is reduced, the crater size can be reduced due to confinement of arc spot movement. Hence by separating the tip from the substrate slowly (with the current nanomanipulators the smallest step size is ~5nm) the region of damage at the starting site can be effectively minimized as shown in Figure 3.11.

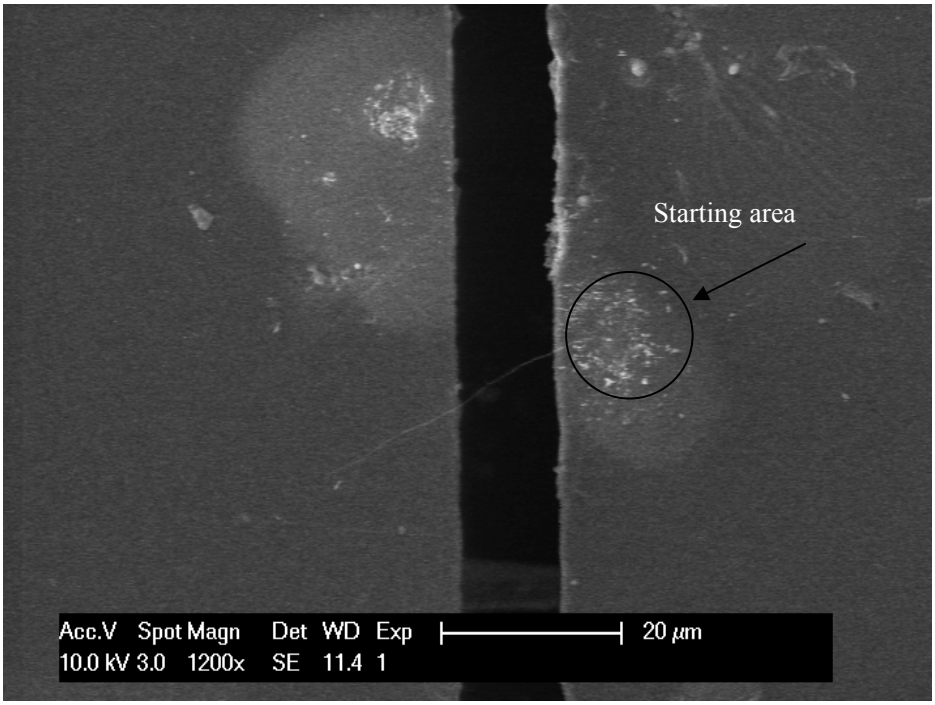

Figure 3.11 Nanowire grown with minimum surface damage

During growth, the free end of the nanowire is electrostatically attracted towards the anode tip. This allows the moving anode tip to direct the growth of the nanowire. The growth is terminated by turning off the applied current (voltage) and the nanowire falls down to the substrate under its own weight.

For electrical measurements, the free end of the nanowire needs to be contacted and it is desirable if it lands on an electrode. Likewise, for TEM imaging, the nanowire should straddle a slot or gap in a micromachined substrate. However, when the growth is terminated, it was found that nanowires tend to land on the oxide or silicon nitride membrane if present. It is suspected that charging of the oxide/nitride by the SEM electron beam might have attracted grown wires to these charged insulating regions. In addition, even if there is no exposed oxide/nitride surface nearby, the growing end of a nanowire tends to land in the direction opposite to that intended. This is likely to be caused by a whiplash phenomenon. During growth, the nanowire is under tension [Gomer, 1958] due to electrostatic attraction towards the anode. Upon termination of the electric field, the stress is released and the nanowire whiplashes to land on the side opposing the anode tip.

To minimize these effects and attach the nanowire to the desired ending site on the substrate, two issues must be addressed:

1) To reduce the whiplash effect, the growing end of the nanowire (cathode) must be very near to the anode tip, so that the applied voltage between the cathode and anode is low (< 40 V). This will localize and reduce the electric field at the nanowire tip.

2) The anode tip must be very close to the desired anchor site (< 1μm) before terminating the electric field. This has 2 effects – the electrostatic screening of stray fields by the conductive ending site, and allowing the nanowire to fall by its own weight quickly before it is attracted away by the stray fields.

The above requirements demand accurate positioning of the tip probe, which could be attained with our nanomanipulators and real-time imaging in the SEM. Figure 3.12

and Figure 3.13 show examples of nanowires growing and bridging the oxide surface and nitride membrane gap between the metal electrodes, respectively.

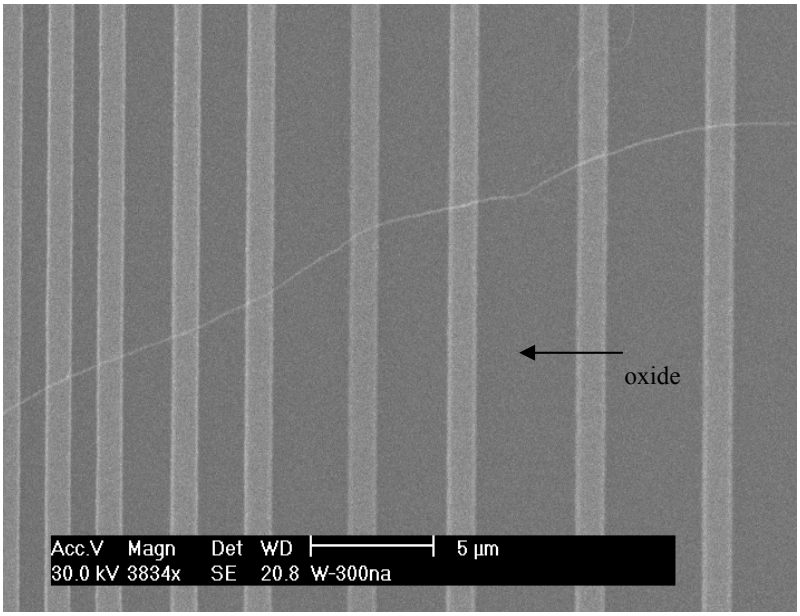

Figure 3.12 Nanowire bridge over the oxide gap

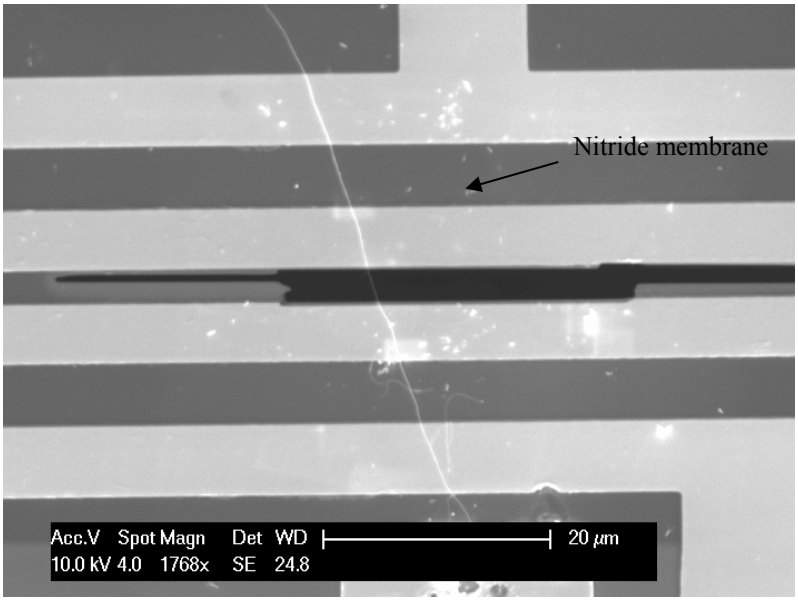

Figure 3.13 Nanowire bridge over the nitride membrane

3.4 TEM characterization of the nanowire

TEM characterization was carried out to determine the microstructure and phase of tungsten nanowires grown at field emission currents ranging from 100 to 1000nA. Figure 3.14 shows a nanowire grown on a micromachined carbon film suspended on a copper mesh TEM grid.

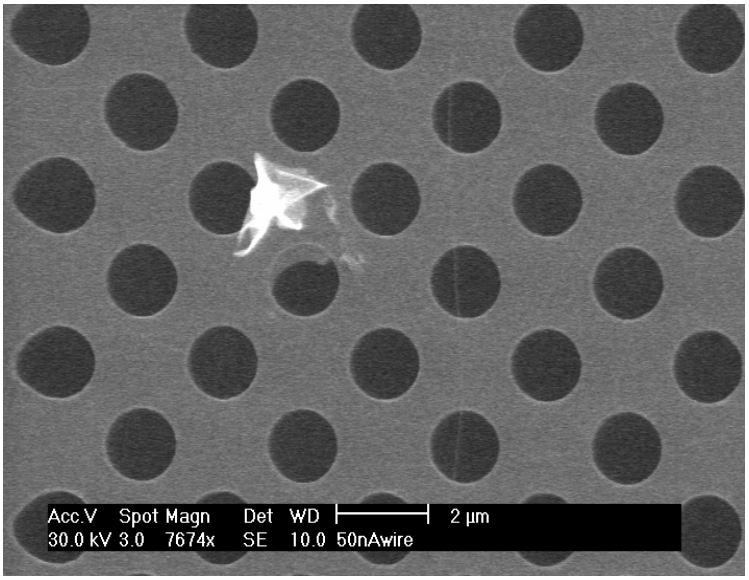

Figure 3.14 A single nanowire grown on a TEM grid (with Quantifoil® holey-carbon membrane).

3.4.1 Electron Diffraction Pattern

To identify the crystal structure and lattice constant of the tungsten nanowire, selected area electron diffraction (SAED) was carried out. Before the experiment, the camera length (L) was firstly calibrated from the selected area diffraction pattern (SADP) for a Si (110) film with a well known d-spacing value (d_{Si} = 5.4309Å). By assuming the effective camera length to be unchanged during the SAED of the tungsten nanowire:

$$R_{si} d_{si} = R_w d_w = L\lambda \qquad (3.2)$$

where R_{si} and R_w are the measured separations between the direct beam spot and diffracted spot/ring from the SADPs of the silicon film and tungsten nanowire, respectively, and λ is the electron wavelength, from which the d-space of the tungsten (d_w) can be estimated. From d_w, the indexing of SADPs was performed based on JCPDS powder diffraction file (PDF) (No. 04-0806 tungsten(BCC)). Figure 3.15 shows an indexed SADP, which is typical for tungsten nanowires grown at all growth currents (from 20 to 1000nA). The first nine diffraction rings can be indexed with the most probable Miller planes (*hkl*) of BCC tungsten.

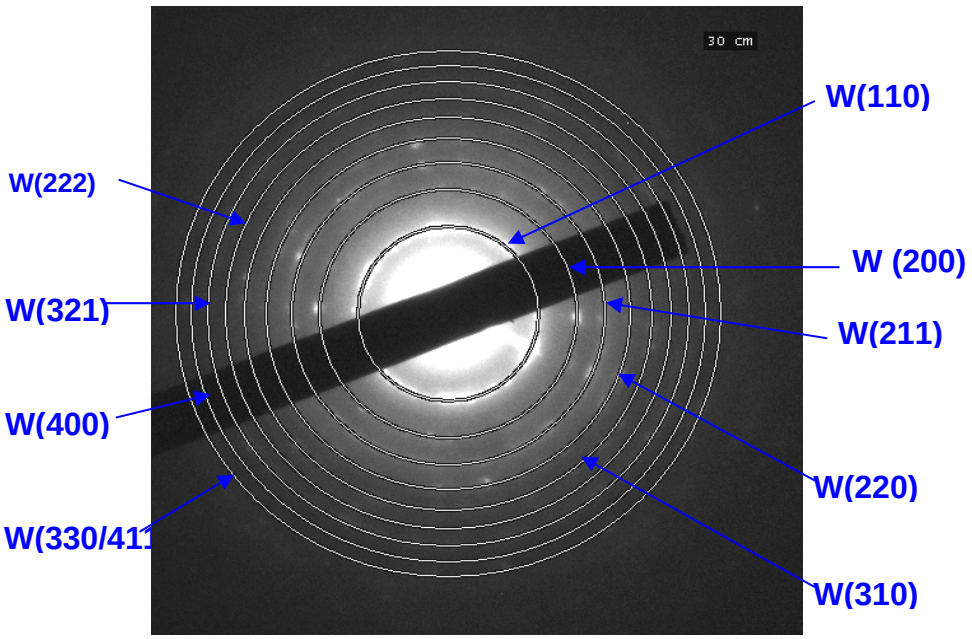

Figure 3.15 A typical selective-area diffraction pattern indexed with most probably (*hkl*) planes.

Moreover, equilibrium bulk-like bcc crystal structure was detected without lattice expansion. This result supports the fact that sources of thermal energy would have been available for enhanced atomic diffusion, thereby enabling crystallization and grain growth to occur. The possible sources of thermal energy are (i) enhanced phonon scattering with the surfaces and grain boundaries of wires with nanometer dimensions and (ii) energetic impact of returning W^+ ions onto nanowire growth front

that is rapidly evolving during the growth process [Onn 2006]. While the former is a typical thermal energy source available for nanostructured materials, the latter is unique to the FEIG process and is believed to be the major energy contributor leading to high crystallinity of the nanowires. The absence of elongated lattice parameters despite the high tensile stress growth environment is probably due to the numerous crystalline defects or dislocations that might have fully compensated for the localized lattice elongations.

3.4.2 TEM imaging

Bright-field (BF) TEM imaging was used to study the morphology of the polycrystalline BCC tungsten nanowires.

Figure 3.16(a) shows a typical BF image of the tungsten nanowire grown at 1000nA. The result is believed to be representative for specimens grown at currents from 100nA to 1000nA. The image shows that the cylindrical nanowire has the non-uniform diameter and a rough surface. Based on numerous acquired BF images, diameter measurements were obtained after averaging readings at various segments of one nanowire (normally 10 to 20 segments). For example, the mean diameter of the nanowire grown at 1000nA is about 45.6nm with a deviation of about ±8.6nm. (Figure 3.16(a)).

In addition to an uneven diameter, a thin layer of carbonaceous was observed on the nanowire surface as shown in Figure 3.16(b). It is clear that there exists two phases with very different atomic weights and degree of crystallinity. The structure of the cylindrical core is identified to be mainly BCC tungsten from electron diffraction, while the less-dense phase outer shell is believed to be carbonaceous.

To examine the carbonaceous layer, electron-energy-loss spectroscopy (EELS) mapping was carried out. Figure 3.16(c) shows the C-loss signal mainly detected from the surface which matches the overcoat layer enveloping the nanowire in Figure 3.16(b). There are two possible origins for carbonaceous overcoat: (i) according to the FEIG growth mechanism in Section 3.2, carbon atoms are dissociated from the CO molecules (Equation 3.1) and some land on the nanowire surface, resulting in an overcoat; (ii) carbonaceous contamination deposited by SEM imaging of the nanowire [Postek 1996]. In fact, this contamination effect is severe if the nanowire is viewed under high magnification for any significant period of time. In general, the thickness of the carbonaceous overcoat layer is typically in the range of 1-5nm.

The uniform contrast of the carbonaceous overcoat layer in Figure 3.16(b) suggests that it is amorphous. This can be confirmed by the high resolution phase-contrast image as shown in Figure 3.16(d), which shows the interface between the overcoat and the tungsten core (W(110) plane) with a lattice spacing of 0.21nm.

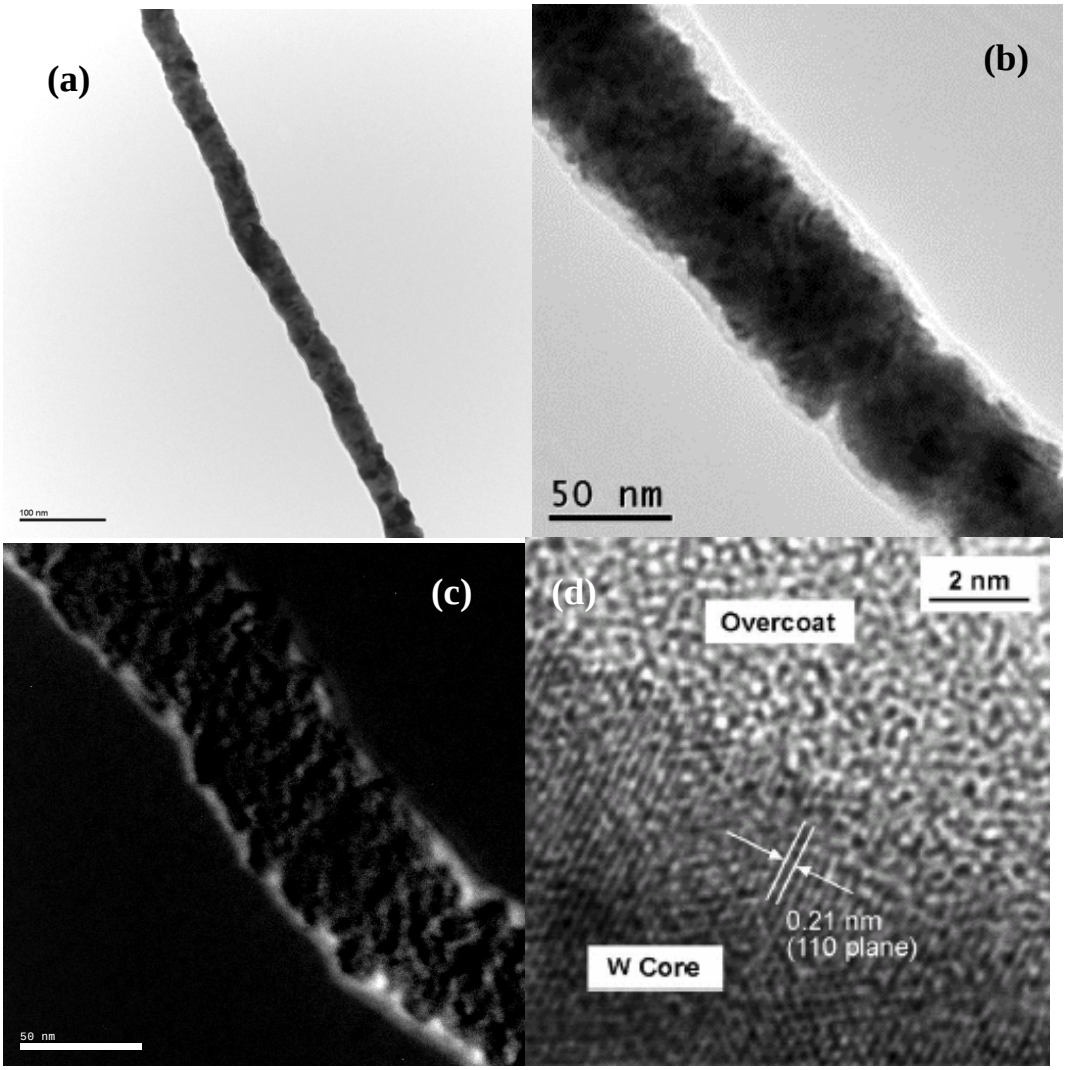

Figure 3.16 (a) A typical BF image of nanowire grown at 1000nA, (b) high resolution BF image of nanowire grown at 1000nA and its (c) carbon energy loss image. (d) High resolution image shows a W-C interface.

Figures 3.17 (a) and (b) show high resolution images of the nanowires of 33±8nm and 25±5 nm diameters, respectively. The results reaffirms the nature of tungsten nanowires as determined from SADP (Figure 3.15), that the tungsten nanowires are indeed polycrystalline with nanosized grains randomly oriented relative to each other. The circled areas in the figures show Moiré fringes [Hashimoto 1957] with alternating intensity due to the spatial overlap of two or more grains causing periodic lattice fringes with spacing ~ 0.2nm-0.3nm oriented in various directions, and Moiré fringes within the tungsten core.

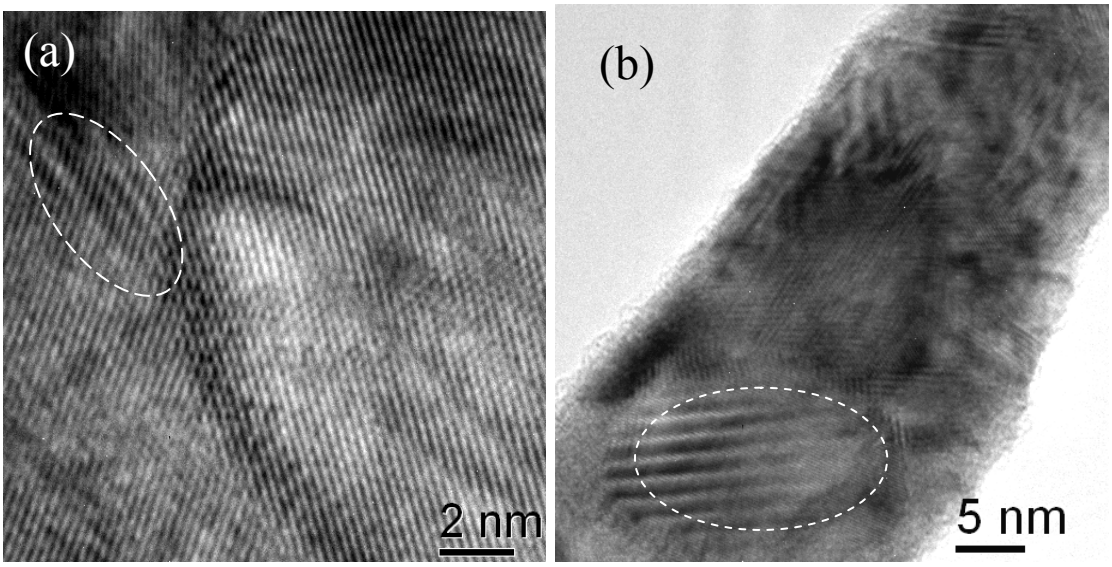

Figure 3.17 High-resolution TEM micrographs of nanowire of (a) 33nm and (b) 25 nm diameter

The crystal grains are studied via dark-field (DF) imaging. Figure 3.18 shows a typical DF image formed using part of the W(110) diffraction ring (see Figure 3.15). It is observed that the size of diffractive grains ranges from 10 to 30 nm in diameter.

The DF image also shows that the grains are irregularly shaped with some of them being columnar. Such columnar grains probably resulted from grain growth process due to the heat generated by ion bombardment at growing end of the nanowire, and Joule-heating of the nanowire. The latter contribution is believed to be relatively insignificant compared to ion bombardment. This was shown experimentally where Joule-heating at current density of 10^5 Acm^{-2} (the maximum current density during growth) is insufficient to provide the thermal energy needed for grain growth in the nanowire. In chapter 4, we will demonstrate the formation of columnar grains by annealing using Joule heating, but only at much higher current densities.

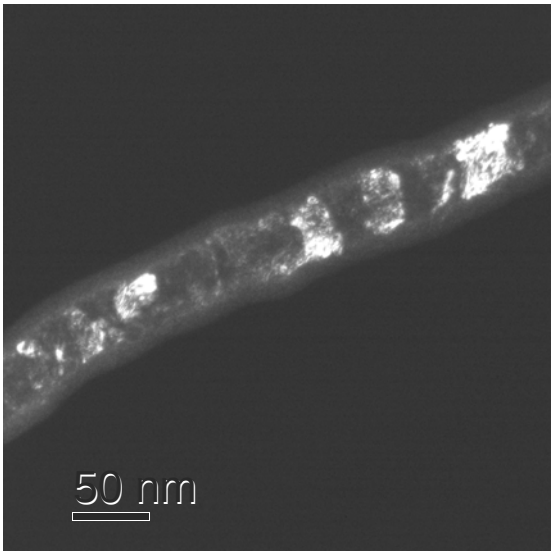

Figure 3.18 A typical dark field image of a nanowire (growth current of 500nA)

The size of diffractive grains was measured from the DF images for nanowires of different diameters as determined from BF images. A possible source of error during grain-size measurement through DF images may come from the uncertainty in overlap between the grains perpendicular to the incident beam (as shown in Figure 3.17).

The mean grain size and grain-size standard deviation of one nanowire is calculated from measurements of about 10-20 diffractive grains. Sizes of irregularly shaped grains are measured by averaging the lengths measured over different lines drawn across the individual grain. Results of are presented in Figure 3.19.

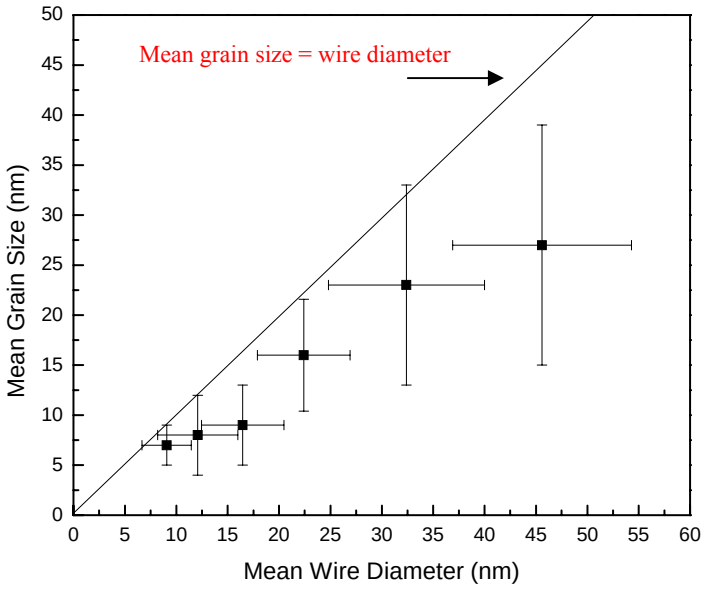

Figure 3.19 Mean grain size Vs. nanowire diameter

It can be seen that the average grain size increases with nanowire diameter but appears to saturate around 20-26nm at wire diameters in the range of 30-50nm. The range of grain sizes observed also increases with wire diameter. For small diameter nanowires, the mean grain size is much closer to nanowire diameter (refer to the line in Figure 3.19). Together with the small standard deviation, it suggests there is almost a single grain across the diameter along the nanowire. This observation is further supported by a high resolution TEM of a 12 nm nanowire (Figure 3.20). Individual grains (refers to the circles in Figure 3.20) can be discerned through their lattice fringes. This is unlike larger-diameter nanowires, in which several grains overlap across the diameter (compare Figure 3.17).

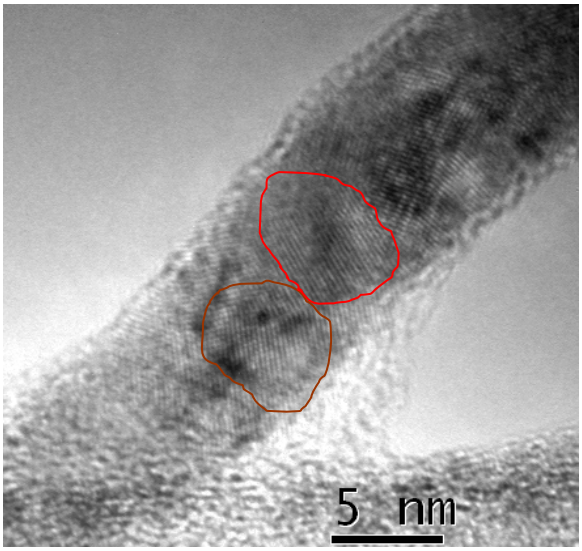

Figure 3.20 High resolution micrograph of nanowire of 12 nm diameter.

3.5 Electrical characterization of the FEIG nanowire

It is accepted [Xia 2001] that nanowires provide a good system to investigate the dependence of electrical on size reduction. In this section, the electrical properties of FEIG tungsten nanowires will be presented. Focused ion beam induced deposition of platinum is used to make contacts to the nanowire. Using 4-point I-V measurements, the size effect of tungsten nanowire from 10nm to 50nm is studied. The experimental results are used to study contributions from both surface and grain boundary scattering to the nanowire resistivity.

3.5.1 Two- and Four- terminal I-V measurements

Two-terminal I-V measurements were carried out using the set up shown in Figure 3.6 after nanowire growing on the electrode patterned sample. Figure 3.21(a) shows a typical I-V curve of a nanowire with an average diameter of 18nm and length of 10μm. The characteristics are non-linear due to the non-ohmic contacts between the nanowire and electrodes, and the two-terminal method includes contributions from the contact resistance. The presence of a non-ohmic contact between the W nanowire

and electrode can be understood on the basis of tunneling transport through the small-area contacts that nanowires make and is widely encountered in such two-terminal I-V measurement [Legrand 2002, Liu 2003, Franceschi 2003]. In addition, the carbonaceous overcoat on the nanowire could also be a source of poor contact resistance. To solve the contact problem, focused ion beam (FIB) Pt deposition was used [Ebbesen 1996, Wei 1999, Lin 2003]. The deposition process is illustrated in Figure 3.22. Before Pt deposition, the nanowire was first irradiated with the Ga^+ ion beam for a few second in order to sputter-off the overcoat layer on the nanowire. (Figure 3.22(a)) The Pt precursor gas was then introduced into the FIB chamber in the path of the Ga^+ ion beam (Figure 3.22(b)) thus depositing Pt-containing material onto the contacts and provided a conducting path between the W nanowire and electrode (Figure 3.22(c)).

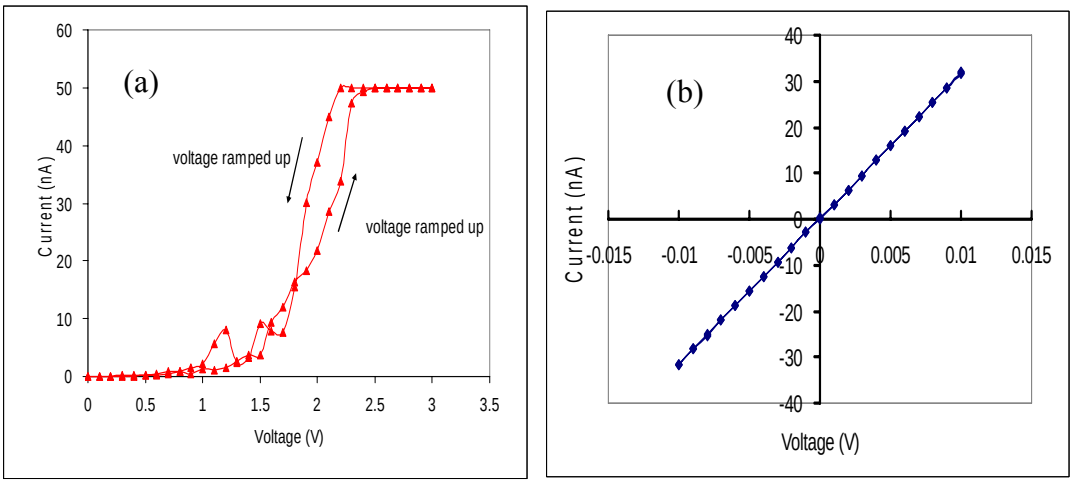

Figure 3.21 IV characteristics of 18nm-diameter nanowire (a) without FIB contact treatment (b) with FIB contact treatment.

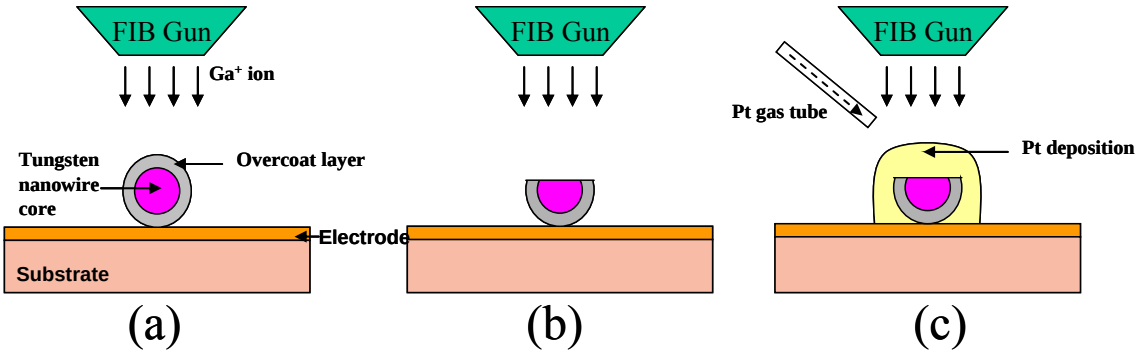

Figure 3.22 Forming nanowires contact by FIB Pt deposition.

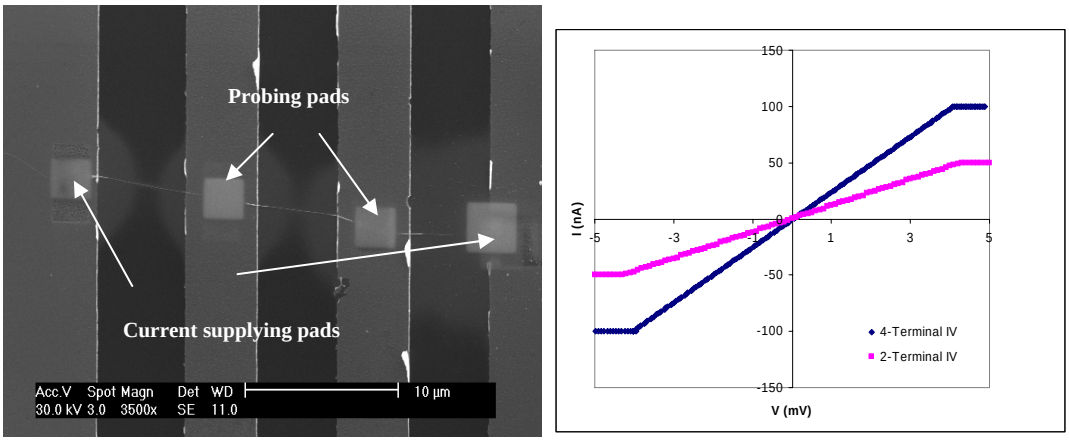

Figure 3.23 (a) SEM image of 4-point contacted nanowire with FIB treatment (b) IV characteristic of nanowire using 2- and 4-point measurements.

Figure 3.21 (b) shows the I-V curve after Pt deposition. It shows that an Ohmic-contacting has been achieved and resistance was thereby reduced to about 230 kΩ. Although FIB deposition provides an efficient way to form ohmic contacts, a 2-point measurement includes both resistance of the nanowire and those of the two FIB contacts. Hence 4-point measurements were carried out on specimens where the nanowire bridged across four electrodes with four Pt-deposited contacts. (Figure 3.23 (a))

Figure 3.23(b) compares two- and four-point I-V measurements for a nanowire of 10 nm in diameter and 7.6µm in length. The resistance of the nanowire measured from the four-terminal method is about 40 kΩ, which is about half the resistance of 86 kΩ measured by the two-terminal method between the two inner contacts. From the

four-point measurement, the resistivity of the tungsten nanowire is 160 μΩ·cm, which is about 18 times that of bulk tungsten (10.2 μΩ.cm at room temperature).

One factor that may cause the comparatively large resistivity in tungsten nanowire is the size effect, arising from enhanced electron scattering in fine structures.

3.5.2 Influence of nanowire diameter

To understand the mechanisms contributing to the resistivity of nanowires, 4-point measurements were carried out on nanowires of different diameters. Figure 3.24 shows the diameter-dependent resistivity measured at 293K. It can be seen that the values (square dots) decrease substantially from 226 μΩ·cm to 88 μΩ·cm as the mean diameter increases from 10 nm to 50 nm. Similar trends can be observed in other materials such as Au [Alexander 2002], Cu [Wu 2004], Bi [Chiu 2004] among others.

The increase in resistivity can be explained by an ordinary size effect [Sambles, 1983, Barati 2001, Durkan 2000]. Given the nanowire cross-section of nanowire is less than the electron mean free path (in our tungsten nanowire of circular cross-section, the mean free path of tungsten at room temperature is about 30nm [Steinhögl 2005a]), shrinking the diameter results in an increase of electron scattering at surface boundary (external interface) and grain boundary (internal interface) of the nanowire. The influence of surface-boundary scattering on the size effect has been proposed by Fuchs and Sondheimer (FS model) [Fuchs 1938, Sondheimer1952] while grain-boundary scattering mechanism can be explained by the Mayadas and Shatzkes (MS model) [Mayadas 1970]. A combined model was proposed by Durkan *et al.* who estimated the overall resistivity by adding both scattering components together [Durkan 2000]. The corresponding simulation works were extended to wires of

rectangular cross-section [Steinhögl 2002, 2003 2005(b), Steinhögl 2005] and circular cross-section [Chiu 2004, Mollars 2004].

To simulate the size effect of tungsten nanowire of circular cross-section, the FS model can be simply solved using Dingle's approach [Dingle 1950]. The resistivity due to the surface elastic scattering can be expressed as:

$$\frac{\rho_0}{\rho} = 1 - \frac{3}{4}k + \frac{3}{8}k^3 \qquad \text{if } k >> 1 \tag{3.3}$$

$$\frac{\rho_0}{\rho} = k - \frac{3}{8}k^2\left(\ln\frac{1}{k} + 1.059\right) - \frac{2k^3}{15} \qquad \text{if } k << 1 \tag{3.4}$$

$$k = \frac{d}{\lambda} \tag{3.5}$$

where ρ is the resistivity of the bulk materials, λ is the electron mean free path, and d is the average diameter of wire.

The MS model applied for wires of rectangular and circular cross-section are the same, so the resistivity of tungsten nanowire due to the grain boundary scattering can be expressed as [Mayadas 1970]:

$$\frac{\rho_0}{\rho} = 3\left[\frac{1}{3} - \frac{\alpha}{2} + \alpha^2 - \alpha^3 \ln(1+\alpha)\right] \tag{3.6}$$

$$\alpha = \frac{\lambda}{D}\frac{R}{1-R} \tag{3.7}$$

where D is average distance between the grain boundaries, which is equals to the mean grain size. R is the electron reflection coefficient representing the probability of an electron being reflected at a grain boundary. The resistivity increase in the MS model is highly dependent on the parameter R and mean grain diameter. In the simulation, the mean grain sizes of our tungsten nanowires were taken from the measurement values ranging from 7-26 nm (Figure 3.19).

Taking the mean free path in tungsten as 30nm and the bulk tungsten resistivity as 10.2 μΩ.cm [Steinhögl 2005b], the resistivities predicted using the FS, the MS and the combined MS+FS models are plotted alongside the experimental measurements. It can be seen that the prediction from FS model underestimates the experimental data by about 70%, implying that the increase of resistivity cannot be attributed to surface scattering alone. Therefore the influence of grain boundary scattering was considered by examining the results from the MS model and the combined (FS+MS) model. Clearly from Figure 3.24, the prediction from the MS model is closer to experimental measurements while the prediction from the combined FS+MS model agrees well with our experimental results if R is taken as 0.8. These results suggest that transport in the tungsten nanowire is mainly dominated by boundary scattering due to nanosized grains giving rise to a huge amount of grain boundaries in the nanowire. For nanowires smaller than the 15nm, the prediction line from MS model becomes saturated while the line from FS model continuously increasing. This is because initially the containing grain boundary area reduces with the nanowire diameter decreasing from 50nm to about 15 nm due to the reduction of mean grain size (see Figure 3.19), but once the nanowire diameter is smaller than 15 nm, the containing grains become straddling over the diameter (see Figure 3.20) so that reduction of grain boundary area is suppressed with further decreasing of diameter. As a results, the scattering contribution from grain boundary to the resistivity of smaller nanowire ($d<15$nm) saturates, while the scattering contribution from nanowire surface continually increasing.

The R value of 0.8 adopted in the present simulation for best-fit to the experimental data is larger than the value of 0.25 reported by Steinhögl in the tungsten nano-interconnects deposited by CVD [Steinhögl 2005]. This is reasonable since the

mean grain sizes in our nanowires (range from 7-26 nm) are much smaller than theirs (range from 30-60nm), so that the scattering probability by the grain boundary in our nanowire is higher. Therefore, for better electrical conductance in polycrystalline FEIG tungsten nanowire, we attempted to transform the original as-grown nanowire into a structure comprising larger grains. Based on this consideration, in the next chapter, we will anneal FEIG tungsten nanowire and study the evolution of the grains in detail.

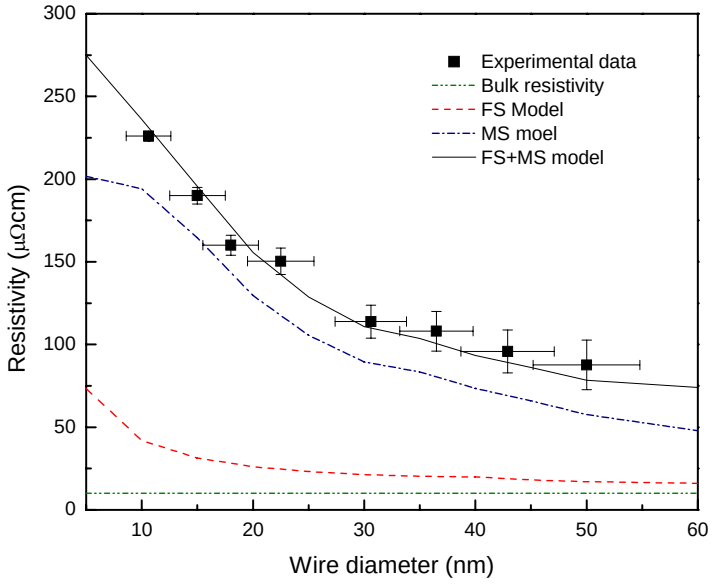

Figure 3.24 Diameter dependence of the resistivity of tungsten nanowires measured by four-point method at room temperature (293K).

3.6 Summary

In this chapter, single tungsten nanowire was grown on a flat substrate by using FEIG method. Through TEM characterizations, it was found that the as-grown nanowires are mainly polycrystalline tungsten structure comprising irregularly shaped grains. The mean grain size was found to increase with nanowire diameter. Electrical I-V measurements of nanowires were successfully carried out. The results were

finally analyzed in order to understand the various scattering contributions to the resistivity of nanowires.

References

Barati M. and Sadeghi E., (2001),*Nanotechnology* **12**, 277

Bergmann G., (1984), *Phys. Rep.* **107**, 1.

Bietsch A. and Michel B., (2002), *Appl. Phys. Letts.* **80**(18) 3346.

Ebbesen T. W., Lezec H. J., Hiura H., Bennett J. W., Ghaemi H. F., and Thio T., (1996), *Nature* **382**, 54.

Cantone B. F., Grasso N., and Pignataro S., (1966), *Journal of Chemical Physics* **44**(8), 3115.

Daalder J. E., (1979), *J. Phys. D : Appl. Phys.* **12**, 1769.

Daalder J. E., (1983), *J. Phys. D : Appl. Phys.* **16**, 17.

Dingle R. B., (1950), *Proc. R. Soc. A* 201, 545

Durkan C. and Welland M. E., (2000), *Phys. Rev. B* **61**, 14215.

Franceschi S. D., Dam J. A. V., Bakkers E. P. A. M., Feiner L. F., Gurevich L., and Kouwenhoven L. P., (2003), *Appl. Phys. Lett.* **83**, 344.

Fuchs K., (1938), *Proc. Cambridge Philos. Soc.* **34**, 100.

Hashimoto H., R. (1957), Uyeda, *Acta Crystallogr.* **10**, 143.

Hu J., Odom T. W., and Lieber C. M., (1999), *Accounts of Chemical Research* **32**(5), 435.

Josell D., Burkhard C., Li Y., Cheng Y. W., Keller R. R., Witt C. A., Kelley D. R., Bonevich J. E., Baker B. C., and Moffat T. P., (2004), *J. Appl. Phys.*, **96**, 759.

Kent A. D., Shaw T. M., Molnar S. V. *et al.,* (1993) , *Science* **262**, 1249.

Legrand B., Deresmes D., and Stievenard D., (2002), *J. Vac. Sci. Technol. B* **20**, 862.

Lin J. F., Birda J. P., Rotkina L., and Bennett P. A., (2003),*Appl. Phys. Letts.* **82**, 802

Linden H. B., Hilt E., and Beckey H. D., (1978), *J. Phys E* **11**, 1033.

Liu C. H., Yiu W. C., Au F. C. K., Ding J. X., Lee C. S., and Lee S. T., (2003), *Appl. Phys. Lett.* **83**, 3168.

Mayadas A. F. and Shatzkes M., (1970), *Phys. Rev. B* **1**, 1382.

McDaniel E. W., (1964), *"Collision phenomena in ionized gases"* ed: John Wiley and Sons, New York.

Molares M. E. T., Chtanko1 N, *et al.*, (2004), *Nanotechnology* **15**, S201

Mølhave K., Gudnason S. B., Pedersen A. T., C. H. Clausen, Horsewell A., and Bøggild P., (2006), *Nano Letters.* **6**(8), 1663.

Neumann G. M., Rogers D. E., Derrick P. J. *et al*. (1980), *J. Phys. D* **13**, 485.

Okuyama F., Shibata T., and Yasuda N., (1979), *Appl. Phys. Lett*. **35**(1), 6.

Okuyama F., (1980a), *Appl. Phys. Lett.* **36**(1), 46.

Okuyama F., (1980b), *J. Crystal Growth* **49**, 531.

Okuyama F., (1982), *J. Appl. Phys.* **53**(9), 6226.

Okuyama F., and Fujimoto Y., (1984) *J. Appl. Phys.* **56**(2), 566.

Okuyama F., Aoyama S., and Fujimoto Y., (1991), *J. Crystal Growth* **114**, 107.

Oon C. H., Thong J. T. L., Lei Y. *et al*, (2002a) *Appl. Phys. Lett*. **81**, 3037

Oon C. H., Thong J. T. L., Yeadon M. *et al*. (2002b), *Appl. Phys. Lett*. **81**, 4823

Oon C. H., Khong S. H., Boothroyd C. B., Thong J. T. L.. (2006), *J. Appl. Phys.* **99**(6), 064309.

Postek M. T., (1996), *SCANNING* **18**, 269

Sambles J.R., (1983), *Thin Solid Films* **106**, 321

Sondheimer E. H., (1952), *Adv. Phys.* **1**, 1.

Steinhögl W, Schindler G., Steinlesberger G., and Engelhardt M, (2002), *Phys. Rev. B* **66**, 075414.

Steinhögl W., Schindler G., Steinlesberger G., Traving M., and Engelhardt M., *Proceeding on Inter. Conf. on Simul. Semi. Proc and Dev.* (2003), 27.

Steinhögl W., Steinlesberger G., *et al*, (2005a), *Microelectronic Engineering* **82,** 266.

Steinhögl W., Schindler G., Steinlesberger G., Traving M., and Engelhardt M., (2005b), *J. Appl. Phys.* **97**, 023706.

Wei B., Spolenak R., Redlich P. K., Ru¨hle M., and Arzt E., (1999), *Appl. Phys. Lett.* **74**, 3149.

Wu W., Brongersma S. H., Hove M. V., Maex K., (2004), *Appl. Phys. Let.* **84**, 2838.

Xia Y., Yang P., Sun Y. *et al*. (2003), *Advanced Materials* **15**(5), 353.

Xu S. Y., Xu J., and Tian M. L. (2006), *Nanotechnology* **17**, 1407.

Chapter 4 Structure Transformation in Polycrystalline Tungsten Nanowire

Tungsten nanowires grown by the FEIG method are highly disordered, containing a high density of grains and grain boundaries that possess large excess free energy. This provides a significant driving force for crystallization and grain growth of such nanowires at elevated temperature [Fecht 1990, Klement 1995]. This chapter describes the evolution of the microstructure as a result of high-temperature annealing.

4.1 Experimental Set-up

FEIG tungsten nanowires were grown directly on 3×3 mm^2 dies with through-substrate slots which allow un-obscured TEM imaging of the straddling nanowires as shown in Figure 4.1. To anneal the nanowire, three different processes were designed and used in the experiments:

(1) Annealing in vacuum chamber (Method 1)

The nanowires were annealed in a vacuum chamber at a base pressure of 2×10^{-6} mbar in order to minimize oxidation of the tungsten nanowire during the annealing process. (The heating set-up will be described in Figure 5.1 in Chapter 5) After cooling to room temperature in the vacuum, the sample was then examined in the TEM.

(2) *In situ* annealing in the TEM (Method 2)

This method involves *in situ* annealing of the nanowire which is carried out using a silicon die as the heating element in a specially-designed TEM holder for a JEOL JEM 2000V microscope. Figure 4.2 illustrates the schematic of the heating arrangement. One end of the nanowire was connected to the grounded silicon substrate while another end of the nanowire lay on a 100nm thick SiO_2 layer. By

passing a current through the silicon die substrate, the nanowire can thus be indirectly heated up to 1000°C. Before annealing, the relationship between the temperature of TEM die and the heating current was calibrated through a viewport in the TEM using a pyrometer. Compared to Method 1, the greatest advantage of this approach is the ability to observe structural transformations in real time. However, above ~600°C, real-time imaging is problematic due to thermally-induced sample drift, which limits the resolution attainable.

(3) *In situ* annealing in the TEM using direct Joule heating (Method 3)

Although Method 2 allows real-time imaging, due to thermal expansion of the supporting heater substrate, the problem associated with the sample drift diminishes the potential of TEM studies especially at high resolution. Hence a method of direct Joule-heating of the nanowire was developed. Figure 4.3 shows the Joule-heating arrangement. Since only the nanowire is heated to high temperature, thermal expansion of the stage is significantly reduced. This method offers considerably better stability for TEM imaging. Temperatures up to 1000°C can be achieved in the middle of the nanowire, while the small power dissipation (typically 10^{-6} W) means that the substrate remained essentially at room temperature. The TEM die was placed in either one of two TEM holders (manufactured by Nanofactory for the Philips CM300 Ultra-Twin™, and JEOL JEM 2010F, Figure 4.4) with electrical feedthroughs connected to a source-measurement unit (SMU).

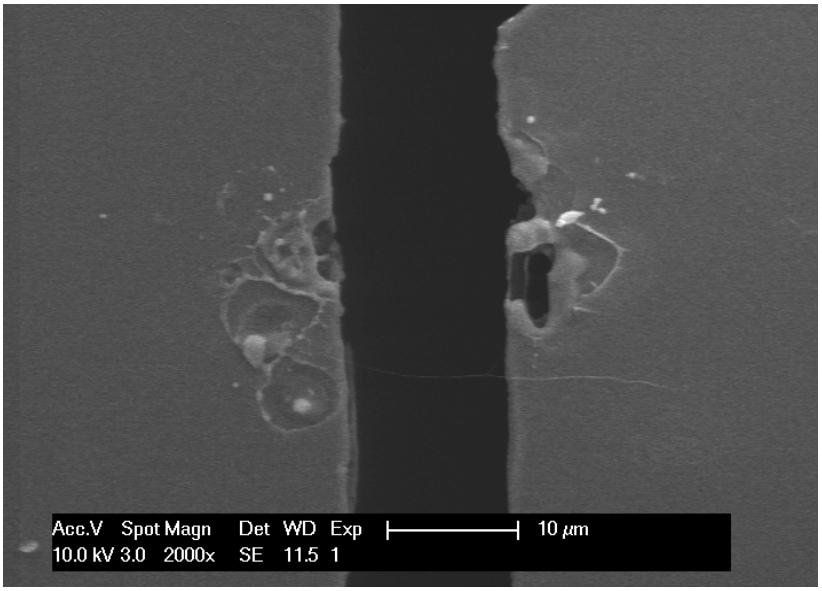

Figure 4.1 SEM image of a nanowire grown on a Si TEM die (3x3 mm^2).

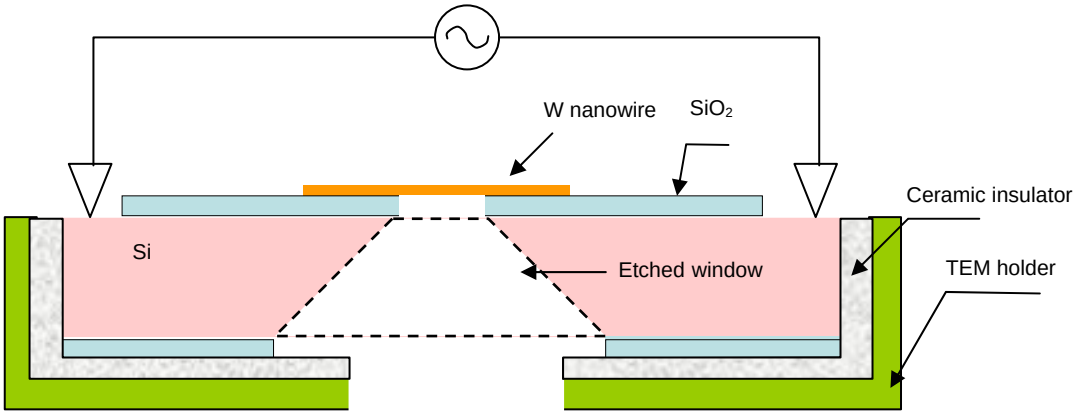

Figure 4.2 Schematic showing nanowire annealed on a heating element.

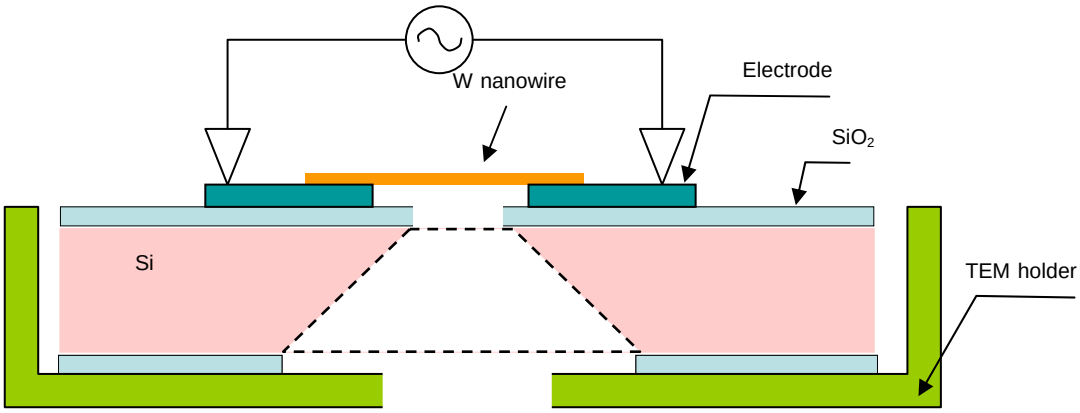

Figure 4.3 Schematic showing nanowire annealed on a TEM die through Joule-heating.

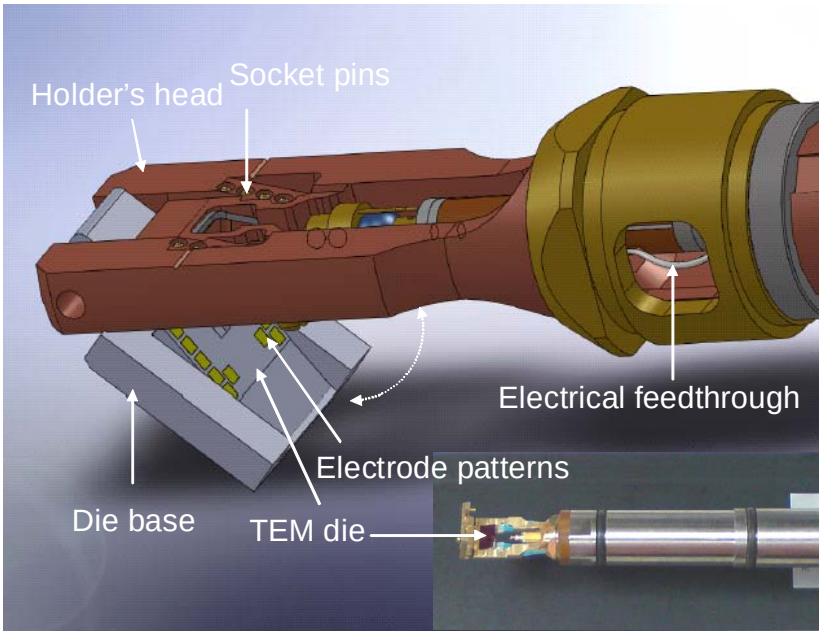

Figure 4.4 A schematic of custom-made TEM holder (inset is photo of the holder): During TEM imaging, the TEM die is mounted on the "Die base". Once the "Die base" clamped on to the holder's head, the "socket pins" (x 8 pins) will contact to the electrode patterns on the TEM dia. The socket pins are connected to a source measurement unit (SMU) via the electrical feedthroughs.

4.1.1 Temperature distribution along Joule-heated free-standing nanowire

With Methods 1 & 2, the temperature of the nanowire can be directly measured. However with Method 3, the temperature profile along the Joule-heated free-standing nanowire across a hollow slot (~ 10μm) has to be determined indirectly.

It is known that the steady state heat flow in and out of an element along the nanowire can be expressed as a balance between the heat generated in the element by electric current and the heat lost from the element. The possible heat losses in nanowire include radiation, convective loss, and conduction along the nanowire [Davies 1964].

The heat flow by conduction along the nanowire (along the axial direction, x) of is $-\kappa S dT/dx$ and so the heat loss per unit length by conduction is:

$$Q_c = \frac{d}{dx}[-\kappa S \frac{dT}{dx}], \qquad (4.1)$$

where S is the cross-section, T is the temperature, and κ is the thermal conductivity of the nanowire.

The heat generated by the current per unit length can be written as:

$$Q_e = I^2 \rho / S \qquad (4.2)$$

where ρ is electrical resistivity, and I is the current. Given the average diameter of 40 nm for the present nanowire, a typical current of about 22μA, and ρ of about 10^{-6} Ωm at room temperature, then Q_e is ~0.4 W/m.

The radiation loss per unit length can be estimated as:

$$Q_r \sim \sigma \varepsilon \pi d (T^4 - T_S^4) \qquad (4.3)$$

where σ is the Stefan-Boltzmann constant (5.6×10^{-8} $W \cdot m^{-2} \cdot K^{-4}$), ε is the emissivity of the wire surface, d is the diameter of the nanowire, and T_s is the temperature of the surroundings. For a nanowire of 40 nm in diameter, Q_r is in order 7×10^{-3} W/m assuming a worst-case scenario where the wire is at a uniform temperature of 1000K and its emissivity is unity. This is much smaller than Q_e, and thus radiative loss from the nanowire can be ignored. Moreover, since heating is carried out in a typical vacuum of 10^{-6} mbar, convective losses are negligible.

Therefore, for a Joule-heated tungsten nanowire system, the heat balance simplifies to:

$$Q_e \cong Q_c . \qquad (4.5)$$

Substituting (4.1) and (4.2) into (4.5) yields:

$$\frac{d}{dx}[-\kappa S \frac{dT}{dx}] = I^2 \rho S \qquad (4.6)$$

After integration, it becomes:

$$-\kappa \frac{dT}{dx} = \frac{\rho x I^2}{S^2} \qquad (4.7)$$

Based on Equation (4.7), a simulation method has been developed to calculate the temperature profile along the free-standing FEIG nanowire. The simulation detail can be found in Appendix B.

4.2 Design of Experiment

Firstly a preliminary *in situ* TEM study (method 2) was carried out for nanowire annealed at 850°C under vacuum environment (vacuum pressure ~ 2×10^{-6} mbar). (Table 4.1)

TEM studies of nanowires with different diameters were then carried out after annealing in a vacuum chamber (Method 1) covering a range of temperatures from 600°C to 900°C (Table 4.2).

To observe structural changes during the annealing process, *in situ* TEM studies were carried out through direct Joule heating (Method 3), as summarized in Table 4.3. The maximum temperature at the middle of each nanowire was simulated according to the corresponding stress current.

Finally, a comparison *in situ* TEM studies (method 3) was carried out between the tungsten nanowire and W-C core-shell nanowire in which a tungsten nanowire was coated with a layer of carbonaceous material (Table 4.4).

Table 4.1 Nanowire used for *in situ* TEM observation of annealing process (Method 2).

	Nanowire	Diameter	Annealing temperature
Under vacuum (2×10^{-6} mbar)	W32	40 ± 8 nm	850 °C

Table 4.2 Nanowires annealed at different temperatures by Method 1.

Nanowire	Diameter	600 °C	800 °C	850 °C	900 °C
W1	15 ± 3 nm	√	√	√	√
W2	25 ± 4 nm	√	√	√	√
W3	40 ± 8 nm	√	√	√	√
W4	50 ± 10 nm	√	√	√	√

Table 4.3 Nanowires used for *in situ* TEM observations of annealing process (Method 3)

Nanowire	Diameter	700°C	800°C	850°C	900°C	1000°C	1100°C
W11	15 ± 3 nm	√	√	√			
W21	25 ± 5 nm		√	√	√		
W31	40 ± 8 nm	√	√	√	√		
W41	50 ± 10 nm		√	√	√	√	√

Table 4.4 *In situ* TEM observation of annealing process (Method 3) for tungsten nanowire and tungsten-carbon core-shell nanowire.

Nanowire	850	900 °C	1500°C
W31	√	√	
Tungsten-Carbon core-shell nanowire (W-C)		√	√

4.3 Results and discussion

4.3.1 *In-situ* TEM observation of annealed nanowire

Figure 4.5 shows the bright field and dark field images of a 40nm nanowire (W32) before annealing. The polycrystalline wire comprises grains with different crystallographic orientations [Onn 2006]. From the micrograph, the grain size ranges from about 4 to 20 nm. After annealing at 850°C for 10 min (by Method 2), significant structural changes were observed from the bright-field and dark-field images in Figure 4.6 and Figure 4.7, as follows.

1) Irregular grains in the original nanowire have transformed to larger grains of size w in the radial direction, and length l (Figure 4.6 (a)).
2) In most of the cases, the new grains straddle the nanowire diameter d ($w = d$, e.g. grains A & B in Figure 4.6 (a)). Such grains will be termed "columnar grains" in this thesis.
3) In a few cases, the radial width w is smaller than d (e.g. grain C in Figure 4.6 (a)). The nanowire regions containing such grains will be termed "non-bamboo sections" in this thesis.
4) Some nanowire regions only have columnar grains where grain boundaries traverse the nanowire normal to its axis. Such nanowire regions are called "bamboo sections" (Figure 4.7 (a)).
5) The inset image of Figure 4.7 (a) shows the diffraction pattern of a bamboo section. Compared to the diffraction pattern of the original nanowire in the inset image of Figure 4.5 (a), the variety of crystallographic orientations is significantly reduced. It stems from the fact that there are fewer grains compared to the original wire in the selected area.

6) From Figure 4.7, it is also observed that grain grooves were formed between adjacent columnar grains along the line where a grain boundary intersects the nanowire surface.

Based on these observations, the evolution of the structural change is proposed as follows (Figure 4.8).

i.) When a polycrystalline nanowire of diameter of d (Figure 4.8 (a)) is annealed at a high temperature T, (e.g. $T < 850°C$ for the nanowire of 40nm in diameter), grain growth occurs (Figure 4.8 (b)). This arises because the polycrystalline nanowire contains a large number of grains and grain boundaries, that give rise to large excess free energy, which provides a significant driving force for grain boundary migration that can lead to grain growth [Fecht 1990] with a strong tendency to transform into a typical configuration with coarser grain size and fewer interfaces at elevated temperature [Klement 1995]. As a result, the mean grain size in nanowire becomes larger, while the grain size range is reduced. In Section 4.3.2, the rate of grain growth will be analyzed based on the measured mean grain size.

ii.) When a columnar grain is formed, grain boundary diffusion in radial direction r terminates (Figure 4.8 (c)). Further annealing of the nanowire only results in boundary diffusion between this new grain and its neighbors. By consuming the neighboring smaller size grains, the columnar grain can continue to grow by expanding along the axial direction x. When neighboring columnar grains impinge together, in order to minimize their boundary energies, they will form vertical grain boundaries at the impingement sites, (by minimizing the boundary areas) creating the bamboo-section (L_B) in nanowire. Since the bamboo sections are formed along the nanowire simultaneously, the whole nanowire consists of bamboo-section (L_B) and non-bamboo section (L) as shown in Figure 4.8 (c). As

annealing progresses, the range of L_B increases as columnar grains expand. Finally a bamboo-like nanowire is formed as shown in Figure 4.8 (d). In section 4.3.3, this evolution of bamboo-like nanowire will be analyzed by the grain growth model.

iii.) Once the nanowire becomes bamboo-like, grain grooves are formed between two adjacent columnar grains, so that the resultant of the two surface tensions (γ_s) and the vertical grain boundary tension (γ_b) will vanish along the line intersection (Figure 4.8 (e)). The formation of the grain groove can be attributed to the tendency of a vertical grain boundary to shrink in order to reduce its area and the free energy, so that the grains become pinched-off and spheroidized [Mullin 1957]. In section 4.3.4, the evolution of grain grooving will be analyzed in a kinetic approach developed by Klinger and Rabkin [Klinger 2005 a, b].

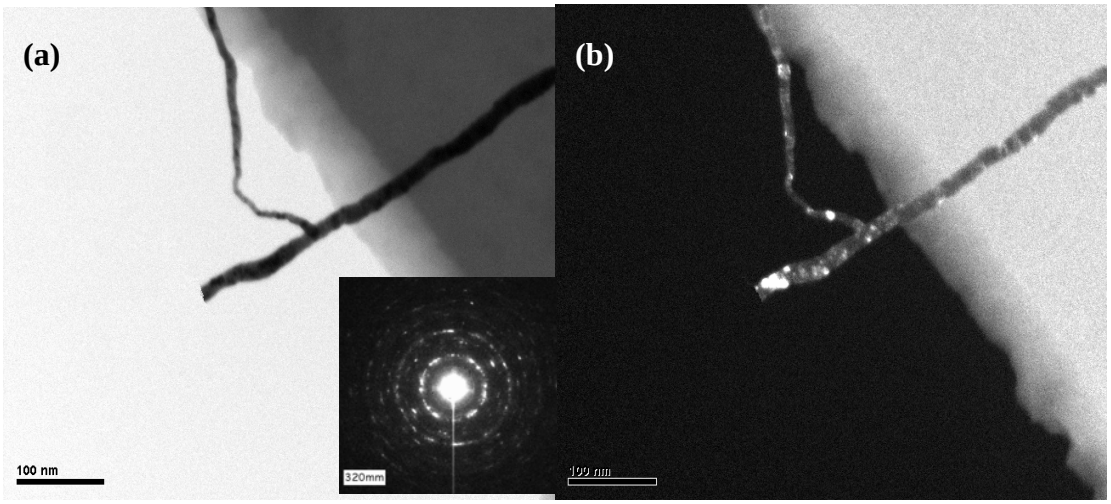

Figure 4.5 (a) Bright-field image and (b) dark-field image of nanowire before annealing.

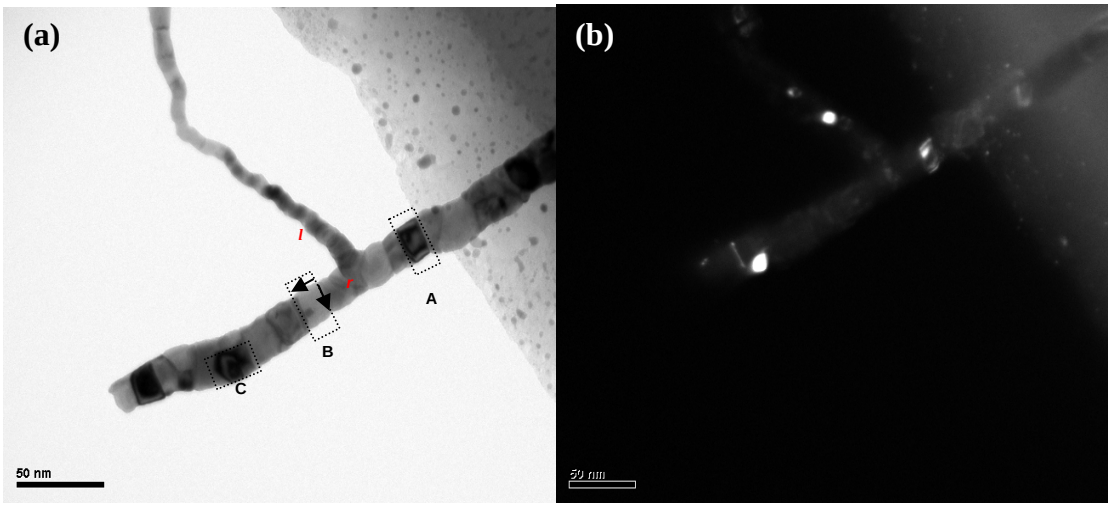

Figure 4.6 (a) Bright-field image and (b) dark-field image of nanowire annealed at 850°C (Method 2).

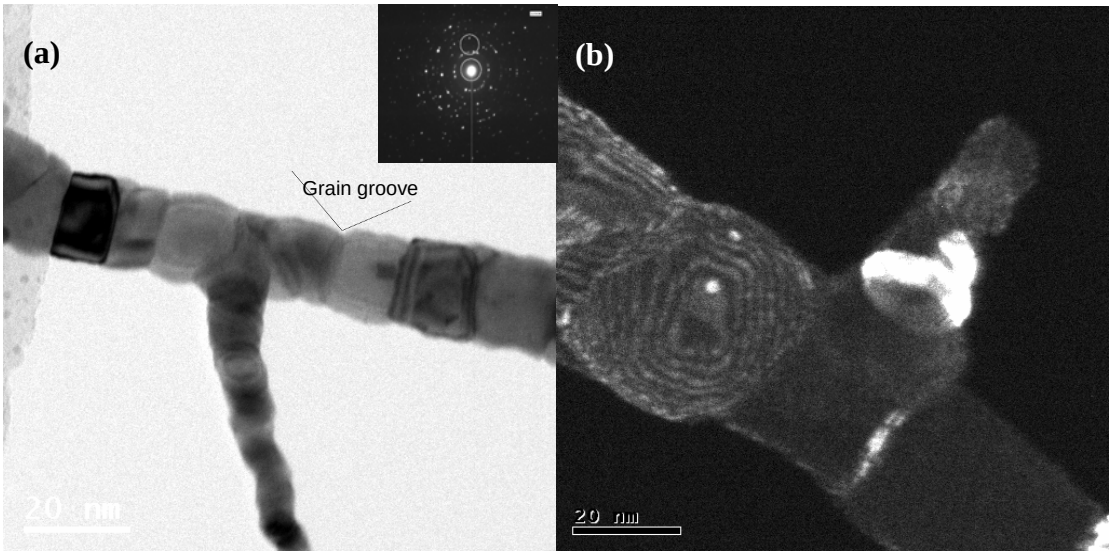

Figure 4.7 (a) Enlarged bright-field image and (b) dark-field image of nanowire annealed at 850°C (Method 2).

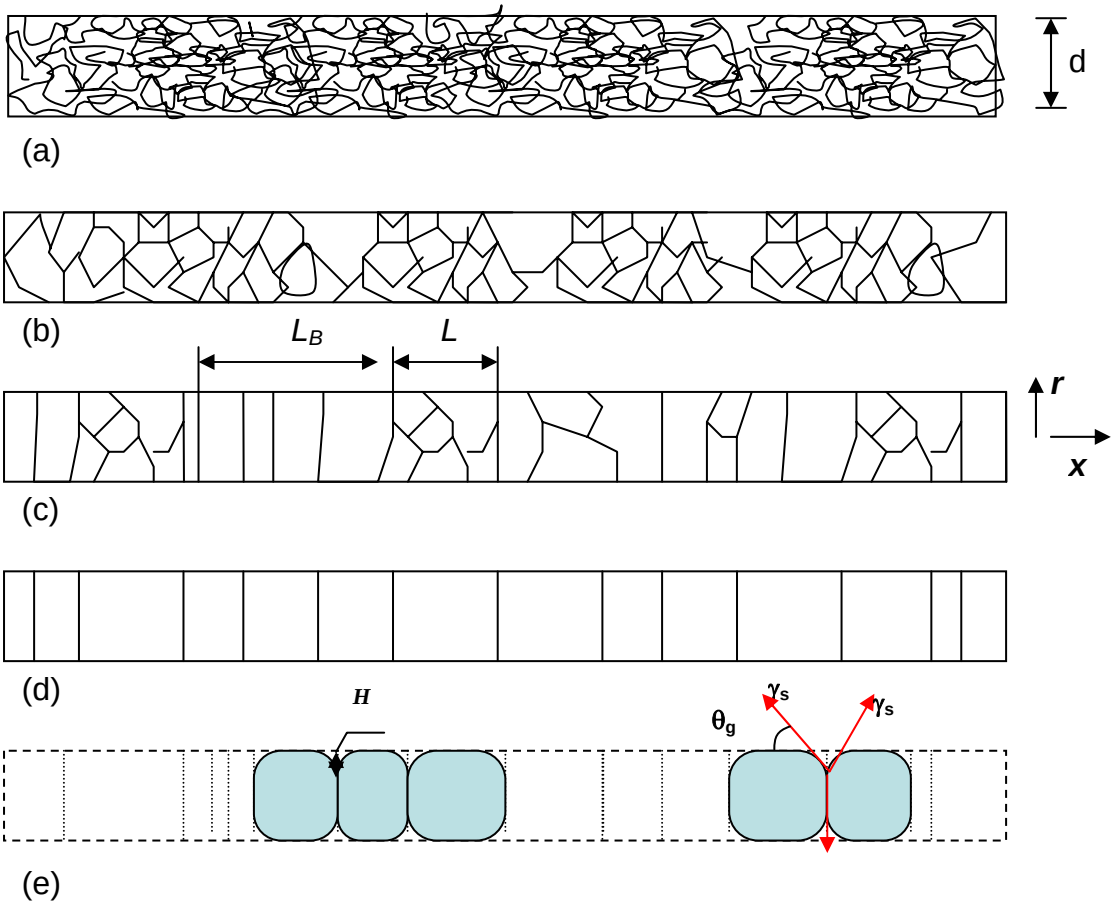

Figure 4.8 Schematic showing evolution of grain structure in a nanowire of diameter *d*.

4.3.2 Grain growth rate in nanowire

Generally, in a thin film structure (2D system), the excess free energy ΔG caused by the grain boundary can be expressed as [Porter 1992]:

$$\Delta G = 2\gamma V_m / r \qquad (4.8)$$

where γ is the grain boundary energy, V_m is molar volume of the grain, and r is the curvature of the grain boundary. This free energy difference can be thought of as a force pulling the grain boundary towards the grain with the higher free energy. The pulling force per unit area of boundary can be expressed as [Porter 1992]:

$$F = \frac{\Delta G}{V_m} \ (\mathrm{Nm^{-2}}) \qquad (4.9)$$

Therefore velocity of grain boundary under per unit driving force can be written as [Porter 1992]:

$$v = MF \tag{4.10}$$

where M is the mobility rate of the boundary. M is a temperature dependent parameter, which obeys an Arrhenius type relationship of the form [Turnbull, 1951]:

$$M = M_0 \exp(-\frac{E_a}{RT}) \tag{4.11}$$

where E_a is the activation energy for boundary mobility, and M_0 is the mobility constant which depends on the material only.

Assuming that the mean radius of curvature of the grain boundaries is proportional to the mean grain diameter $\overline{D}$, then the mean velocity of the grain boundary, which is used to express the grain growth rate ($d\overline{D}/dt$), can be written as [Burke 1952]:

$$\bar{v} \cong \frac{d\overline{D}}{dt} = \alpha M \frac{2\gamma}{\overline{D}} \tag{4.12}$$

where α is a small geometric constant.

To determine the grain growth rate in the annealing process, the mean grain diameter $\overline{D}$ of sample W31 was measured from DF images captured at annealing temperatures of 700°C and 800°C (by Method 3). The result is shown in Figure 4.9(a). It can be seen that over the span of 20 minutes, the mean grain diameter increased from 21.8nm to 27.2 nm, and from 27.8 nm to 37.6 nm, at 700°C and 800°C, respectively. From this result, the grain growth rate can be extrapolated as shown in Figure 4.9(b). In the figure, for both temperature conditions, the grain growth rates are seen to decrease monotonically with time since the total excess free energy within the nanowire decreases as the grains grow. The relationship between $d\overline{D}/dt$ vs. $\overline{D}^{-1}$

is plotted in Figure 4.9(c). From Equation 4.12, the grain growth rate should be proportional to $\overline{D}^{-1}$ and approaches zero as $\overline{D}^{-1} \rightarrow 0$. However, in Figure 4.9(c), at both temperatures, extrapolation of the grain growth rate as $\overline{D}^{-1} \rightarrow 0$ leads to negative $d\overline{D}/dt$ values. Note that Equation 4.12 was derived for a thin film structure (2D system) [Burke 1952], where the grain can continue to grow without limit. If there is a limiting grain size, Equation 4.10 will be modified as:

$$v = M(F - C) \qquad (4.13)$$

where C is a constant for the material. This alternative empirical analysis was given by Grey and Higgins [Grey 1973] when they found a cessation of grain growth at a limiting value in some two-phase thin film structures, where the dispersion of second-phase particles will reduce the growth rate of the grain by the Zener pinning pressure.

In the case of a nanowire, it was observed that radial grain growth terminates at the nanowire surface, so there is a radial limit given by the nanowire diameter. Therefore, we apply Equation 4.13 to describe the grain growth process in a nanowire, where C accounts for the limiting grain size due to the nanowire surface.

If Equation 4.13 is incorporated into Equation 4.12, then the grain growth rate becomes:

$$\frac{d\overline{D}}{dt} = M(\alpha\frac{2\gamma}{\overline{D}} - C) \qquad (4.14)$$

Figure 4.9(c) shows that the results are in good agreement with a linear relationship of the form $d\overline{D}/dt = A\,\overline{D}^{-1} + B$ at both 700°C and 800°C. From Equation 4.14, $A = 2M\alpha\gamma$ and $B = -MC$. Since $M_{700°C} < M_{800°C}$, then A(700 °C) < A(800 °C) and B(700 °C) < B(800 °C). This feature is also consistent with our experimental results.

As C is a constant, from the fitting curves, we obtain $M_{700°C}/M_{800°C} \sim 0.24$, from which the activation energy of grain boundary mobility E_a can be determined as ~

187kJ/mol. This energy refers to the energy barrier that must be overcome in order for an atom to migrate through the grain boundary. The result is close to activation energy of 210 kJ/mol obtained from measurements of a tungsten wire [Almanstottef 1997] but less than 380 kJ/mol for a tungsten film [Kaur 1989]. This difference is probably caused by a stress-constrain effect on the grain growth rate in thin films. As a thin film is coated at the substrate, if the substrate exerts a tensile stress on the thin film, then its grain growth rate will be larger comparing to the cylindrical wire with free surface. In contrary, the grain growth rate in thin film will be smaller in the case of compressive stress from substrate. That is why the E_a in a tungsten wire [Almanstottef 1997] and in our nanowire are different to the measured value from thin films by Kuar *et al* [Kaur 1989]. A similar difference in the measured activation energy can be found in other metals like lead films and wires [Haessner 1978].

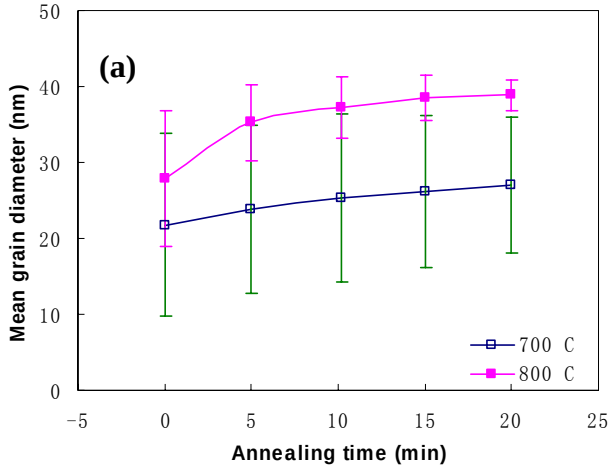

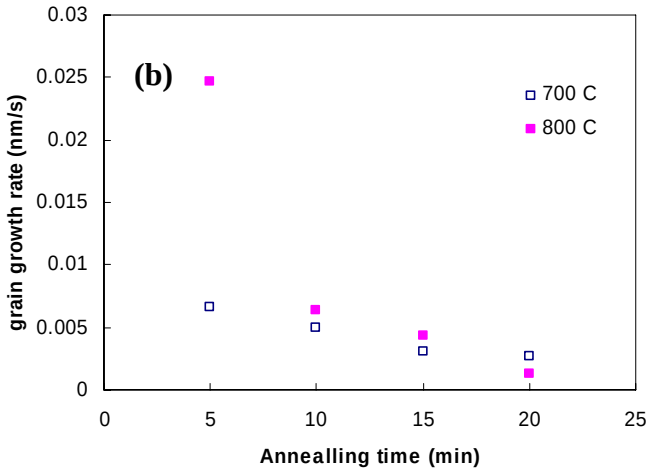

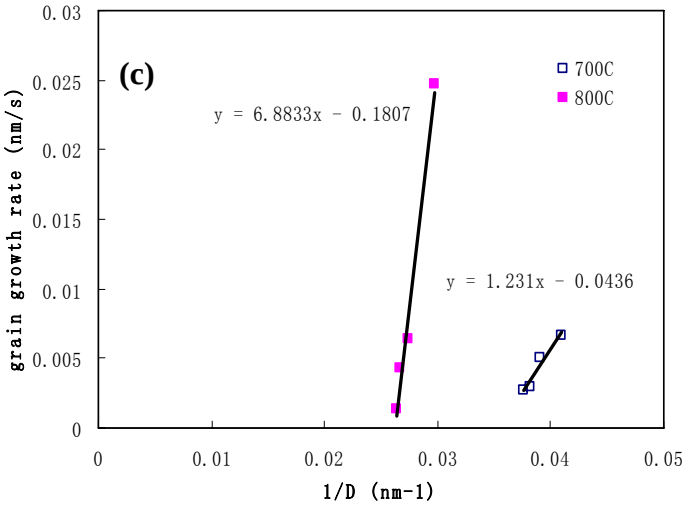

Figure 4.9 Time dependence of (a) mean grain diameter, $\overline{D}$ and (b) mean grain growth rate d$\overline{D}$/dt. (c) is the relationship between mean grain growth rate and 1/$\overline{D}$.

4.3.3 Bamboo-like structure formation in nanowire

Bamboo-like 1D microstructures have received much attention for decades, since the median time to electromigration-induced failure (MTTF) in such metal wires is significantly higher when they are used as interconnects in the semiconductor industry [Kinsborn 1980]. The reason for this behavior is because they contain only vertical grain boundaries along the wire axis so that the total "failure unit" [Cho 1989] by the electromigration is much less than regular polycrystalline metal wires in which the grain size is smaller than the wire diameter.

The pioneering simulation on the microstructural evolution of bamboo-like thin-film strips can be found in work by Walton's group [Walton 1991], where they used a model developed by Frost and Thompson *et al*. for grain growth in continuous thin films [Frost 1988(a), 1988(b), 1990]. Later Hau-Riege *et al.* found good agreement between the simulations and their experiments in laser annealing of Al and Cu interconnects [Hau-Riege 1999]. In the present work, we apply this simulation method to the Joule-heating annealing (Method 3) of FEIG tungsten nanowire.

In Walton's simulation work, they proposed a distribution relationship where the total area fraction of bamboo-structure section to the nanowire (f_{bamboo}) as a function of time is given by [Walton 1991]:

$$f_{bamboo} = 1 - \exp\left\{-2\frac{1}{L}\frac{M}{w}t\right\} \qquad (4.15)$$

where L is the initial length of non-bamboo section and w is strip width. In our bamboo-like nanowire structure, w is equal to the nanowire diameter d.

The fraction of bamboo section (f_{bamboo}) was estimated from the TEM images by dividing the total length of columnar grains to the wire length. Figures 4.10 (a) and (b) are the DF and BF images, respectively, of nanowire W31 (40nm in diameter). They

show the absence of columnar grains initially, and hence the non-bamboo section length (L in Equation 4.15) is equal to the length of nanowire.

After annealing at 700°C for 20 minutes, some columnar grains are formed as shown in Figures 4.10 (c) and (d) (e.g. grains A and B). Upon annealing the nanowire at 800°C for a further 20 minutes, more columnar grains are seen (Figures 4.10 (e) and (f)). From the analysis of such TEM images we can plot the rate of transformation to bamboo-like structure for FEIG nanowire in form of $\ln(1 - f_{bamboo})$ vs. (t/d) (Figure 4.11).

The data appears linear at both annealing temperature of 700°C and 800°C, demonstrating the asymptotic approach to a full-bamboo structure ($f_{bamboo} \to 1$) according to Equation (4.15) with a slope S equal to $-2M/L$. As L is the same at both temperatures, we obtain $M_{700°C}$ /$M_{800°C}$ ~ 0.24, which is similar to the result obtained from the grain growth analysis in Section 4.3.2. Therefore, this provides another simple approach to estimate the grain boundary mobility by using Walton's method, which is much easier compared to the Burke method.

Using Walton's method, we also plotted the relationship between $\ln(1 - f_{bamboo})$ vs. (t/d^2) for nanowires of different diameter d (w21, w31, w41) at 800°C (Figure 4.12). The slope S' becomes $-2Md/L$. Since both M and L are constant, the differences in S' are due to variations in diameter d. From the figure, $S'_{W21} : S'_{W31} : S'_{W41}$ ~ 29:40:52, which is close to the $d_{W21} : d_{W31} : d_{W41}$ = 25:40:50. The results suggest that the transformation rate to bamboo nanowire structure is faster the thinner the nanowire, which is not unreasonable as columnar grains may be expected to form rapidly to span a very thin nanowire.

So far, we have assumed that the nanowire eventually transforms to a *full* bamboo-like ($f_{bamboo} \to 1$) nanowire with increasing temperature and time. In fact, in the process of transformation, grain grooving simultaneously occurs at the vertical grain boundaries between columnar grains. With increasing temperature and time, grain grooving dominates the microstructural evolution in the form of shrinking grain boundaries (as shown in Figure 4.7). In this case, the kinetics of morphological changes are not only due to grain boundary diffusion but also include atomic migration on the free surface of the nanowire. To demarcate the point at which one or the other of the two processes dominates the morphological changes, a grain grooving temperature (termed as T_{GB}) is introduced in this thesis, at which temperature 90% of the nanowire is bamboo-like ($f_{bamboo} \sim 0.9$). Figure 4.13 shows a formed bamboo-like ($f_{bamboo} \sim 0.9$) nanowire in wire W31 after annealing at 850 °C for about 300 seconds. Below T_{GB}, it is assumed that the nanowire approaches a bamboo-like structure due to grain growth, while at $T_{GB,}$ it is assumed that grain grooving starts. This makes it convenient for us to observe the development of grooving at a selected temperature above T_{GB}.

With experimental Methods 1 and 2, T_{GB} is the measured annealing temperature resulting in $f_{bamboo} \sim 0.9$ for the entire nanowire. With Method 3, T_{GB} is simulated based on the corresponding stress current which results in $f_{bamboo} \sim 0.9$ in the middle section of the nanowire (~1μm length).

Figure 4.14 shows T_{GB} (Method 1) of nanowires of different diameters (W1,W2,W3,W4). It clearly shows that T_{GB} increases with nanowire diameter. The result reaffirms the conclusion from Figure 4.12, i.e., the rate of transformation to bamboo structure in a thinner nanowire is much faster than in a thicker nanowire.

From the definition T_{GB}, if f_{bamboo} = 0.9 and t =10 minutes are defined, according to Equations 4.15 and 4.11, then $1/T_{GB}$ should be proportional to $\ln(d)$. Such a linear relationship can be found in the fitting curve shown as an inset in Figure 4.14, which means that our observed T_{GB} for nanowires of different diameters are in agreement with the prediction by Walton's theory.

One application of T_{GB} is to calibrate the temperature in the Joule-heated nanowire, since it is difficult to measure the temperature of a nanowire with Method 3. The detailed calibration procedure can be found in Appendix B.

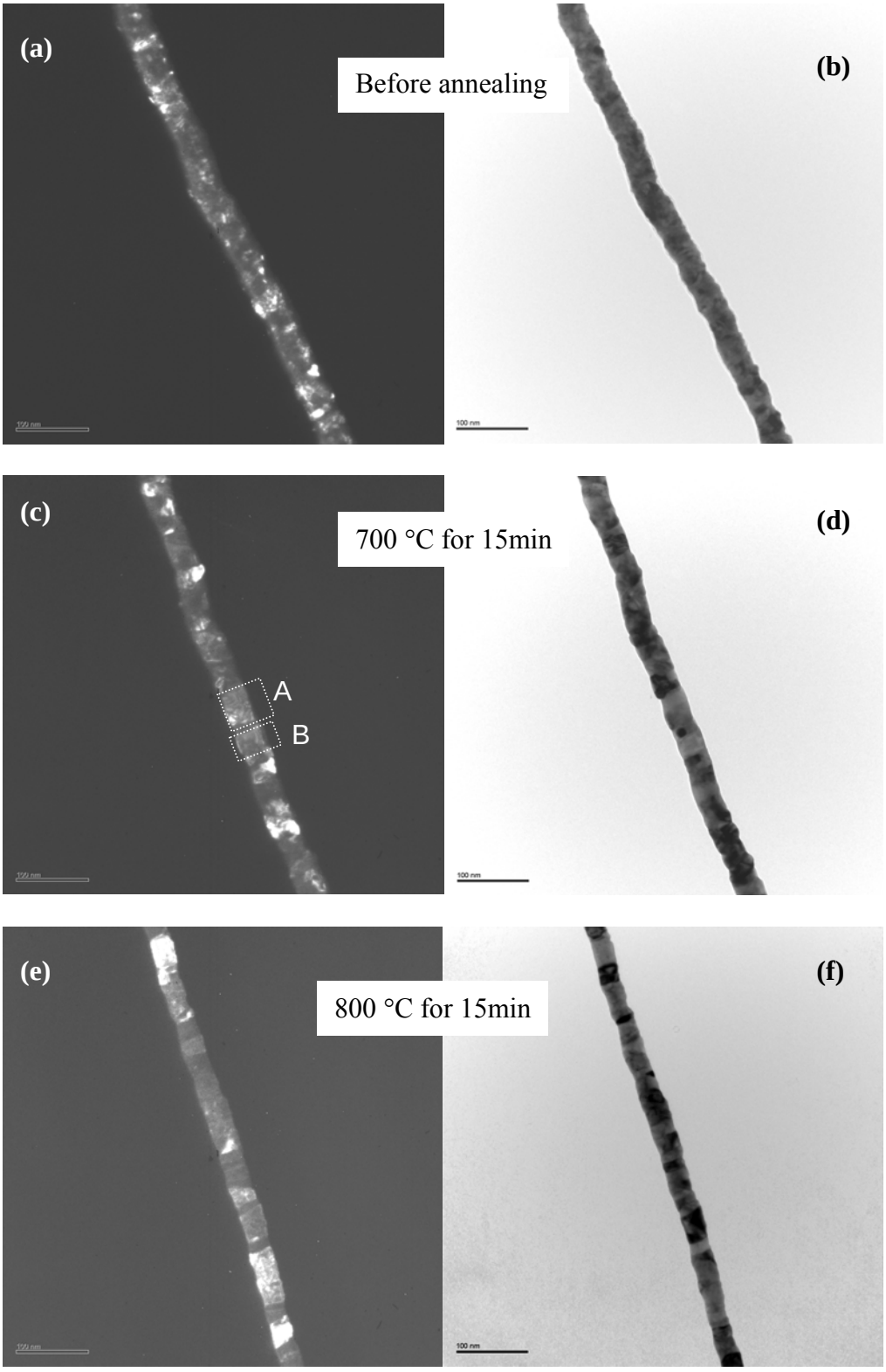

Figure 4.10 Dark field and bright field images of nanowire (W31) before it annealing ((a),(b)) , after it annealing at 700°C for 15minutes ((c),(d)) and at 800 °C for 15 minutes. ((e),(f))

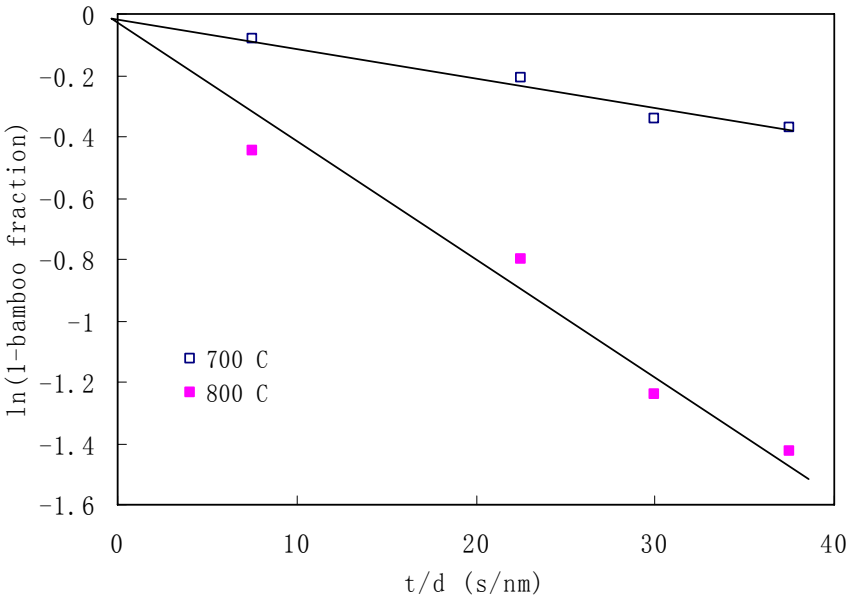

Figure 4.11 Relationship between $\ln(1-f_{bamboo})$ and (t/d) for nanowire W31.

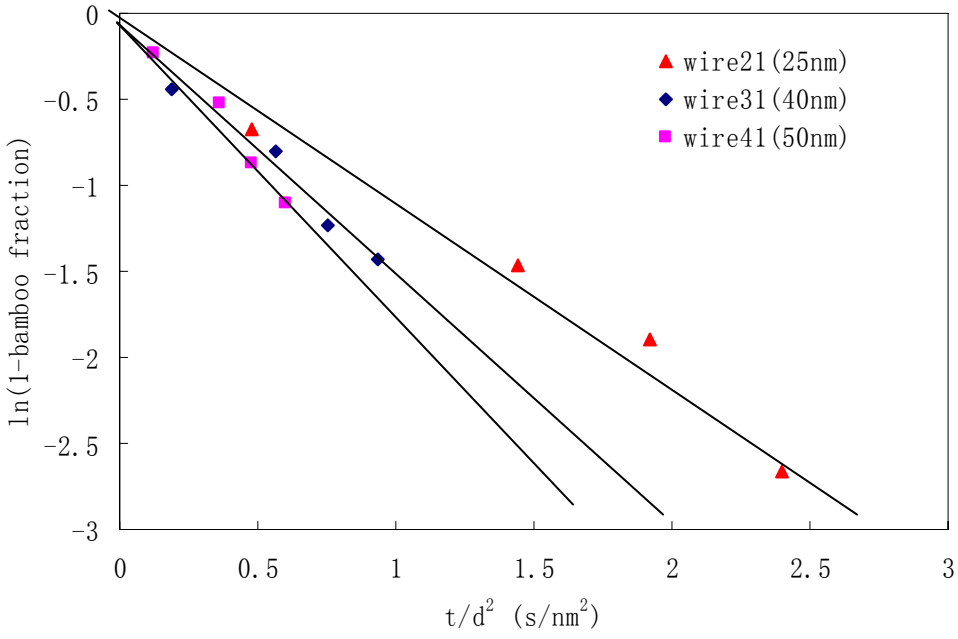

Figure 4.12 Relationship between $\ln(1-f_{bamboo})$ and (t/d^2) for nanowires of different diameter *d* (w21, w31, w41) at 800°C.

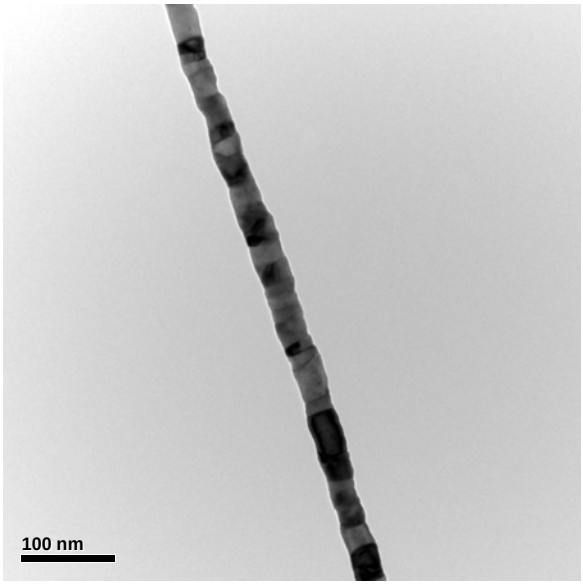

Figure 4.13 Nanowire (W31) annealed at 850°C for 300 seconds, shows a nearly-bamboo structure.

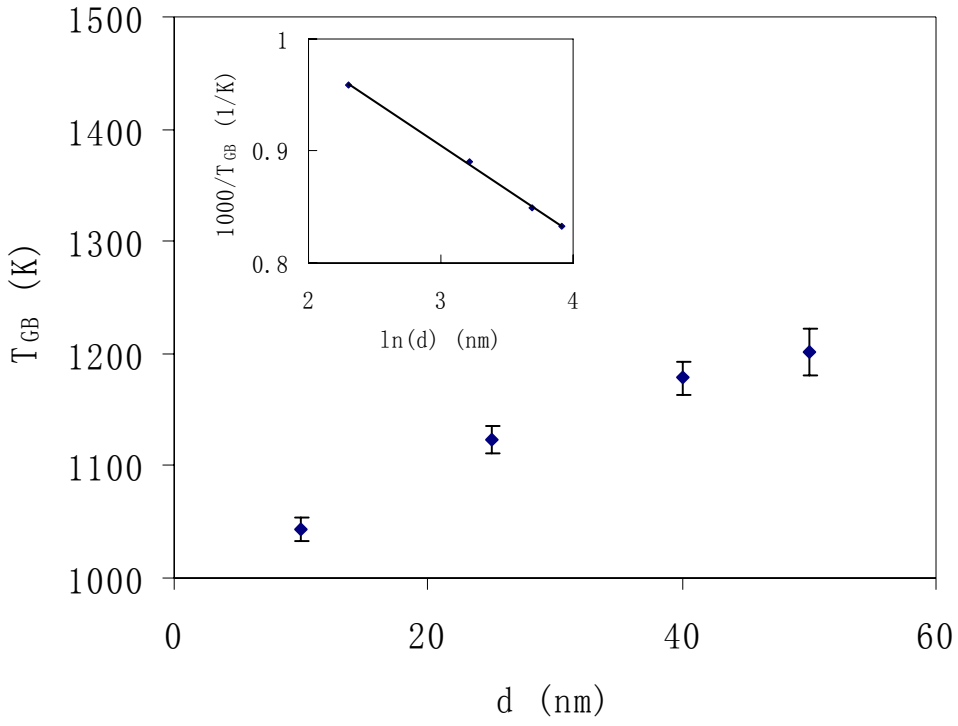

Figure 4.14 Relationship between T_{GB} and d of W1-W4. Inset shows a plot of $1000/T_{GB}$ vs. ln(d).

4.3.4 Grain grooving mechanism in nanowire

The grain groove process was firstly analyzed by Mullins in 1957 [Mullins 1957]. He showed that grain grooving on a metal surface is accomplished by material transport mainly through surface diffusion especially at the beginning of the grain grooving process. Mullins's theory was initially developed for grooves on a planar surface and later it was extensively applied to grooving at thin-film surfaces [Dunn 1966, Frost 1990, 1992]. According to his theory, the relationship between the diffusion flux of metal surface (J_s) and the grove profile is given by:

$$J_s = -\frac{\delta_s D_s \gamma}{KT}\frac{\partial K}{\partial s} = -\frac{B}{\Omega}\frac{\partial K}{\partial s} \qquad (4.16)$$

where δ_s, D_s and γ are the thickness of the surface layer in which the diffusion process occurs, the surface diffusion coefficient, and the surface energy, respectively. K is the curvature of grooving surface, s is the arc length along the groove profile, and B is the so-called Mullin's coefficient:

$$B = \frac{\delta_s D_s \gamma \Omega}{KT}. \qquad (4.17)$$

Recently, Klinger and Rabkin [Klinger 2005a, 2005b 2006] showed that the evolution of grain grooving in a cylindrical nanowire is faster than for a thin-film structure. They attributed this phenomenon to the geometrical effect which is associated with the additional curvature of a cylindrical nanowire. As the grain groove develops, the variation of the local radius of the deformed wire in the groove region becomes more and more significant and thus provides an additional driving force for surface diffusion, which may accelerate the groove evolution. Based on this mechanism, they calculated the groove profile by adding a consideration of the variation of the primary wire diameter in the groove region. In their theory, the mean curvature K of the cylindrical surface was expressed as:

$$K = -\frac{\partial_x^2 R}{(1+(\partial_x R)^2)^{3/2}} + \frac{1/R}{(1+(\partial_x R)^2)^{1/2}} \qquad (4.18)$$

where R is the cylinder radius, x is the distance along the cylinder axis (x = 0 corresponds to the grain bound plane). The shape of the grooved cylinder, which is a body of revolution, can be described by a function of $R(x, t)$ and follows the condition of mass conversation:

$$\partial_t R = -\frac{1}{R}\partial_x (RJ_s) = -\partial_x J_s - \frac{\partial_x R}{R} J_s \qquad (4.19)$$

where t is the annealing time.

The evolution of groove in nanowire structure can be simulated by solving Equations 4.16-4.19. The simulation details and conclusions can be found in Appendix D.

4.3.4.1 Shallow grain groove at beginning of grooving process

To date, there is no comparative study between the Klinger and Rabkin's theory and experimental results. Therefore, based on their theory, the groove profile measured by TEM will be quantitatively analyzed in this section.

Groove angle θ_g and depth of groove H (Figure 4.8e), which are used to describe the groove profile can be measured from TEM image. For example, for a typical grain groove of nanowire W31 shown in Figure 4.15, the measured mean values of θ_g and H are about 20.5° and 3.6nm, respectively. The annealing time and temperature are 100 seconds and 900°C, respectively. The mean radius of nanowire R_0 is 20 nm.

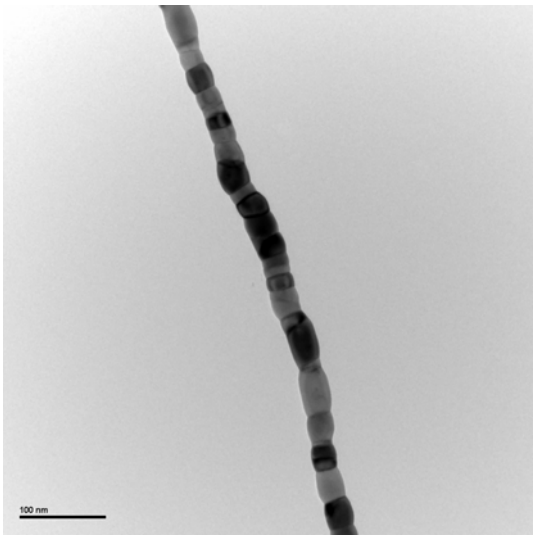

Figure 4.15 SEM image of nanowire annealed at 900°C for 100 sec.

In Mullins's coefficient Equation (4.17), $B = \frac{\delta_s D_s \Omega \gamma}{kT}$. From the known surface energy γ value of tungsten of 2830 ± 470 ergs/cm^2 at 1500°C, and a measured temperature dependent factor of ($d\gamma/dT$) ~ 0.13 ergs/cm^2/°C [Hodkin 1970], the derived γ for tungsten at 900°C is about 2920 ergs/cm^2. The atomic volume Ω for tungsten is 1.57×10^{-23} cm^3 according to the lattice parameter. Since the surface area per atom (A) is about 10^{-15} cm^2/atom for tungsten [Barbour 1960], the number of atoms per unit surface area, ν=1/A=10^{15} cm^{-2}, from which $\delta_s = \Omega\ \nu \sim 10^{-8}$cm.

The surface diffusion coefficient D_s can be expressed as:

$$D_S = D_0 \exp\left\{-\frac{E_a}{kT}\right\} \qquad (4.20)$$

At 900°C = kT ~0.1eV. Taking the value of surface activation energy E_a = 3.14eV [Barbour 1960, Philip 1960] and diffusivity constant D_0 of about 4 cm^2/sec [Barbour 1960], we get $D_s \sim 2.17\times10^{-13}$ cm^2 s^{-1}. The value corresponds to the diffusion coefficient of bulk tungsten metal [Barbour 1960]. Therefore, Mullin's coefficient of tungsten is $B \sim 2.84\times10^{-28}$cm^{4}s^{-1}.

Now we use this data (B) to compare with Klinger and Rabkin's theory. Since groove depth H (~3.2nm) is much smaller nanowire radius, (20nm) then H follows Equations D.14-D.15. As the annealing time is short, ($Bt/R_0^4 \sim 2\times10^{-1} << 1$, if B is estimated to be in the order of $10^{-28}cm^4s^{-1}$), we then use equation D.16 to calculate B as $B\sim 3.42\times10^{-28}cm^4s^{-1}$ where $m = \tan(\theta_g) \sim 0.3$.

As the two results are almost the same, therefore equation D.16 was used to describe the groove profile of our nanowire at the beginning of grain grooving. (Mullin's condition: $Bt/R_0^4 << 0.1$). Based on this equation, a method is proposed to find the surface diffusion coefficient (D_s) of the nanowire as follows:

1) Once a bamboo-like nanowire is formed, it is continuously annealed at above T_{GB} (e.g., T_{GB} + 50°C) for a short period (~ 10^2 seconds in tungsten) until a shallow groove at nanowire surface is observed.
2) The mean groove depth (H) and equilibrium angle (θ_g) are measured from TEM images.
3) Then Mullin's coefficient B is calculated according to Equation D.14, and finally D_s can be obtained.

Figure 4.16 shows the surface diffusion coefficient taken from nanowires of different diameters (W11, W21,W31,W41) at T_{GB}. A good linear relationship is observed between the $\ln(D_s)$ and $1/T_{GB}$ with a slope of about 3.6 cm^2/s. So D_s follows an expected Arrhenius relationship as given by Equation 4.20. This slope of 3.6 cm^2/s corresponds to the surface diffusivity constant D_0 for our tungsten nanowire which is closer to D_0 of $4.0cm^2/s$ for bulk tungsten metal [Barbour 1960, Bowden 1969]. This reaffirms Klinger and Rabkin's analysis for shallow groove profile (Equations D.14-D.16) as suitable for our tungsten nanowire annealing.

Up to now, we have used Mullin's assumption that the grain grooving is mainly due to the surface diffusion if the annealing time is not too long [Mullins 1958]. Now we validate this assumption.

In Mullins' calculation, a ratio σ was introduced for judging whether surface diffusion or evaporation predominates. σ is the profile area that would be transferred from below to above the original surface by surface diffusion alone divided by the profile area that is lost by evaporation. From his calculation,

$$\sigma = 0.38 \frac{(D_s \nu 2\pi M)^{\frac{1}{2}}}{\Omega \gamma^{\frac{1}{2}} p_0} t^{-\frac{1}{2}} \qquad (4.21)$$

where, M is the weight of the molecule, p_0 is the vapor pressure in equilibrium with a surface, and ν is the number of atoms per area. From Equation 4.21, it is noted that surface diffusion initially dominates the grooving process when t is small, but becomes of less relative importance as the groove develops. The essential temperature dependence of σ is controlled by $D_s^{1/2}/p_0$.

In the case of tungsten, using the same parameters as before and taking the p_0 value for tungsten as 4.27 Pa [Langmuir 1913], the calculated σ for tungsten is about $10^4\ t^{-1/2}$. This means when annealing time $t < 10^4$ sec (~ 10 hours), ($\sigma > 10^2$) only surface diffusion dominates the grain grooving process. Therefore in the above method, in order to find the surface diffusion coefficient, the annealing time to form the shallow groove of about 10^2 second is acceptable.

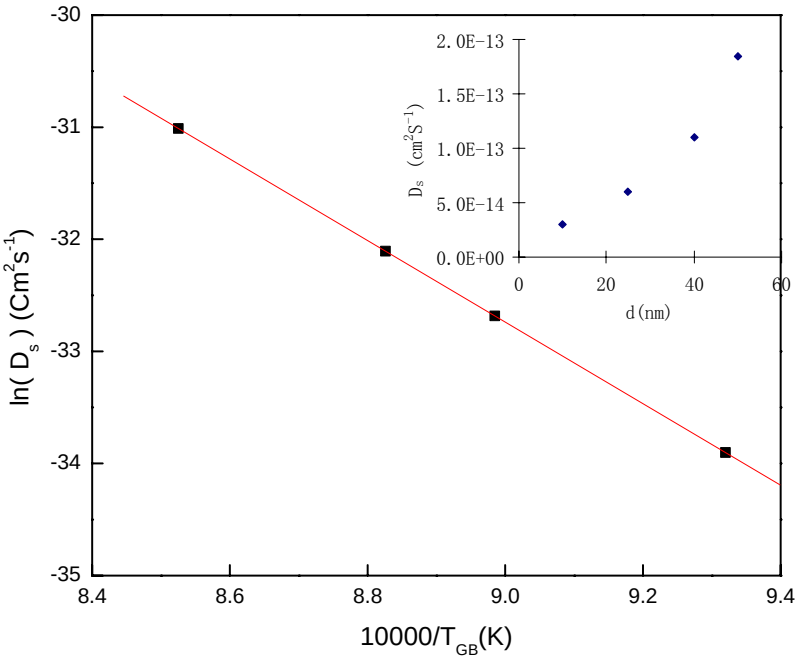

Figure 4.16 Plot of ln(D_s) vs. 10000/T

4.3.4.2 Development of grain grooving in nanowire

As annealing temperature and time increases, it was found that the grain grooves at the nanowire surface are further developed. Figure 4.17 illustrates the development of the grain grooving in nanowire (wire W31) at Joule-heating temperature of 900°C (Method 3).

After annealing for about 300 seconds, (Figure 4.17 (a)) the further increase in groove depth is not as significant, compared to image shown in Figure 4.15, taken after the nanowire has been annealed for 100 seconds. In Figure 4.17 (a), the term (Bt/R_0^4) is about $6\times10^{-1} < 1$, and according to Equation D.14–D.16s, the groove depth is nearly proportional to $T^{1/4}$. So only a minor groove depth developed in this period.

After annealing for about 1000 seconds, (Figure 4.17 (b) where (Bt/R_0^4) > 1, it was found that the depth of the groove has increased significantly. This means that

Equations D.14-D.16 are no longer applicable in this time range. According to Klinger and Rabkin's theory, (as shown in Figure D.2) the development of the groove will accelerate due to the additional driving force from the variation of the local radius of the cylindrical nanowire (Equation D.17). Thus, our TEM result supports this mechanism which is applicable for the developed groove at the nanowire surface.

In addition, based on their calculation (Equations D.1-D.4), Klinger and Rabkin analyzed the development of the grain groove. They showed that a critical ratio $(L/D)_{crit}$ (see "$(L/R_0)_{max}$" in Equation D.18, D.19) exists for every grain, above which the grain will break up from its neighbor, where L and D are the length and diameter of the columnar grain, respectively. Below this critical ratio, the equilibrium shape of grain can be achieved in a specific time (Figure D.5 – Figure D.6).

This feature can also be supported by our TEM results shown in Figure 4.17 (b). It can be seen that groove depth for larger-ratio (L/D) grain (e.g. grain A, B) is much larger than that of a smaller-ratio grain (e.g. grain C). Here, $(L/D)_A \sim 2.8$, $(L/D)_B \sim 3$ and $(L/D)_C \sim 1$. After nanowire has been annealed at 900°C for 1200 seconds, (Figure 4.17 (c)) this trend becomes more marked where the grooves at grains A and B develop much faster than at grain C. Finally, the nanowire breaks up at the grooved site of grain A after annealing for 1500 seconds (Figure 4.17 (d)). This means that the $(L/D)_{crit}$ for our nanowire is around 3. This is in good agreement with Klinger and Rabkin's simulation result ($\sqrt{3/2} < (L/D)_{crit} < \pi$) as shown in Figure D.5.

Based on above analysis, it can be concluded that our TEM results for the groove profile are in good agreement with the kinetic analysis by Klinger and Rabkin's theory both for shallow grooves ($(Bt/R_0^4) < 1$) and developed grooves ($(Bt/R_0^4) > 1$). In addition, we also successfully developed the method to characterize the surface diffusion coefficient parameter of the nanowire.

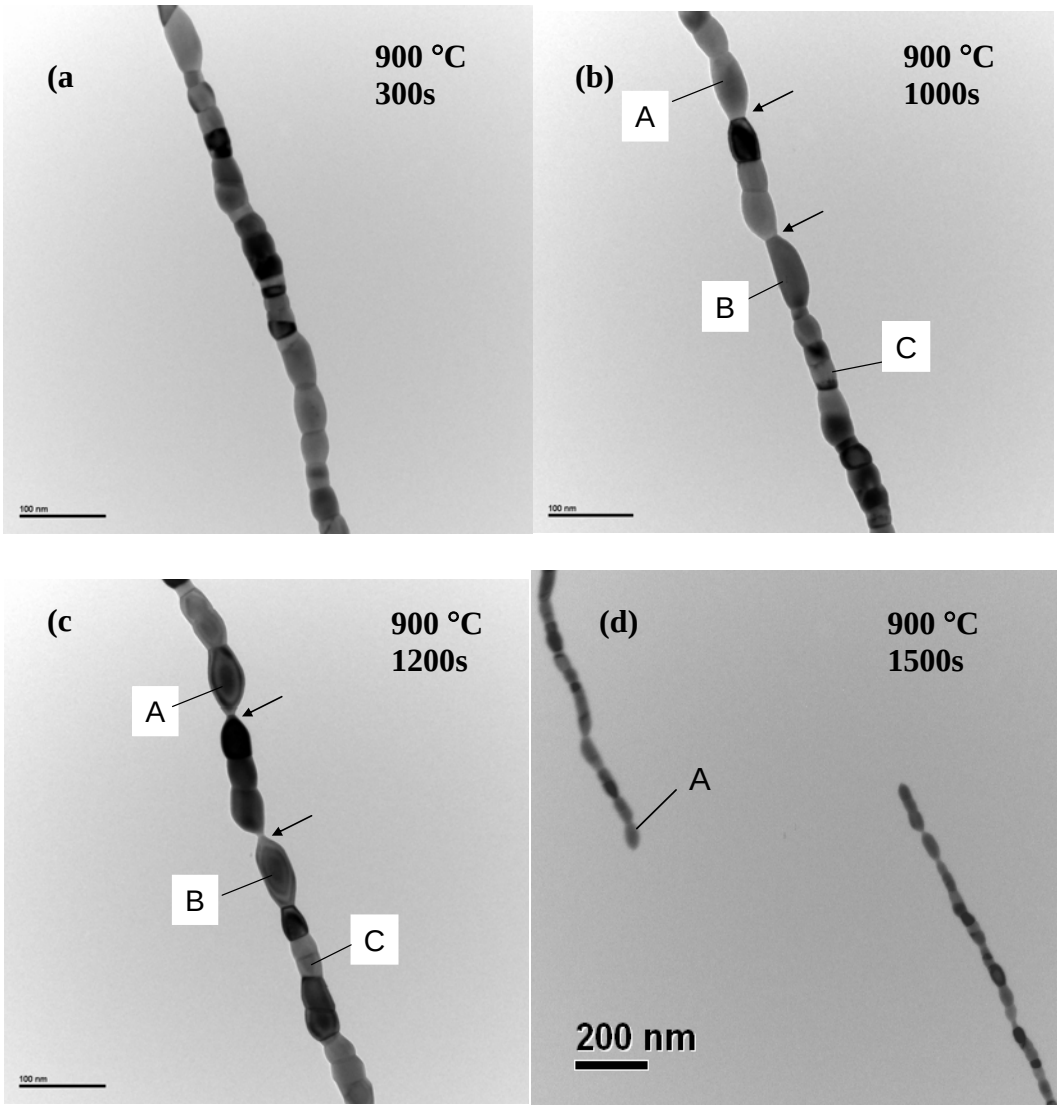

Figure 4.17 Evolution of grain groove in W31 at 900°C

4.3.5 Improved morphology stability performance of tungsten-carbon core-shell nanowire

From Figure 4.17 (d), the break-up of the polycrystalline tungsten nanowire results from the progression of grain grooving at an elevated temperature of about 900°C from Joule heating by the stress current of 20 μA passing through. Due to this morphology instability, the maximum current density for time-to-break-up of 1500 seconds for this free-standing nanowire (40nm diameter, 10μm length) is about 1.5×10^6 A/cm^2, which is much lower than a typical current density of about 10^7 A/cm^2 for time-to-failure of 20 minutes for thin film tungsten vias and plugs as a result of electromigration failure [Tao 1991].

For a free-standing nanowire, Joule heating can lead to high temperatures along the nanowire due to the limited thermal conductance of nanowires [Volz 1999], as compared to the temperature attained in thin-film vias or plugs in the presence of heat dissipation to substrate. Therefore, for high-aspect ratio free standing nanowire structure, even relatively low current densities can elevate the temperature sufficiently to cause failure by morphology instability, overtaking electromigration as primary failure mechanism. To date, this issue has not received much attention, although it could emerge as a challenge to the use of free-standing nanowires as interconnects in future nanodevice applications.

Since Joule heating is an unavoidable effect of passing current through a nanowire, one possible way to prevent morphology instability is to suppress the atomic diffusion at the nanowire surface. As such, a layer of carbonaceous material was coated along the entire length of a tungsten nanowire to form a core-shell structure. The coating was carried out by irradiation in the SEM to deposit

contamination onto the nanowire (Figure 4.18(a)). Two-terminal IV measurements carried out before and after coating show that the resistivity of the coating is much higher than that of the tungsten core.

When the W/C core-shell nanowire structure was stressed with a current of 20 μA (corresponding to an average core current density of ~1.5×10^6 A/cm^2) for 1800 seconds, longer than the time of 1500 seconds to break the uncoated tungsten nanowire, no necking is apparent in the W/C core-shell nanowire. The only notable difference is that the grains have become bigger as evident from Figure 4.18(b) and the inset dark-field image formed using part of the W(110) diffraction ring. In this instance, the length of the single crystal grain shown is about 400 nm which is much larger than the nanowire diameter. To arrive at this state, grain growth must have taken place in the tungsten core through atomic diffusion across the interfacial boundary. The position of the interfacial boundary can be estimated by observing the different diffraction patterns (SAED) emerging on either side of the boundary, as shown in Figure 4.18(c). The SAED pattern in Area II, which is towards to the middle of the nanowire where the temperature is highest, is clearly single-crystalline, as opposed to polycrystalline nature of Area I which is on the side closer to the nanowire anchor. From Figure 4.18(c), it is clearly seen that the grooving structure is not formed along the intersection between the interfacial boundary and surface of tungsten core. Thus morphology instability due to the grain grooving of the tungsten core has been prevented by the presence of the carbonaceous shell.

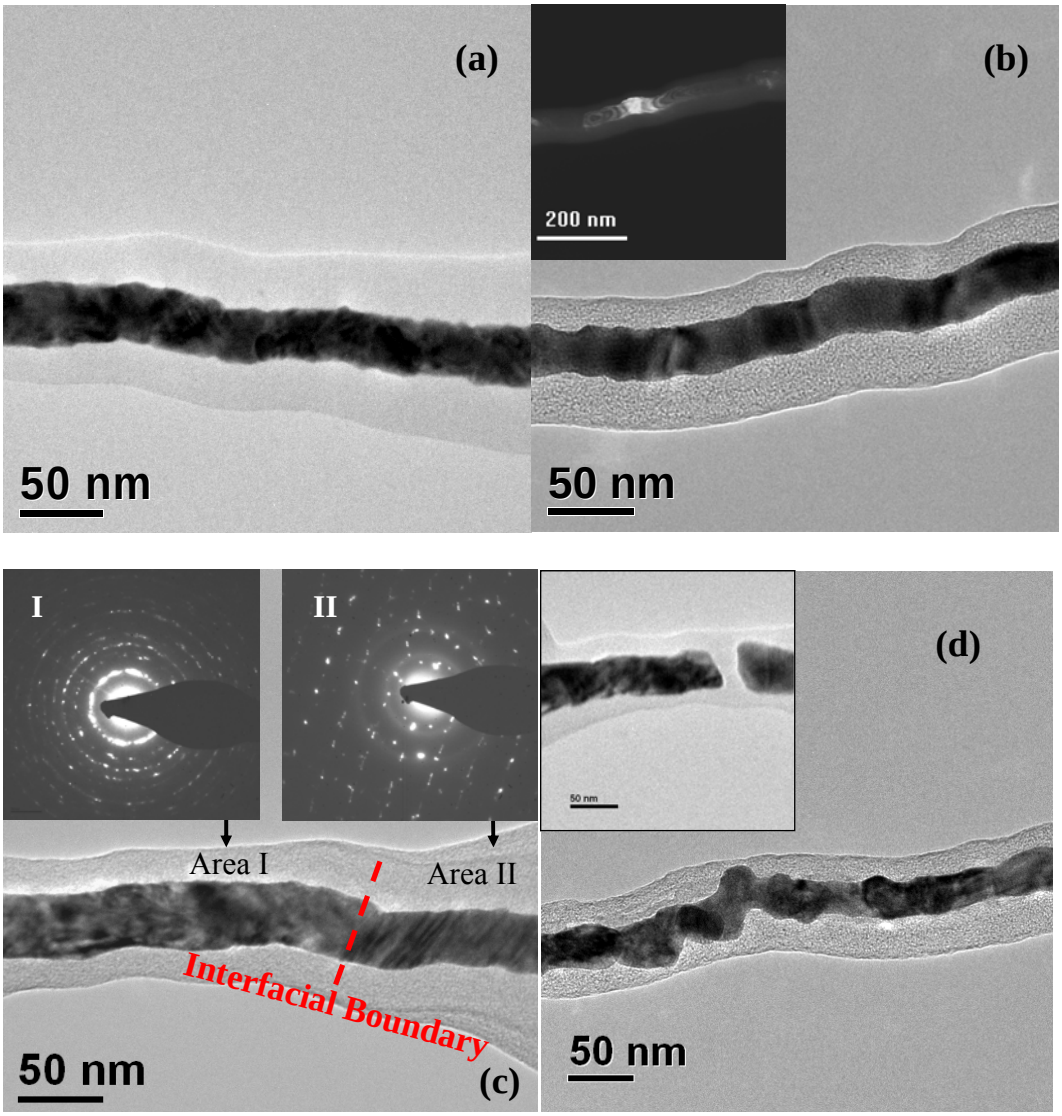

Figure 4.18 (a) Polycrystalline nanowire coated with a layer of carbonaceous contamination. (b) Middle of the nanowire after annealing at 20 μA for 1800 seconds. Inset shows the dark field image taken using a portion of the W(110) diffraction ring. (c) Interfacial boundary of the nanowire demarcates the polycrystalline portion towards the anchor (area I) and single-crystalline portion towards the middle (area II). (Inset images are the corresponding SAD patterns) (d) Nanowire after passing a current of 370μA for 300 seconds. Inset shows a void formed due to the electromigration in the nanowire.

It is known that grain grooving at a metal surface is accomplished by material transport through surface diffusion especially at the beginning of the grain grooving process [Mullin 1958]. Therefore, the prevention of the grain grooving in the W/C core-shell nanowire can be attributed to the inhibition of atomic diffusion at tungsten/carbon interface. This is different from the case of the free tungsten surface shown in Figure 4.17. According to the bond-order–length–strength (BOLS)

correlation theory [Sun 2006], the critical temperature of the phase transition is proportional to the mean atomic cohesive energy, which is the sum of the bond energy over all the coordination numbers of a given atom, and overheating (defined as increase in the melting temperature T_m) may occur in a substance (the W core here) when it is covered by another substance with higher T_m (the carbonaceous shell). Reaction of the carbon with tungsten at elevated temperature creates interface bonds of C and W, and the tungsten core is then overheated. We have simulated the temperature along the W/C core-shell nanowire based on experimental measurements of the thermal conductivity of the carbonaceous layer, which is about 3 W/(m·K), less than 10 percent of 40 W/(m·K) of tungsten nanowire. In the simulation, to determine the thermal conductivity of carbonaceous layer, we used a suspended MEMS device [Shi 2003] to first measure the thermal conductance of a Si nanowire of 300nm in diameter, then repeated the measurement of the thermal conductance after coating the Si nanowire with a carbonaceous layer of 20nm in thickness. The difference between two values is considered as the thermal conductance of the carbonaceous layer. At a stress current of 20μA (corresponding to an average core current density of ~1.5×10^6 A/cm^2), the simulated temperature at the middle of the W/C nanowire is about 850°C, only slightly lower than the peak temperature of the bare W nanowire. Although the temperature of the W nanowire is effectively unchanged after coating with carbonaceous material, since the melting point of the core has been raised by the additional carbonaceous layer, the atomic diffusion at tungsten/carbon interface will be inhibited at 850°C. Therefore grain grooving does not form in W/C nanowire unlike the case of the W nanowire at 900°C.

The stress current was increased in increments of 10 μA. At each current step, grain grooving in the W/C core-shell nanowire was not observed over a period of 10

minutes. The only observed change is a shift in the interfacial boundary towards the nanowire anchor as the single-crystal grain expands. When the stress current increased to about 370 μA (equivalent to an average core current density of ~3×10^7 A/cm^2), at which the corresponding simulated temperature in middle of the W/C nanowire is about 1400°C, a different form of morphology instability in the tungsten core started to take place, manifested as roughening of the nanowire as shown in Figure 4.18 (d). The inset image shows a gap (void failure) in a W/C nanowire after stressing at a current density of about 3×10^7 A/cm^2 for about 300 seconds. Real-time TEM observation of this gap developing (see video chip (Movie-1.avi) in attached CD: Appendix C) reveals that the void originated at a grain boundary site, where the metal ions are weakly bonded. It can be seen that material is depleted from the grain boundary and transported in the direction of the electron flow (right to left direction in the movie), which is a typical feature of the electromigration phenomenon. Due to the atom flux along the W core, the final broken ends of tungsten core are almost flat (Figure 4.18(d)). This is in contrast to the morphology of the broken ends of the uncoated bare W nanowire (see Figure 4.17 (c & d)). In the bare W nanowire, the diameter of the broken ends is much smaller than the average diameter of the wire itself, arising from the progressive shrinkage of the grain boundary grooved neck due to a dominating surface diffusion process.

4.3.6 Grain rotation during the grain grooving of the nanowire

During annealing of nanowire (W31) in the TEM using Method 3, it was observed that the diffraction contrast of individual grains keeps changing. In the attached CD (appendix C), The files Movie-2 (total duration 30s) and Movie-3 (total duration 10s) show the real-time development of the grain groove after having annealed the nanowire at 950°C for 5 min and 15min, respectively. In Movie-3, the grooves have developed much deeper than the grooves shown in Movie-2.

In both movies, the frame rate is 0.3 sec, and hence any event faster than the temporal resolution of 0.3 sec cannot be captured. But from the two movies, we can observe significant changes in the bright-field contrast of individual grains during annealing. The mechanism underlying this phenomenon may arise from the rotation of individual grains around the nanowire axis. The observed changes in contrast arise from variations in the amplitude of the diffracted beam when the beam passing through the specimen.

It is known that, based on the two beam analyses (direct and diffraction beams) in the TEM, the total electron wave amplitude can be represented by the Howie-Whelan equations which describe the change in amplitude of the direct beam ϕ_0 and the amplitude of the diffracted beam ϕ_g considering also dynamical effects arising from multiple diffraction [Fultz 2008]:

$$\frac{d\phi_g}{dz} = \frac{\pi i}{\xi_0}\phi_0 + \frac{\pi i}{\xi_g}\phi_0 \exp(-2\pi i s z) \qquad (4.22)$$

$$\frac{d\phi_0}{dz} = \frac{\pi i}{\xi_0}\phi_0 + \frac{\pi i}{\xi_g}\phi_g \exp(+2\pi i s z) \qquad (4.23)$$

where ξ_g and ξ_0 are the extinction distance for the direct and diffracted beams, respectively, which is the characteristic length for the diffraction vector g. They depend on the lattice parameters of the crystal grain. z corresponds to the thickness of the specimen, and s is the deviation parameter, defined as the vector pointing from the reciprocal lattice point to the place on the Ewald sphere – if the crystal is not perfect, local variations in $\mathbf{s}=s(x,y,z)$ will be present. In our experiment, z and s are the geometry parameters which correspond to the individual grain diameter and the grain surface curvature, respectively.

Each individual grain of our nanowire is barrel-shaped with a maximum diameter at the center of grain ($x = L/2$) and smallest diameter at the ends ($x = 0, L$). The surface of the grain can be considered as a sphere with curvature K. Changes in the amplitude of the electron beam as a result of changes in grain diameter (changes in the z parameter in Equations 4.22 and 4.23) seem less probable in our experiment as we did not observe any grain diameter changes in the direction normal to the incident beam even as the contrast changed from bright to dark and vice versa. Likewise, changes in the grain surface curvature (changes in the s) are also unlikely to account for this. Had the surface curvature changed, then we should observe the contrast fringe ring in the image which normally accompanies changes in surface curvature.

We also considered the possibility of nanowire motion as a possible. To test this hypothesis, we manually moved the nanowire in both lateral directions and found that the contrast of the nanowire did not change by such displacement. When we moved the nanowire along the electron-optical axis (direction parallel to the incident beam), the contrast was found to change but only for displacements larger than 10^3 nm. However, this observed change in contrast was also accompanied with defocusing of the nanowire. From the TEM movies, we found that the nanowire remained within

the depth of focus. Therefore nanowire drift (lateral shifts) and vertical vibrations (in/out of focus) are not the reasons for the dynamic changes in contrast in this experiment.

Based on above analysis, we conclude that the most likely reason is due to grain rotation during the grain grooving process. As the grain rotates, the crystallographic plane normal to the incident beams will change, and give rise to changes in the extinction distance ξ_g and ξ_0 of the grain. According to Equations 4.22 and 4.23, the contrast will thereby change. To demonstrate this, we manually tilted the nanowire, and hence the grains, around the wire axis, to observe changes in the image contrast. Figures 4.19 (a) and (b) show contrast differences of a bamboo-like nanowire before and after tilting ~2°, respectively. The contrast of grain A is seen to change from dark to the bright after tilting.

In fact, grain rotation which accompanies changes of the orientation difference between neighboring grains (misorientation) had been studied as an important phenomenon of microstructural development in polycrystalline metals.

In 1976, Herrmann *et al*. [Herrmann 1976] showed that a copper crystal ball (~100 μm in size) can "rotate" on a flat crystal plate in order to minimize their interfacial energies. The driving force is the reduction of boundary energy so that a minimum misorientation between the ball and substrate can be reached. They assumed the rotation was achieved by the diffusive flux of atom on the grain boundary.

Harris *et al*, [Harris 1998] directly observed the change of the grain orientation (grain rotation) during annealing of thin film gold (2D system). The driving force is considered as the aggregate energy gradient with respect to the misorientation for all the grain boundaries surrounding a particular grain. The observed grain rotation rate is

consistent with their proposed mechanism based on diffusion-limited grain boundary sliding in response to the variation of grain boundary energy with misorientation. Their results revealed that grain rotation exists in thin films at a later stage of microstructural development, which is similar to other reports [Randle 1993, Ke 1995, Shibayanagi 1996].

In addition, grain rotation is also observed in the "orientated attachment process" of 1D nanostructure which generally involves the attachment of multiple nanoparticles as building blocks in pearl-chain-like structures [Yang 2008, Zhang 2007, Liu 2004]. In such a process, the adjacent nanoparticles which share the same crystallographic orientation plane will finally fuse to each other. Otherwise nanoparticles could rotate for a thermodynamically favorable interfacial configuration to reduce the overall energy [Penn 1998a, 1998b].

In our nanowire system, a possible mechanism for grain rotation at high temperatures could be attributed to variations in the surface energy of the adjacent grains that share the same grain boundary. The driving force is provided by the aggregate energy gradient with respect to the miscorrelation. Hence the grain rotates in a manner that reduces grain boundary energy as grain boundary misorientation is minimized.

4.4 Summary

In this chapter, the polycrystalline tungsten nanowires were annealed in vacuum. Through *in situ* TEM, the structural transformation progress in nanowires is observed. The observation results were systemic analyzed in order to understand the mechanisms of grain growth and grain grooving in 1D nanowires structure. To improve the morphology instability of free standing polycrystalline nanowires, a

strategy has been developed by overcoating carbon layer on the nanowire surface. In the end of chapter, it was also observed that the grain rotates individually across the nanowire axis during the grain groove developing.

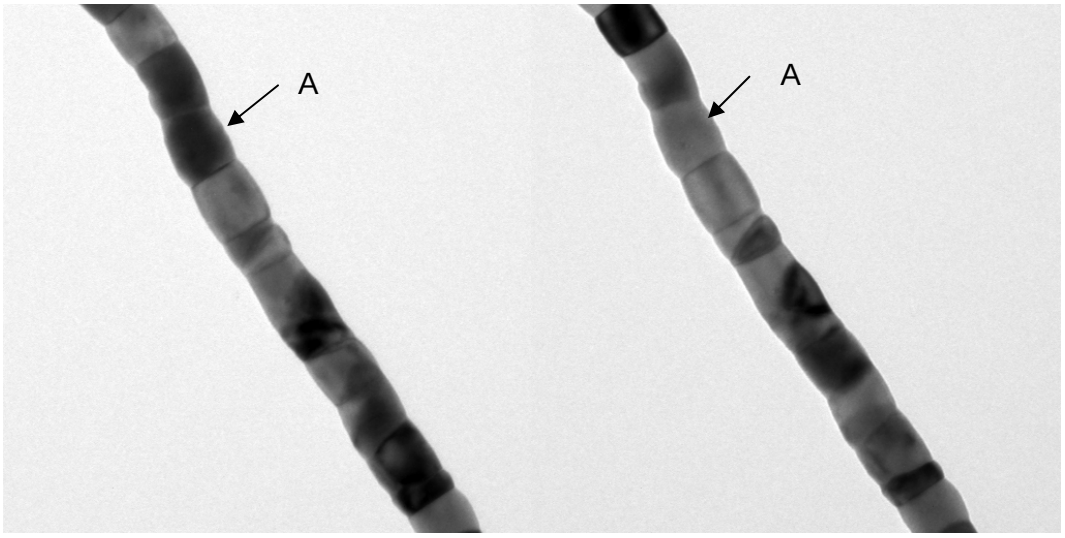

Figure 4.19 Nanowire (a) before and (b) after tilting for 2°.

Reference

Almanstottef J., Ruhleb M., (1997), *Int. J. of Refractory Metals & Hard Materials* **15**, 295.

Arzt E. and Nix W. D., (1991),*J. Mater. Res.* **6**, 731.

Barbour J. P., Charbonnier F. M., Dolan W. W., Dyke W. P., Martin E. E. and Torlan J. K., (1960), *Phys. Rev.* **117**, 1452.

Briant C. L. (1996), *Interface Science* **4**, 81.

Burgers W.G., (1941), *Handbunch der Metallphysik* **3**, 2.

Burke J. E., and Turnbull D., (1952), *Prog. Metal Phys.* **3**, 220.

Cho J. and Thompson C.V., (1989), *Appl. Phys. Lett.* **54**, 2577.

Dunn C. G., (1966), *Acta Metal.* **14**, 221.

Fecht H.J., (1990), *Phys. Rev. Lett.* **65**, 610.

Frost H. J., Thompson C.V., Howe C.L., and Whang J., (1988a),*Scripta. Metall.* **21**, 65.

Frost H. J., and Thompson C.V., (1988b), *J. Electron. Mater*. **17**, 447.

Frost H. J., Thompson C.V., and Walton D.T., (1990), *Acta Metall.* **38**, 1455.

Frost H. J., Thompson C.V., Walton D. T., (1992), "*Grain Growth in Polycrystalline Materials"* ed: Abbruzzese and Brozzo. Trans Tech Publns. p543

Fultz B., Howe J., (2008), *"Transmission Electron Microscopy and Diffractometry of Materials"* ed: Springer, ISBN: 978-3-540-73885-5

Grey E. A. and Higgins G. T., (1973), *Acta Metall.* **21**, 309.

Haessner F., (1978), "*Recrystallization of Metallic Materials",* ed: Dr. Riederer Verlag GmbH, Stuttgart.

Harris K. E., Singh V. V., King A. H, , (1998), *Acta Mater* **46**(8), 2623.

Hau-Riege C. S. and Thompson C. V., (1999), *Appl. Phys. Lett.* **75**, 1464.

Herreo J. G., *et al*, (1993), *Appl. Phys. Lett*. **62**(10), 1077.

Herrmann G., Gleiter H., Baro G., (1976),*Acta Metall.* 24, 353.

Humphreys F. J. and Hatherly M. (1996), *"Recrystallization and related annealing phenomena"* ed: Pergamon, Elsevier Science Ltd, , ISBN 0080418848.

Kaur I., Gust W., Kozma L., (1989) "*Handbook of Grain and Interphase Boundary Diffusion Data"* Vol. 2. ed: Ziegler Press, Stuttgart,.

Kinsborn E., (1980), *Appl. Phys. Lett.* **36**, 968

Klement U., Erb U., Sherik A.M. E., *et al.* (1995), *Aust, Mater.Sci. Eng. A* **203**, 177.

Ho S. S., Jun Y., Jae Y. S., (2007),*Appl. Phys. Lett.* **91**, 173106.

Ke M., Hackney S. A., Milligan W. W., Aifantis E. C., (1995), *Nanostr. Mater.* **5**, 689.

Klinger L., Rabkin E., (2005a), *Scripta Materialia* **53,** 229.

Klinger L., Rabkin E. (2005b), *Z Metallkd.* **96**(10), 1119.

Klinger L., Rabkin E., (2006), *Acta Metall.* **54**, 305.

Langmuir I., (1913), *Phys. Rev.* **2**(5), 329.

Liu B., Zeng H. C., (2004), *J. Am. Chem. Soc.* **126**, 8124.

Molares M. E. T., Balogh A. G., *et al.* (2004), *Appl. Phys. Lett.* **85**, 5337.

Morvath H. *et al*, (2007), *Microelectronic Engineering* **84**, 837

Mullins W. W., (1957),*J. Appl. Phys.* **28**(3), 333.

Mullins W.W., (1958), *Acta. Metall.* **6**, 414.

Oon, C. H., Thong, J. T. L., (2004), *Nanotechnology* **15**, 687-691

Penn R. L., Banfield J. F., (1998a), *Science* **281**, 969.

Penn R. L., Banfield J. F., (1998b), *Am. Mineral.* **83**, 1077.

Pichaud M., Muller A., Drechsler M. (1971), *Surf. Sci.* 26, 14.

Pierson H. O., (1992), *"Handbook of Chemical Vapor Deposition (CVD): Principle, Technology and application"* ed: William Andrew Inc. ISBN 0815513003

Randle V., (1993), *Phil. Mag. A* **67**, 1301.

Shi L., Li D.Y., Yu C. H., (2003**)**, *Journal of Heat Transfer* **125**, 881.

Shibayanagi T., Sumimoto K., Umakoshi Y., (1996),*Scripta mater.* **461**, 204-206.

Smith C. G., Ahmed H., Wybourne M. N., (1987), *J. Vac. Sci. Technol. B* **5**, 314.

Sun C.Q., (2007**)**, *Prog. Solid State Chem.* **35**, 1.

Tao J., Yong K. K., Pico C. A., Cheung N. W., (1991), *IEEE Electron Device Letters* 12, 646.

Thompson C.V. (1992), *"Grain growth in polycrystalline materials"* ed: Abbruzzese and Brozzo. Trans Tech Publns. p245

Turnbull D., (1951), *Trans. Met. Soc. AIME* **19**, 661.

Volz S.G., Chen G., (1999), *Appl. Phys. Lett.* **75**, 2056.

Walton D.T., Frost H. J., Thompson C.V., (1991), *Appl. Phys. Lett.* 61, 40.

Yang L., Yang H., Yang Z. X., Cao Y. X., Ma X. M., Lu Z. S., (2008), *J. Phys. Chem. B* **112**, 9795

Zhang Y. G., Liu F., Wang Z. Y., Zhang L. D., (2007), *J. Phys. Chem. C* **111**, 4519

Chapter 5 Oxidation of tungsten nanowire

This chapter concerns studies on the oxidation of tungsten nanowires with an aim to elucidating changes to the structural properties during the oxidation process. Based on experimental results, we carried out simulations to explain the self-limiting oxidation mechanism.

5.1 Background

Metal oxide semiconductors stand out as one of the most versatile classes of materials, due to their diverse properties and functionality. One-dimensional (1D) nanostructures of such materials have attracted increasing attention because of their unique electrical, optical, and chemical sensing properties [Shengelaya 1998, Poizot 2000, review in Liu 2006, Shen 2009] associated with their highly anisotropic geometry and size confinement. They are good candidates for lithium-ion batteries, catalysts, electrochromic devices, and gas sensors [Ponzi 1998, Granquist 1995, Talledo 1995, Micocci 1997, Li 2003, Wang 2003, Kobayashi 2007]. As such, they demonstrate promise for future nanoscale electronic, optoelectronic, and sensing applications.

Among such metal oxides, tungsten oxide 1D nanostructures have been used to construct flat panel displays, optical modulators, gas sensors, humidity/temperature sensors, and so forth [Yao 1992, Arid 1998, Zhao 2000, Cheng 2001, Lee 2000, Santato, 2001, Sayama 2001, Solis 2001, Koltypon 2002, Wang 2003, Kim 2005, Ponzoni 2006, Deb 2007, Gubbala 2007]. Motivated by potential applications, different techniques for the synthesis of 1D tungsten oxide nanostructure have been developed [Li 2003(a), Li 2003(b), Zhu 2003, Zhou 2005, Baek 2007, Song 2007].

One of the simplest and most direct ways to synthesize 1D tungsten oxide nanostructures is through thermal oxidation of tungsten. The oxidation kinetics of the bulk W surface have already been well investigated for over a century [Gulbransen 1960, Webb 1956, Ptushinsku 1967, King 1971]. However limited attention has been paid to the oxidation kinetics in tungsten nanowires although such knowledge is important to achieve precise control of the oxide thickness and microstructure to optimize the performance of tungsten oxide nanowire based devices.

In the present work, oxidation of FEIG tungsten nanowires by direct annealing in an oxygen environment is investigated. The oxidation mechanism and morphology investigation of the tungsten oxide nanowire will be discussed.

5.2 Experimental set up

Tungsten nanowires were initially grown on a home-made silicon nitride membrane TEM die (see Figure 3.8). The method of growth of the FEIG tungsten nanowire has been previously described in Section 3.3.2.

Once the FEIG tungsten nanowire has been grown on the TEM die, the specimen was placed onto an electrically-heated button heater located in a turbo-pumped vacuum chamber with a base pressure of 2×10^{-6} mbar (Figure 5.1). The temperature was measured using a miniature (200 μm) Type-K thermocouple directly contacting the TEM die surface. To ensure accurate temperature measurement of the specimen, good thermal contact between the TEM die surface and thermocouple was achieved through the use of silver paint at the point of contact.

Figure 5.2 illustrates the temperature profile during the oxidation process. After ramping the temperature to the target oxidation temperature of T_1, the temperature was stabilized for about 5 min before introducing oxygen into the chamber. The vacuum pressure was controlled to 2×10^{-4} mbar by adjusting the flow of oxygen through the leak valve. Upon admission of oxygen, due to convective cooling, the specimen temperature drops to T_2, where (T_1-T_2) is about 30-40°C. The specimen temperature was restored to T_1 by increasing the heater current. This temperature compensation process typically took ~60 seconds (from t_1 to t_2). Once the specimen temperature has stabilized at T_1, this signified the time at which we considered oxidation to have started. The oxidation process was stopped at time t_3, by terminating the oxygen supply and turning off the heater. Once the specimen has cooled to room temperature under vacuum, it was taken out from the chamber and mounted into a standard TEM specimen holder for TEM characterization.

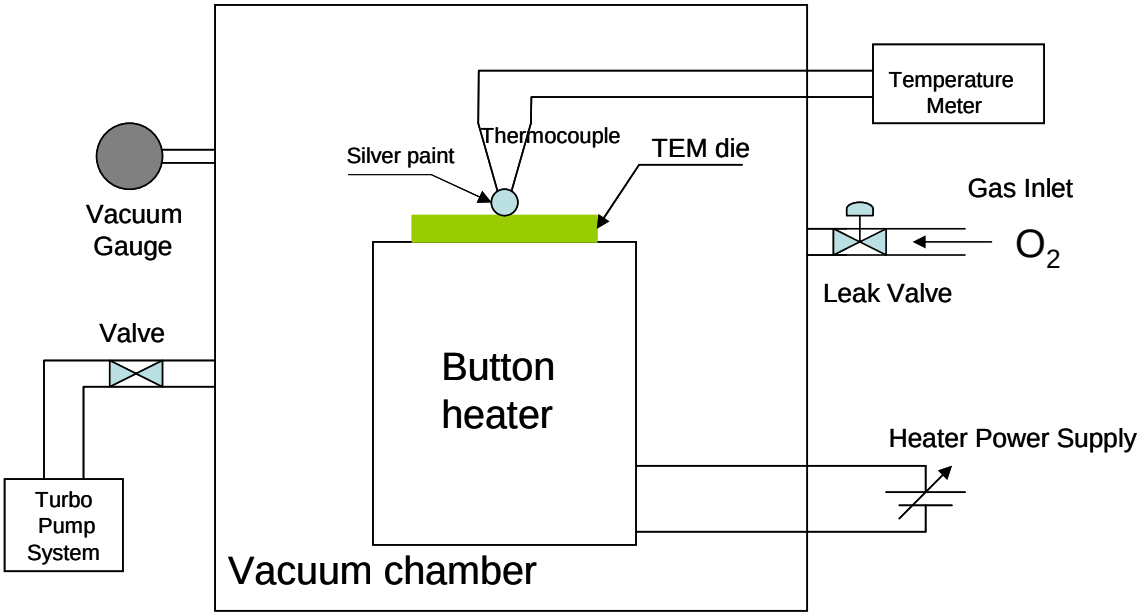

Figure 5.1 Experimental set-up for thermal oxidation of nanowire sample

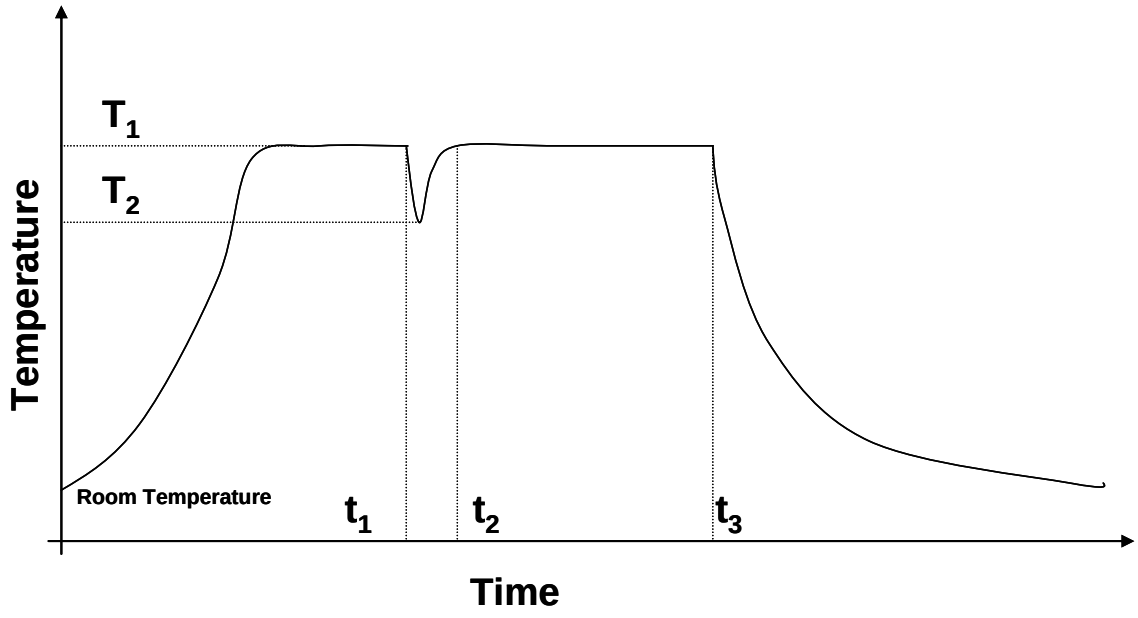

Figure 5.2 A typical temperature profile during oxidation.

5.3 Oxidation of Tungsten Nanowire at 400°C

It is known that tungsten begins to oxidize at a temperature of around 300°C, above which, different forms of tungsten oxide will be progressively formed (from the lowest oxide state (WO) to the highest oxide state (WO_3)) until the temperature

reaches about 700°C [Barth 1961, Granquist 1995]. In the present work, oxidation of tungsten nanowire was first conducted at 400°C.

5.3.1 Design of experiment

Five tungsten nanowires with diameters ranging from 10nm to 28nm were individually oxidized in the vacuum chamber. Prior to oxidation, each tungsten nanowire was imaged by high-resolution TEM (HRTEM, Philips CM300) to determine the diameter of the nanowire. Due to the rough surface of the nanowire, the uniformity of diameter along the wire length is poor. For example, Figure 5.3 shows the morphology of one such nanowire (wire O4) before oxidation. The diameter of one nanowire (Wire O4) can range from 22 nm (d1) to 30 nm (d2). Therefore a mean value is obtained by taking ten random readings along the nanowire. The mean diameter is about 25nm with a standard deviation of about 3.2 nm. Table 5.1 lists the calculated mean diameters of five nanowires alongside the standard deviation σ. Inset image (a) shows the corresponding SAD pattern, which tells us that the initial polycrystalline nanowire contains various nano-sized grains. In Chapter 3, it has already been established that the orientation of the nano-sized crystalline grains is randomly distributed along the nanowire and the mean grain size is proportional to the nanowire diameter. For example, from the dark field image as shown in inset image (b), the mean grain size taken as an average of the diffractive grains is about 15nm.

After oxidation for a period of time, the specimens were taken out for TEM characterization. Table 5.2 lists the sequence in which TEM characterization was carried out for all five nanowires.

Table 5.1 Table of nanowire dimensional parameters

	Wire O1	Wire O2	Wire O3	Wire O4	Wire O5
Diameter $\overline{d}$ (nm)	10	18	22	25	28
Standard deviation $\pm\sigma$ (nm)	1.8	2.0	2.6	3.2	3.4
Maximum/minimum (nm)	8/13	14/23	18/25	21/30	23/36

Table 5.2 Table of TEM characterization sequence for the five nanowires during oxidation

	0.5(hrs)	1(hrs)	2(hrs)	4(hrs)	6(hrs)	8(hrs)	10(hrs)	12(hrs)
Wire O1	√	√	√		√		√	√
Wire O2		√	√	√		√		√
Wire O3	√	√	√		√		√	√
Wire O4		√	√	√		√		√
Wire O5		√	√	√		√		√

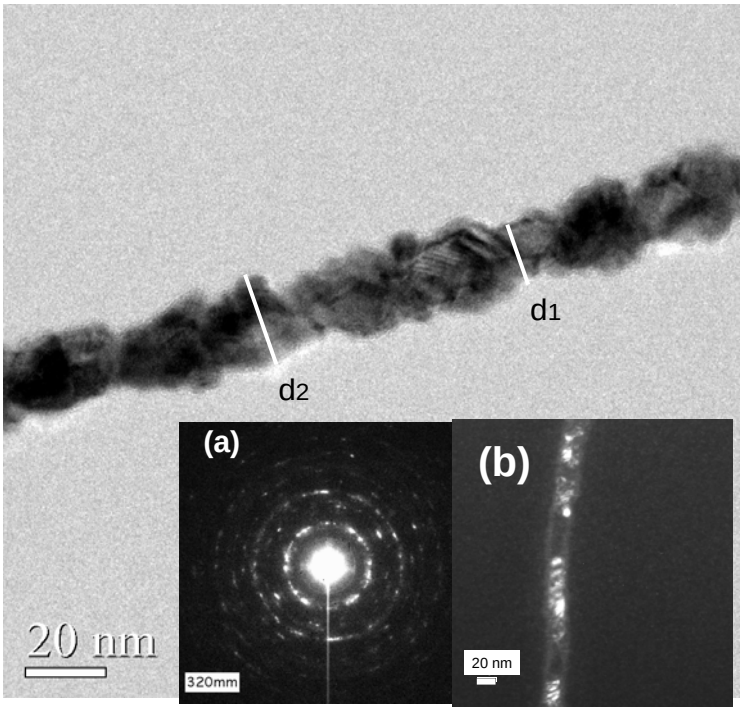

Figure 5.3 Nanowire (Wire 04) with non-uniform diameter, inset image (a) shows a diffraction pattern and (b) shows the dark field image formed in using part of the W(110) diffraction ring.

5.3.2 Progress of Tungsten Oxidation

Figure 5.4 shows a TEM image of Wire O4 after oxidation for 1 hour. Strong diffraction and mass thickness contrast difference are observed in the core-shell nanowire structure, showing the existence of two phases of different atomic weights and degree of crystallinity. Strong diffraction and mass-contrast is observed in the figure, which shows the existence of two phases of different weight and degree of crystallinity in the specimen. It is suggested that the denser phase is tungsten which constitutes the cylindrical core, while the less dense phase is tungsten oxide that encapsulates the core. This can be confirmed by the high-resolution TEM phase-contrast image (Figure 5.5), which corresponds to the interface area A (circled in Figure 5.4) between the core and overcoat shell. In Figure 5.5, the detected lattice spacing of the core is about 0.225nm, which corresponds to the tungsten {110} planes. The overcoat shell layer appears to be amorphous. In order to determine its chemical nature, EDX spectroscopy for selected area B in Figure 5.4 was carried out. The result, shown in Figure 5.6, reveals that the region comprises mainly oxygen and tungsten. From the EDX spectrum, the atomic weight of the detected tungsten to oxygen (W:O) is about 95:5. Compared to the EDX spectrum of the nanowire before oxidation in which the peak of oxygen signal can not be identified, the additional oxygen content in oxidized nanowire is believed to come from reacted tungsten oxide in the overcoat shell region.

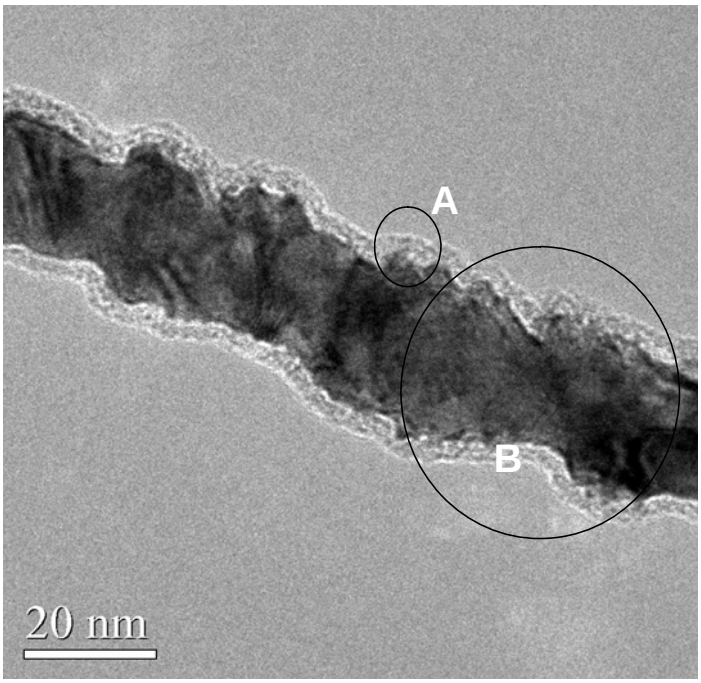

Figure 5.4 Wire O4 after oxidation for 1hour.

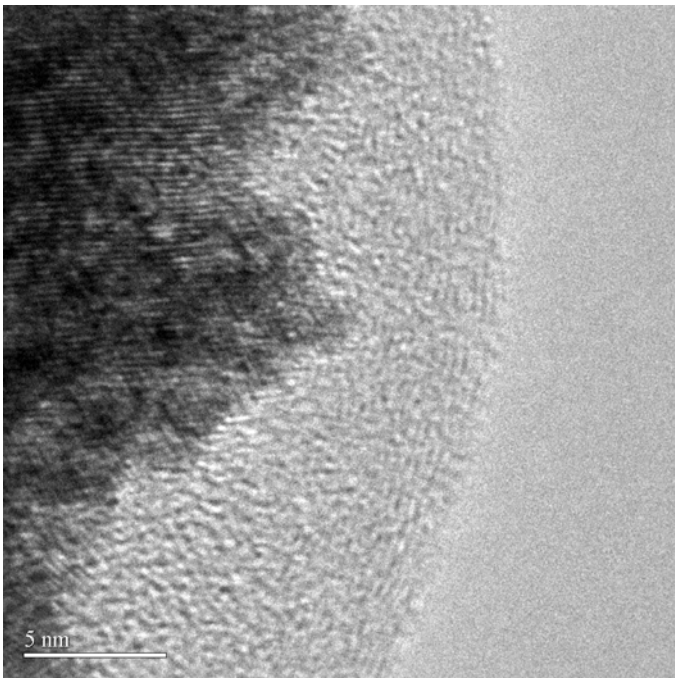

Figure 5.5 HRTEM image of selected area A in Wire O4

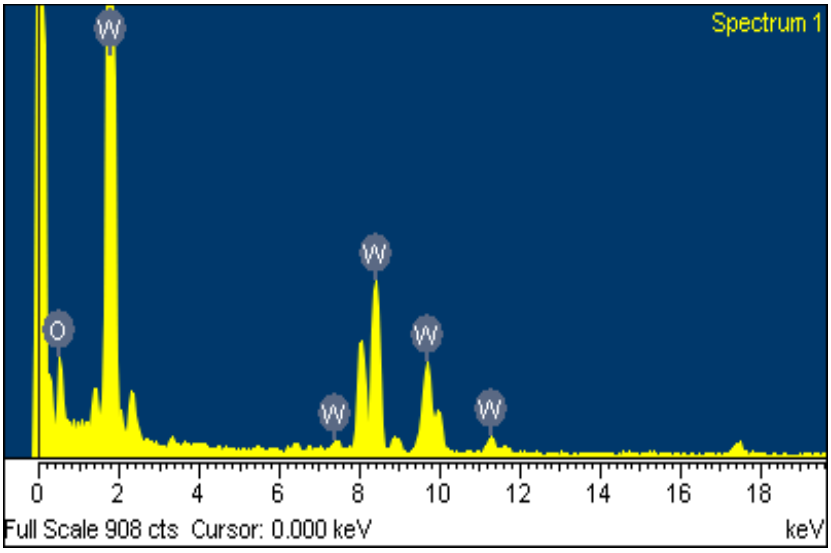

Figure 5.6 EDX spectrum for selected area B in Wire O4

To monitor the progress of oxidation, the diameter of the tungsten core and thickness of oxide shell were measured after various oxidation times. Figure 5.7 is a TEM image of Wire O4 after 4 hours of oxidation, clearly showing that with the increase in oxidation time, the average diameter of the tungsten core has reduced to ~14nm while the oxide layer thickness has expanded to ~15nm. Finally after 12 hours of oxidation, the tungsten core has reduced to ~4 nm in diameter while the oxide thickness is ~ 23 nm (Figure 5.8).

It is observed, firstly, that the oxide layer becomes increasingly non-uniform with oxidation time, which could be caused by the difference in oxidation rates for different tungsten crystallographic orientations along the polycrystalline nanowire [Mitrofanov 1963], and exacerbated by the volume expansion of the oxide. In addition, oxidation preferentially occurs at the boundaries and defects [Kolmakov 2003], which could give rise to non-conformal oxidation along the nanowire.

On the other hand, the tungsten core became increasingly uniform in diameter, and appears smooth after 12 hours of oxidation. This phenomenon can be attributed to the effect of compressive stress in the oxide. In general, compressive stress arises

in a growing oxide when its molar volume exceeds that of the material being oxidized [Stringer 1970]. In the case of tungsten oxide, the volume of a WO_3 molecule is 32.37 $Å^3$, which is larger than the volume of a tungsten atom of 9.53$Å^3$. Thus a large increase in molar volume accompanies the conversion of W to WO_3. During the oxidation of the tungsten, the oxygen diffuses through the previously-formed oxide layer and reacts with the tungsten atom at the tungsten/oxide interface. The newly-formed oxide has to push out the previously-formed oxide more to accommodate the volume expansion. This results in compressive stress accumulating at the tungsten-oxide interface, which will limit the oxygen-tungsten reaction rate and the diffusion rate of oxidants to the interface [Hsueh 1983, Kao 1985]. As a consequence, the rate of reduction of the core diameter becomes progressively smaller and finally the core approaches an asymptotically uniform diameter as shown in Figure 5.8. This retarded oxidation phenomenon is termed as self-limiting (or "stress-limited") oxidation which has been widely studied in Si nanowires [Liu 1993, Liu 1994, Heidemeyer 2000]. It has also been observed in the oxidation of metal nanowires of tin [Kolmakov 2003] and bismuth [Li 2006], as well as in nanodot structures [Scheer 2003, Chen 2005]. However, to the best of our knowledge, the self-limiting oxidation of tungsten nanowire has not been observed nor studied previously.

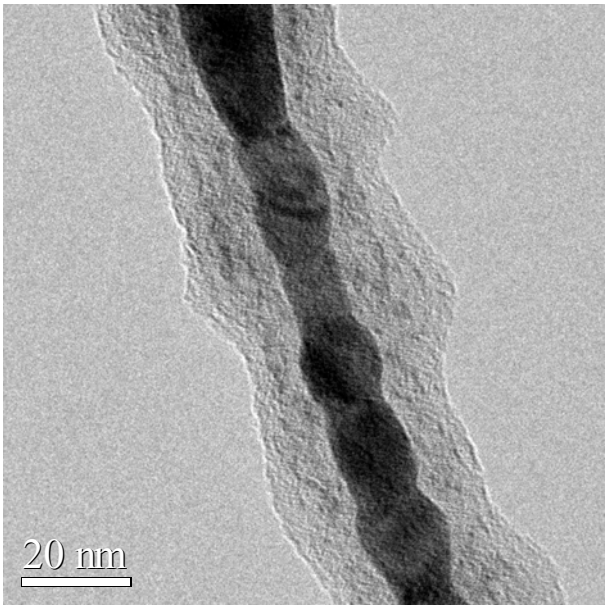

Figure 5.7 Wire O4 after oxidation for 4 hours

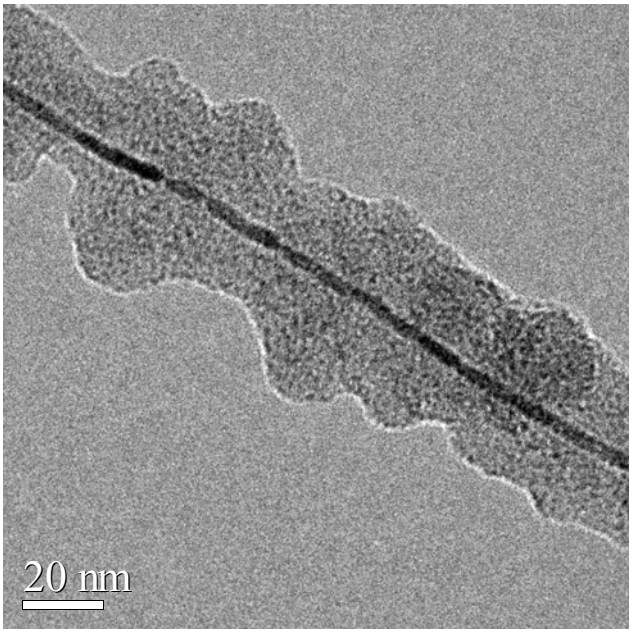

Figure 5.8 Wire O4 after oxidation for 12 hours

The thickness of oxide shell and remaining diameter of the tungsten core as a function of oxidation time for different nanowires (Wire O1 – Wire O5) are plotted as shown in Figure 5.9 and Figure 5.10, respectively. For oxidation beyond ~6 hours, the oxide growth rate and the shrinkage rate of the core progressively diminishes with time. After oxidation for about 12 hours, both thickness of oxide shell and diameter

of tungsten core appear to approach asymptotic values, as would be expected if the oxidation in tungsten nanowire is self-limited by oxidation-induced stress.

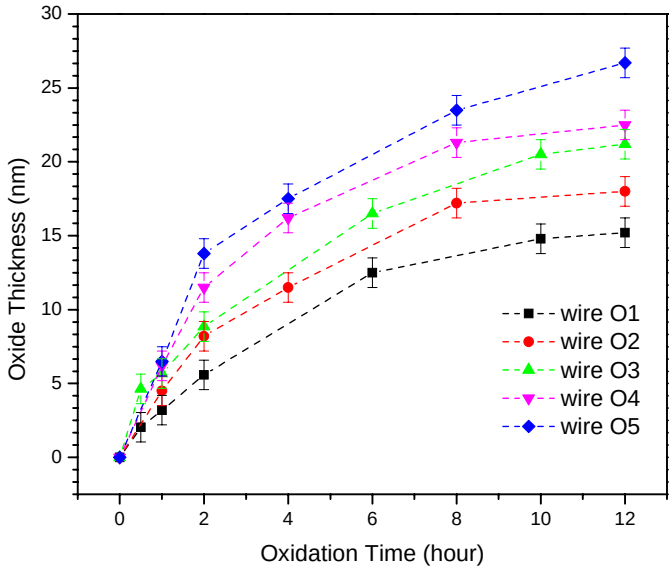

Figure 5.9 Thickness of oxide shell vs. oxidation time

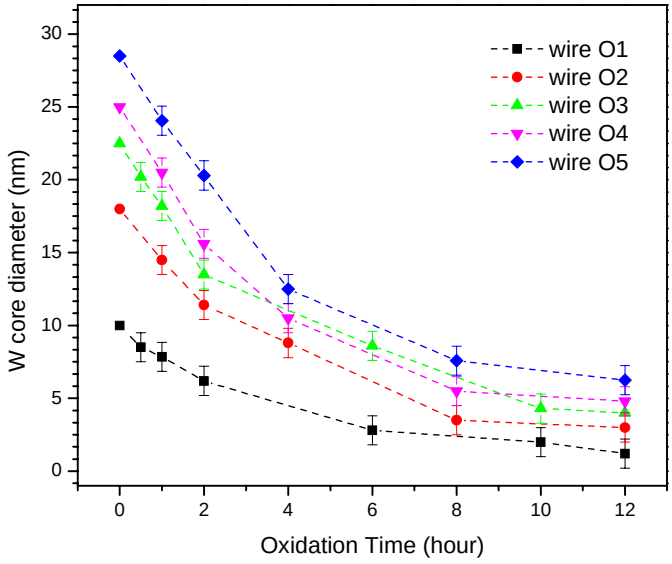

Figure 5.10 Diameter of tungsten core vs. oxidation time

5.3.3 Self-limiting oxidation

At the outset, we need to determine whether the self-limiting oxidation is kinetically limited or thermodynamically limited. Assuming self-limiting oxidation will reach a constrained equilibrium state, although a residual tungsten core cannot be the lowest energy state since the oxidation reaction is highly exothermic, a deep metastable state of constrained equilibrium may, in principle, occur if a large energy barrier exists in the pathway to equilibrium. To assess the likelihood of this metastable state, the incremental energy cost arising from stress built up in the oxide and the formation energy of WO_3 from W is compared. A simple elastic model yields an upper bound for the strain energy per unit column length, $\pi Y\delta^2 / 2(1-\nu)$, where Y and ν are the Young's modulus and the Poisson's ratio of the oxide, respectively, and δ is the radial expansion at the W/WO_3 interface due to the additional oxide growth. From this estimation, taking Y as about $\sim 30\times10^{10}$ Pa [Parreira 2006, Polcar 2007] and ν as 0.2 from oxide bulk values [Dunn 1995], the upper bound of energy cost per oxide molecule grown for a tungsten core diameter of 2nm and 5nm is estimated to be in the order 0.4eV and 0.1eV, respectively, which is much smaller than the 9eV energy gained for each oxide molecule created due to the chemical reaction. Therefore a constrained equilibrium state should be ruled out. It can be concluded that oxidation of W wire is kinetically limited and the asymptotic behavior arises from accumulated interfacial stress.

To explain oxidation process in a Si cylindrical structure under interfacial stress, Kao *et al.* [Kao 1987, 1988] proposed a model where the effects of mechanical stress on the reduction of oxidation rate at the Si/SiO_2 interface are taken into account. In this work, Kao's model [Kao 1987] is applied to explain the self-limiting oxidation mechanism in tungsten nanowires which can be described as follows.

According to Deal-Grove model [Deal 1965], with appropriate boundary conditions in cylindrical coordinates, the oxidation rate (dx_0/dt) can be expressed as:

$$N\frac{dx_0}{dt} = \frac{C^*}{\frac{1}{K_s} + \frac{1}{h}\frac{a}{b} + \frac{1}{D}a\log\frac{b}{a}} \qquad (5.1)$$

where K_s is the surface reaction coefficient, D is the oxidant diffusivity in oxide, C^*, is the oxidant solubility in the oxide, N is the oxide density, h is the surface mass transfer constant of oxidant ($1/h << 1/K_s$, and can be neglected [Liy), and a and b are the radius of curvature of the tungsten core surface and the radius of oxide shell surface, respectively (Figure 5.11(a)). Both a and b change with oxidation time.

The formation of new oxide at the tungsten surface involves a volume expansion. The newly-formed oxide expands and pushes out the old oxide, which rearranges itself through viscous flow. Because of the high viscosity (η) of the oxide, the viscous oxide deformation involves large stresses [EerNisse 1979], which can be resolved into $\sigma_\perp$, the stress normal to the tungsten/tungsten oxide interface, and P, the hydrostatic pressure throughout the bulk of oxide (as shown in Figure 5.11(a)). The stress components in a convex cylindrical structure are shown schematically in Figure 5.11(b) [Kao 1988]. $\sigma_\perp$ is compressive and can be expressed as:

$$\sigma_\perp = -2\eta\xi\left(\frac{1}{a^2} - \frac{1}{b^2}\right) \qquad (5.2)$$

while P is tensile and can be expressed as:

$$P = -2\eta\xi\frac{1}{b^2} \qquad (5.3)$$

where ξ is a velocity constant determined from the oxide growth rate at the interface.

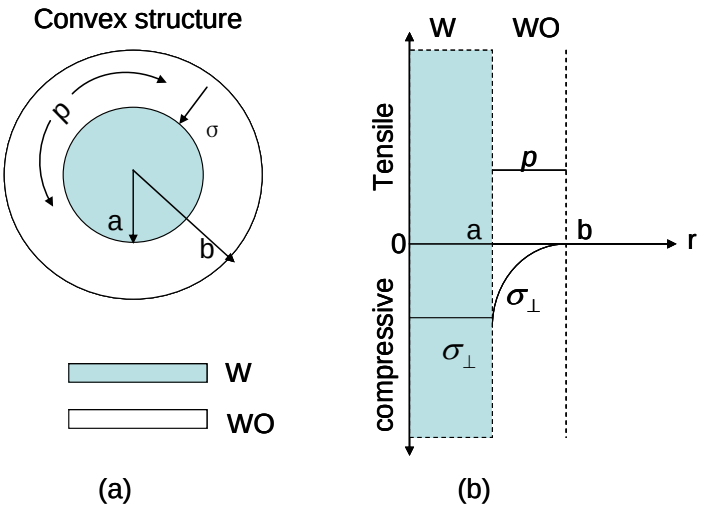

Figure 5.11 Stress components in a convex tungsten oxide nanowire structure during oxidation

The stress-dependent parameters in Equation 5.1 are surface reaction rate K_s, oxidant diffusivity D and oxidant solubility C^*. As suggested by Sutardja and Oldham [Sutardja1989], C^* in silicon oxidation is almost stress-independent if the oxidation temperature is low (<800°C). Hence, C^* can be considered to be a constant. In the present study, since both the oxidant concentration and oxidizing temperature are low we also assume the oxygen solubility C^* in amorphous tungsten oxide to be a stress-independent constant parameter. It was suggested by Kao *et al*. [Kao 1988] and Umimoto *et al.* [Umimoto 1989] that the viscosity of oxide is a function of the temperature T and hydrostatic pressure P. Sutardja and Oldham modified it by considering the viscosity as a shear-stress dependent parameter [Sutardja 1989]. Sutardja's model predicted that the viscosity is almost constant over a large range of the shear stress and falls beyond a certain critical high shear stress. Since the shear stress decreases with an increase in oxide thickness, in the present experiment, the viscosity η is assumed to remain constant at 400 °C.

Therefore, in our present model K_s and D are considered as the stress-dependent parameters in tungsten oxide. Both of them have an Arrhenius relationship with stress barriers as:

$$K_s = K_0 \exp\left(\frac{\sigma_\perp V_k}{k_B T}\right) \tag{5.4}$$

and

$$D = D_0 \exp\left(-\frac{pV_D}{k_B T}\right) \tag{5.5}$$

where K_0 is the reaction rate constant in the case of stress-free, k_B is Boltzmann's constant, D_0 is the oxidant diffusivity under zero stress, V_k is the volume changes corresponding to a unit chemical oxidation reaction, V_d is the activation volume of diffusivity.

To understand the stress contribution to the retardation of the oxidation rate, two kinds of the self-limiting oxidation are studied, namely 1) reaction-limited oxidation where oxidation is retarded only by the effect of stress on the interface reaction, (p =0) and 2) diffusion-limited oxidation where oxidation is influenced only by the hydrostatic pressure in oxide ($\sigma_\perp = 0$). To simulate the self-limiting oxidation of the tungsten nanowire structure at 400°C, the initial conditions are established as follows:

(i) The initial value of geometric parameters a, b and ξ are determined from TEM measurements.

(ii) For reaction-limited oxidation, it is assumed that p=0 and D=D_0 while for diffusion-limited oxidation, the normal stress $\sigma_\perp$ is ignored ($\sigma_\perp$=0) and K= K_0. D_0 and K_0 are stress-free constants (see table 5.3).

(iii) In silicon oxidation [Sutardja 1989], V_k and V_d are considered as constant parameters during oxidation. In this work, the V_k and V_d are determined by curve fitting to the first experimental data point of each nanowire under reaction-limited and diffusion-limited oxidation conditions, respectively. (see Figure 5.12 and

Figure 5.13) The values obtained for V_k and V_d are then used to calculate K_s and D, respectively, for this nanowire at other times according to Equations (5.4) and (5.5). $\sigma_\perp$ and p are calculated through Equations (5.2) and (5.3).

(iv) The oxide thickness under reaction-limited and diffusion-limited oxidation conditions are calculated using Equation (5.1) , with the reference values for tungsten oxide, C^*, N and η as listed in Table 5.3. Finally the calculation results are shown in Figure 5.12 and 5.13.

Table 5.3 Reference values used in simulation

C^*	N	η	D_0	K_0
7.5×10^{-5} (molecules/nm^3) [Battery 196]	16.5 (molecules/nm^3) [Gerand 1981]	2.5 (centistokes) [Bailey 1996]	1.3 (cm^2/s) [Stringer 1963]	0.5 (Å/s) [Gulbransen 1949]

For reaction-limited oxidation (Figure 5.12), the simulated oxide thicknesses are lower than the experimental values. This means that in the absence of any influence from hydrostatic pressure in the oxide, the oxidation process would be more retarded due to the accumulating normal stress, $\sigma_\perp$, at the tungsten/oxide interface, which reduces the reaction rate, K_s, by making the oxidation reaction less energetically favorable. The difference in oxide thickness between simulation and experiment is greater for a thicker nanowire, which could be attributed to the higher normal stress accumulated in the thicker nanowire. Figure 5.12 indicates a trend where the normal compressive stress at the tungsten/oxide interface retards tungsten oxidation.

On the other hand, a comparison of the simulation results under diffusion-limited conditions with the experimental values shows that the oxidation process is faster in the absence of any influence from normal compressive stress at the tungsten/oxide

interface (Figure 5.13). This is because in a convex nanowire structure, the hydrostatic pressure p is tensile throughout the oxide (Figure 5. 11(b)). As tensile pressure would enhance the volume of the voids in the oxide network that are occupied by the diffusing oxidant species [Kao 1985], the oxidation rate increases.

Combining the above results, it can be adduced that the oxidation is neither fully reaction-rate limited, nor fully diffusion-rate limited. Both the normal compressive stress $\sigma_{\perp}$ at the tungsten/oxide interface and tensile hydrostatic pressure p in the oxide play a role in the oxidation, in which the former retards the oxidation reaction rate while the latter enhances oxidant diffusion in the oxide. These two opposing stress influences give rise to oxidation trend observed (Figure 5.9 and Figure 5.10).

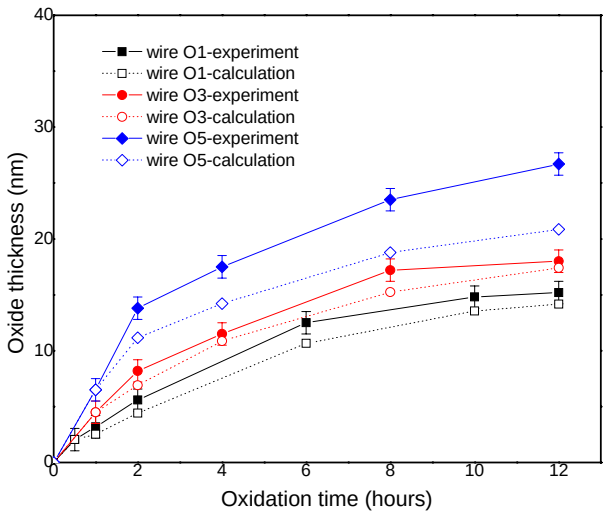

Figure 5.12 Simulated oxide thickness assuming reaction-limited oxidation compared with experimental data.

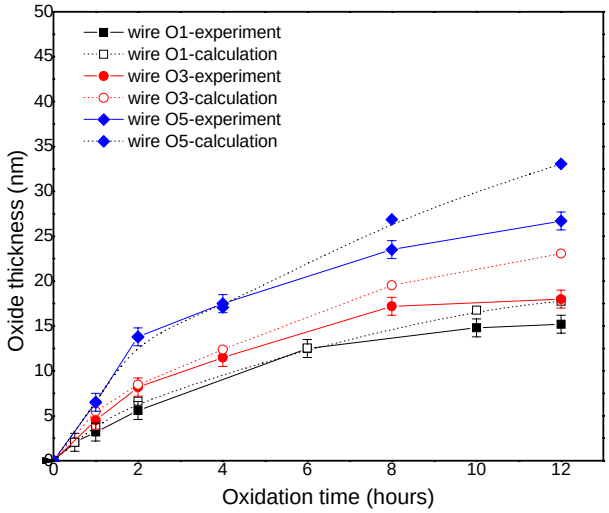

Figure 5.13 Simulated oxide thickness assuming diffusion-limited oxidation compared with experimental data.

5.4 Tungsten Oxidation at higher temperature (450-500°C)

In the above section, oxidation at 400°C gave rise to tungsten oxide which is amorphous. However, at higher oxidation temperatures, we found that the tungsten oxide layer becomes crystalline.

As shown in Figure 5.14, the tungsten nanowire oxidized in 450°C for 4 hours is seen to contain some crystalline grains embedded in amorphous tungsten oxide. The amount of crystalline material is found to increase with oxidation time. Figure 5.15(a) shows fully-crystalline tungsten oxide in the shell after oxidation at about 500°C for 8 hours. The magnified HRTEM image (Figure 5.14(b)) reveals that the lattice spacing is ~ 0.378nm, which can be assigned to the lattice spacing between the (010) planes of monoclinic $W_{18}O_{49}$ crystal along the intertexture (JCPDS card: 36-0101) [Frey 2001, Li 2003]. This monoclinic crystalline form is related to the γ phase [Berger 1956]. The composition is consistent with an EDX measurement which shows an oxygen-to-tungsten ratio of ~2.71. Compared to the other bulk highly-crystalline γ phase

tungsten oxide (like $W_{18}O_{49}$) achieved by directly heating a hot substrate (such as tungsten foil or film) at about 1000°C [Liu 2003, Choe 2004], the oxidation of a tungsten nanowire requires a much lower temperature of about 500°C. This is probably due the large surface-to-volume ratio of a 1D nanostructure that allows a relatively large amount of oxidant to be absorbed. This increase in oxidation efficiency can also be found in $W_{18}O_{49}$ nanorods formed in a relatively low temperature range of 600-700°C by thermal annealing a W_2N film [Seongho 2007].

Aside from the higher degree of crystallinity, it is also known that higher temperature oxidation results in a higher oxide crystalline structure [Berger 1956]. It is expected that the higher crystalline oxides, such as β-phase ($WO_{2.9}$) or α-phase WO_3 could be formed if oxidation is carried out at above 500°C. However we did not perform systematic experiments for two reasons:

(i) Tungsten oxide will start to volatilize, especially for a nanowire structure due to extremely high surface to volume ratio. For example, Gilleta *et al*. showed that the WO_3 nanorods could be sublimated at relatively low temperature (550°C) [Gilleta 2005]. We also found that the oxide thickness started to reduce after oxidation for 6 hours at 500°C even as the tungsten core was still shrinking, indicating that sublimation had indeed been taking place.

(ii) It has been found that the present polycrystalline tungsten nanowire core starts to crystallize at a temperature of around 500-600°C under an oxygen pressure of 2×10^{-4} mbar (Chapter 4). The morphology of the crystallized tungsten nanowire becomes unstable and finally leads to a break up.

For these reasons, oxidation at temperatures higher than 600°C was not carried out.

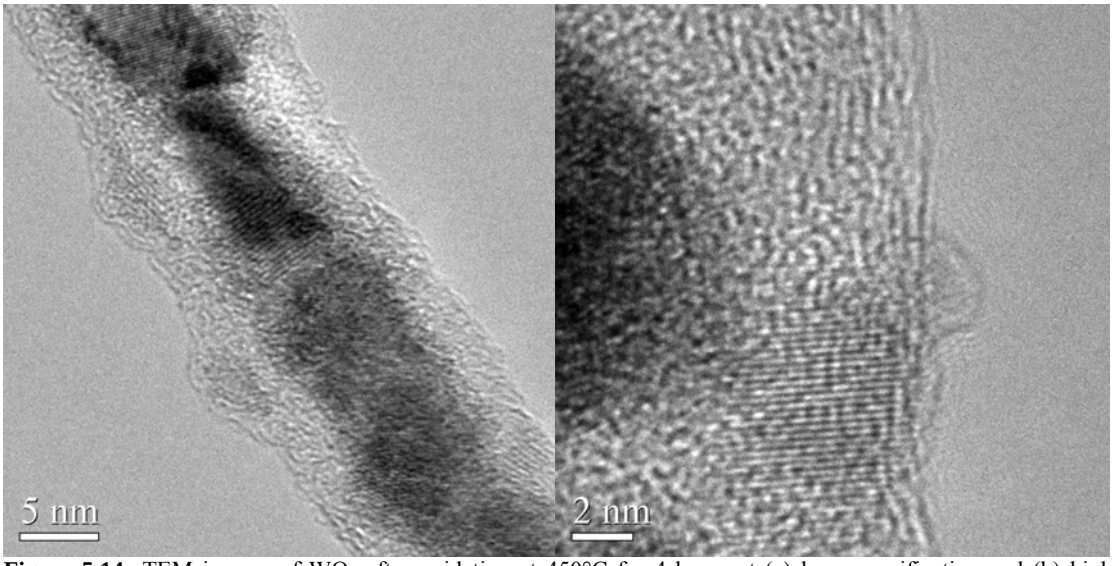

Figure 5.14 TEM images of WO_3 after oxidation at 450°C for 4 hours at (a) low magnification and (b) high magnification.

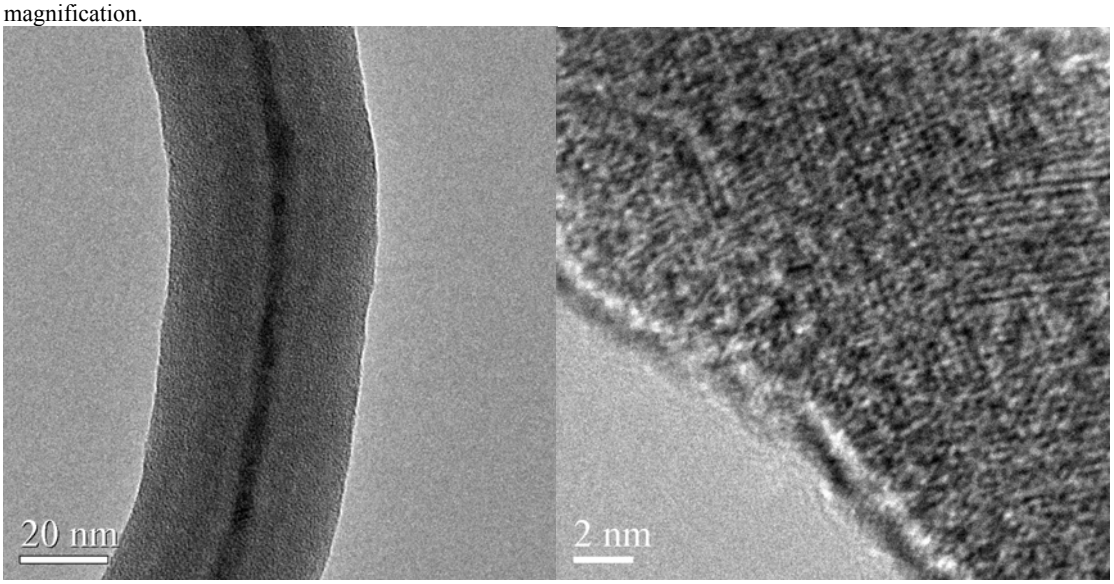

Figure 5.15 TEM images of WO_3 after oxidation at 500°C for 8 hours at (a) low magnification and (b) high magnification.

5.5 Summary

In this chapter, the polycrystalline tungsten nanowires were thermally oxidized in an oxygen environment. At temperature of 400 °C, the formed oxide was found to be amorphous structure. It was also found that oxidation is kinetically limited which results in a tungsten/amorphous tungsten oxide core-shell structure. Simulations carried out in reaction-limited and diffusion-limited oxidation conditions show that the asymptotic behavior in oxidation arises from accumulated compressive normal

stress at the tungsten/tungsten oxide interface. The crystalline oxide structures were formed at temperature of above 400 °C.

References

Bailey J. A., Budd K. D., Tran T. T., (1996) *U. S. Patent* 5772978

Barth V. D. and Rengstorff G. W. P., (1961), *DMIC Report* 155.

Battery J.B. and Stickney R.E., (1969), *J. Chem. Phys.* **51**(10), 4475.

Berger I. I, Sevast yanov N. G., Putilina L. K., (1956), *Russian Journal of Inorganic Chemistry* **1**(8), 1713.

Chen C. H., Yamaguchi T., Sugawara K.I., Koga K., (2005), *J. Phys. Chem. Lett. B* 109, 20669.

Choe M. H., Park S. A., Yang K. D., *et al.*, (2004),*J. Vac. Sci. Technol. B* **22**(3), 1084.

Deal B. E., Grove A. S., (1965), *J. Appl. Phys*. **36**, 3770.

Dunn M. L., Ledbetter H., (1995), *Journal of Materials Research* **10**(11), 2715-2722

EerNisse E. P., (1979), *Appl. Phy. Lett.* **35**, 8,

Frey G. L., Rothschild A., Sloan J., *et al.*, (2001), *Journal of Solid State Chemistry* **162**(2), 300.

Gerand B., Nowogrocki G., Figlarz M., (1981), *Journal of Solid State Chemistry* **38**, 312.

Gilleta M., Delamare R., Gillet E., (2005), *Eur. Phys. J. D*, **34**, 291.

Granquist C. G., (1995), "*Handbook of Inorganic Electrochromic Materials"* ed: Elsevier Science, Amsterdam

Gulbransen E. A. , *Ind. Eng. Chem.*, (1949) **41** (7), 1385.

Heidemeyer H., Single C., Zhou F., Prins F. E., Kern D. P., and Plies E., (2000), *J. Appl. Phys.* **87**, 4580.

Hsueh C. H., and Evans A. G., (1983), *J. Appl. Phys.* **54**(11) 6672.

Kao D. B., McVittie J. P., Nix W. D., and Saraswat K. C., (1985), *IEEE, IEDM* **85**, 388.

Kao D. B., McVittie J. P., Nix W. D., and Saraswat K. C., (1987), *IEEE Trans. Electron Devices* **34**, 1008.

Kao D. B., McVittie J. P. , Nix W. M., (1988), *IEEE Trans. Electron Devices* **35**(1), 25.

Kolmakov A., Zhang Y., Moskovits M., (2003), *Nano Lett.* **3**, 1125.

Lepage J., Mezin A. and Nivoit M., (1985), *Surface Science* **161**, 255.

Li L., Yang Y. W., Li G. H., Zhang L. D., (2006), *small* **2**(4) 548.

LiX. L., Liu J. F., Li Y. D., (2003), *Inorg. Chem.* **42**, 921.

Liu H. I., Biegelsen D. K., Johnson N. M. *et al.*, (1993), *J. Vac. Sci. B* **11**, 2532.

Liu H. I., Biegelsen D. K., Ponce F. A. *et al.*, (1994), *Appl. Phys. Lett.*, **64**, 1383.

Liu Z., Bando Y., Tang C., (2003), *Chem. Phys. Lett.* **372**, 179.

Mitrofanov O.V., (1963), *Soviet Physics-Crystallography* (Trans), **8**(2), 229-231.

Miyake K., Kaneko H., Sano M., *et al*., (1983), *J. Appl. Phys.* **55**(7), 2747.

Parreira N. M. G., Carvalho N. J. M., Cavaleiro A., (2006), *Thin Soild Film* **510**, 191.

Polcar T., Parreira N. M. G., Cavaleiro A., (2007), *Vacuum* **81**, 1426.

Scheer K. C., Rao R. A., Muralidhar R., *et al.*, (2003), *J. Appl. Phys.* **93**(9) 5637.

Scherer G. W., (1986), "*Relaxation in Glass and Composite"* ed: Wiley, New York

Senogho J., Yong K. J., (2007), *Nanotechnology* **18**, 245602.

Stringer J., and Rosenfield A. R., (1963) *Nature*, **199**, 337.

Stringer J., (1970), *Corros. Sci.* **10**, 513.

Sutardja P. , Oldham W. G. , (1989), *IEEE Trans. Electron Devices* **36**(11), 2415.

Umimoto H., Odanak S., Nakao I. and Esaki H., (1989), *IEEE Trans. Computer-Aided Design Intergr. Circuits Syst.,* **8**(6) 599.

Chapter 6 Conclusion

6.1 Summary

In this work, we have fabricated tungsten nanowires by the field emission induced growth method. We demonstrated the growth of a single nanowire on a flat substrate by initiating growth via arc discharge to the substrate while incurring minimum damage. Through the use of a nanomanipulator, we are able to initiate growth on the desired location, allowing the technique to create nanowires' interconnects.

By growing the nanowire on a silicon die that could be mounted in a TEM holder, its morphology and structural properties were studied by TEM techniques. It is shown that the specimens are mainly polycrystalline BCC tungsten structure comprising irregularly shaped grains. The mean grain size was found to range from 7 nm to 40 nm with the increase of nanowire diameter from 10 nm to 50nm. The increase in mean grain size may be due to local heating of the nanowire tip end by W^+ ion bombardment during growth, which provides energy needed for grain coarsening.

Four point measurements conducted on nanowires grown on metal electrodes and contacted by FIB deposition of Pt material shows the resistivity of as-grown tungsten nanowire (in diameter of 10nm and length of 7.6 μm) is about 160 μΩ·cm, which is about 18 times that of bulk tungsten. The larger resistivity is believed to be due to enhanced electron scattering at the surface and at grain boundaries within the nanowire.

It was observed that the resistivity of nanowires increase with diameter decreasing. By comparing the results from experiments and simulations of combined FS and MS model, it is found that the electron scattering caused by the boundary of nanowires grains is the main contribution to the increase in resistivity.

The polycrystalline tungsten nanowires were annealed in vacuum. The annealing process was studied via either *ex situ* or *in situ* TEM observations. Nanosized grain growth is driven by the excess free energy from the grain boundaries. The grain growth rate was determined from the changes of the mean grain size during the annealing process. The calculated activation energy of grain boundary mobility E_a is about 187 kJ/mol.

Once the grain grows to straddle the nanowire diameter, a bamboo-like nanowire structure is formed which consists of only individual columnar shaped grains along entire length of the nanowire. It is shown that the rate of transformation to bamboo-like nanowire structure is faster in the nanowires of smaller diameter. The transformation rate is found to be in agreement with Walton's theory which was developed for microscale structures. We also introduced a grain grooving temperature T_{GB}, at which temperature 90% of nanowire takes on a bamboo-like structure. Above this temperature, it is considered that the grain growth process is replaced by a grain grooving process.

The formation of the grain groove can be attributed to the tendency of a vertical grain boundary to shrink in order to reduce its area and the free energy so that the grains become pinched-off and spheroidized. The analysis of the shallow grain groove at the beginning of the grain grooving process provides us with a method to calculate the diffusion coefficient D_s at the nanowire surface.

We have studied the evolution of grain grooving with the annealing process until the nanowire eventually breaks up at a grooved boundary site. It was found that a critical value of aspect ratio of grain length to diameter, $(L/D)_{crit}$, exists in every columnar grain, above which the grain will break up from its neighbor. Our observation in tungsten nanowire showed that $(L/D)_{crit}$ is about 3, which is in good

agreement with a theoretical prediction by Klinger's model.

Due to this break-up problem, it is found that a free-standing tungsten nanowire of 40 nm in diameter and 10 μm in length is morphologically unstable at elevated temperature resulting from Joule-heating. This can be successfully prevented by overcoating the tungsten core with a carbonaceous layer. It was found that with a carbonaceous shell layer, the nanowire can sustain much higher current densities of up to 3 x 10^7 A/cm^2 compared to 1x10^6 A/cm^2 for a bare tungsten nanowire. The result suggests that the W/C core-shell nanowire has great potential to be used as free-standing interconnects in future nanoelectronic devices. In addition, in our preliminary *in situ* TEM studies, we also observed a phenomenon where individual grains rotate around the nanowire axis during the evolution of grain groove.

Amorphous tungsten oxide nanowires were obtained through thermal oxidation of the tungsten nanowire at a temperature of about 400°C in an oxygen environment. It was found that oxidation is self-limited by accumulated stress in the oxide, which results in a W/α-WO_3 core-shell structure. Non-uniformity of the oxide shell may be due to anisotropy in the oxidation rate of different crystal planes. The uniformity of the tungsten core after a period of oxidation may be attributed to the retardation of the oxidation rate. Our simulations based on the Kao's model show that self-limiting oxidation is mainly due to reduction of the oxidation rate by the normal compressive stress at the tungsten/oxide interface, which overwhelms the diffusion of the oxidant from tensile hydrostatic pressure through the oxide.

If the nanowire is oxidized at a higher temperature of 450°C, the resulting oxide shell has a crystalline. The magnified HRTEM image shows that the lattice spacing of crystalline oxide is about 0.378nm, which can be assigned to the lattice spacing between the (010) planes of monoclinic $W_{18}O_{49}$ crystal along the intertexture.

6.2 Future work

We have studied the electrical size effect due to the surface and boundary confinement of polycrystalline tungsten nanowire at room temperature. Electrical characterization at cryogenic temperatures may help us to better understand the conduction mechanisms involved in the nanowire.

From *in situ* TEM experiments, we observed that individual grain rotation along the nanowire axis during the grain grooving developing process. More careful TEM characterization is required to better understand the grain rotation mechanism. Since the grain rotation is strongly dependent on the grain surface and boundary condition, it is of interest to find out the rotation relationship between different parameters such as rotation rate, grain boundary energy, surface diffusion coefficient and the crystalline plane of the grain.

Tungsten oxide is a widely used gas sensing material. One of the potential applications of our oxidized tungsten nanowires is use in a gas sensor device. Preliminary works have provided us its structural information. Further study should include systematic characterization of its gas sensing property.

APPENDIX A - Publications

1). J. T. L Thong, C.H. Oon, G. F. You, K.S. Yeong, (2002), "Connection of nanostructures using nanowires grown by a self-field-emission process" *Proceeding of SPIE*, **4936**, 26.

2). G. F. You, H. Gong, J. T. L. Thong, (2010) "Improving the morphological stability of a polycrystalline tungsten nanowire with a carbon shell" *Nanotechnology* 21(19), 195701.

APPENDIX B - Simulation of temperature profile of nanowire

Firstly, an ideal situation is considered for a free-standing tungsten nanowire of a uniform radius R, constant electrical resistivity ρ and thermal conductivity κ, and where the nanowire straddles across a gap of L_w (Figure B.1).

Taken ρ is a constant of 30 μΩ·cm at room temperature for tungsten nanowires of 40nm diameter. The thermal conductivity κ can be derived from the Wiedemann-Franz Law $\kappa = LT/\rho$ to be about 20W/m·K, where L is the Lorenz constant, 3.02×10^{-8} WΩ/K^2 for tungsten at T=300K [Halas, 1998]. By using equation as in chapter 4(Equation 4.7)

$$-\kappa \frac{dT}{dx} = \frac{\rho x I^2}{S^2}, \qquad \text{(B.1)}$$

the simulated temperature profile along a nanowire (L_w = 10μm) passing 22μA current is plotted in Figure B.2. A maximum temperature of ~950K is reached in the middle of the nanowire (x = 0) by assuming the temperature at both edges to be 300K ($x = \pm 5$ μm).

However, the exact temperature profile along the tungsten nanowire is more complex, as it is also affected by other factors (such as the temperature dependence of ρ and κ, and non-uniformity in the nanowire diameter). To testify the accuracy of our simulation profile, one simple way is to find a reference temperature which can be measured directly at a particular point along nanowire and then compare it to the simulated temperature at that point. However, direct measurement using a classical pyrometer cannot be applied to nanowires.

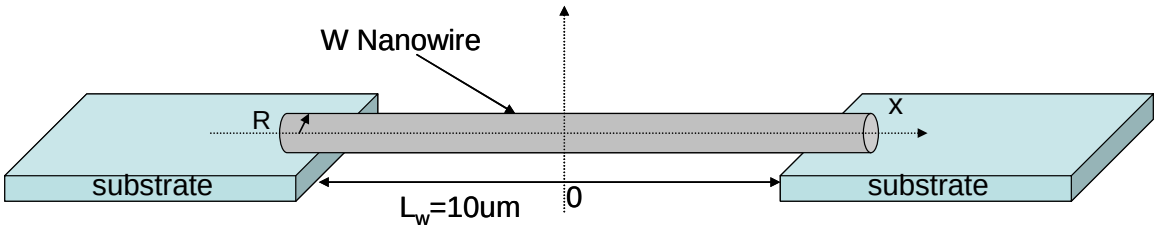

Figure B.1 Schematic of a free-standing nanowire.

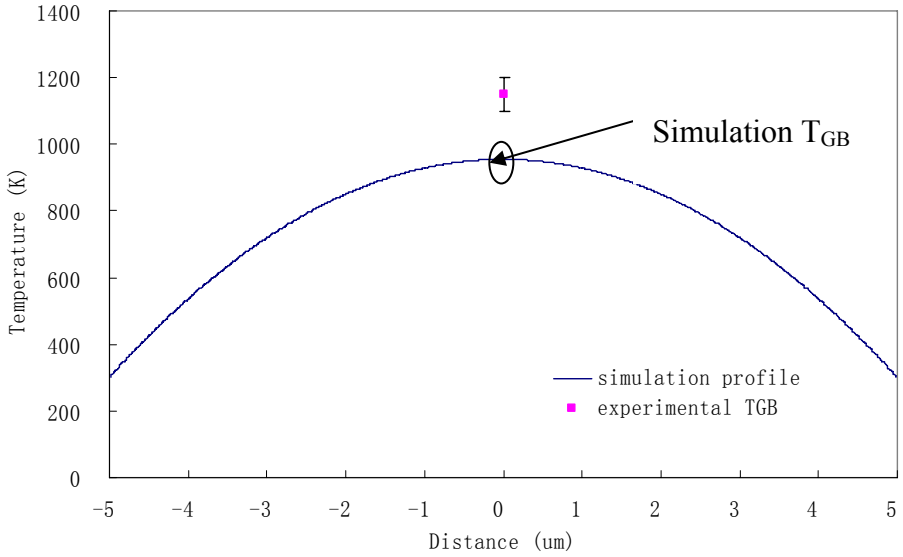

Figure B.2 Simulated temperature profile compared with measured T_{GB}

B.1 Temperature calibration: Determination of reference temperature (T_{GB})

Fortunately, we have observed that FEIG tungsten nanowires transform to bamboo-like structure above a specific annealing temperature, which is defined as grain grooving temperature (T_{GB}) in this project. Based on this, the temperature difference between the simulation and experiment can be obtained as following:

1) First, the nanowire is annealed by ramping up the Joule-heating current *in situ* in the TEM (Method 3). The current is noted at the point where a bamboo-

like structure is observed to form in the middle of the nanowire where it is hottest.

2) After recording this current, a simulated temperature profile is then plotted by solving equation (B.1)). (e.g., simulation profile in Figure B.2). From the plot, we are able to obtain a simulation-based T_{GB} at the middle portion of the nanowire (e.g. simulated T_{GB} as shown in Figure B.2).

3) From the TEM study of another nanowire (with almost same diameter and length) annealed in vacuum chamber (Method 1), we obtain the experimental T_{GB} at which a similar bamboo-like structure was observed along the entire length of the nanowire. As such, we can equate the real temperature in the middle of the Joule-heated nanowire to the experimental T_{GB}, by assuming that the transformation is driven primarily by temperature. For example, in Figure B.2, the experimental T_{GB} of the nanowire (40nm in diameter, 10μm in length) using Method 1 is about 1150 K. The simulated profile underestimated T_{GB} by about 200K.

Possible reasons that could have given rise to the difference between the experimental and simulated values include:

a) Non-uniformity of the FEIG nanowire

Since the diameter of FEIG nanowire is non-uniform, the wire cross sections, S, become a variable along the x axis, which is defined as $S(x)$. Here, we consider a

typical case in which the surface of the nanowire follows a sinusoidal profile of the form:

$$S(x) = \pi\left[\frac{r_1 + r_2}{2} + \frac{r_1 - r_2}{2}\sin(\frac{\pi}{l}x)\right]^2, \qquad \text{(B.2)}$$

where r_1, r_2, l are the nanowire maximum radius, minimum radius, and surface wavelength, respectively (as shown in the inset image in Figure B.3). By inserting equation B.2 into B.1, the temperature profile can be expressed as:

$$-\kappa\frac{dT}{dx} = \frac{\rho I^2}{\pi^2\left[\frac{r_1 + r_2}{2} + \frac{r_1 - r_2}{2}\sin(\frac{\pi}{l}x)\right]^4}x, \qquad \text{(B.3)}$$

Figure B.3 shows the simulated temperature curves of nanowires with diameters of 40 ± 4nm, 40 ± 8nm, and 40 ± 12nm. All the curves show local oscillatory behavior and peak temperatures of 980 K, 1050 K and 1250K, respectively. Higher peak temperatures with increasing surface roughness can be interpreted in terms of a reduction in the effective diameter of the nanowire. Compared to the smooth nanowire, the peak temperature is larger by 30K, 150 K and 350K for diameter undulations of ± 4nm, ± 8nm, and ± 12nm, respectively.

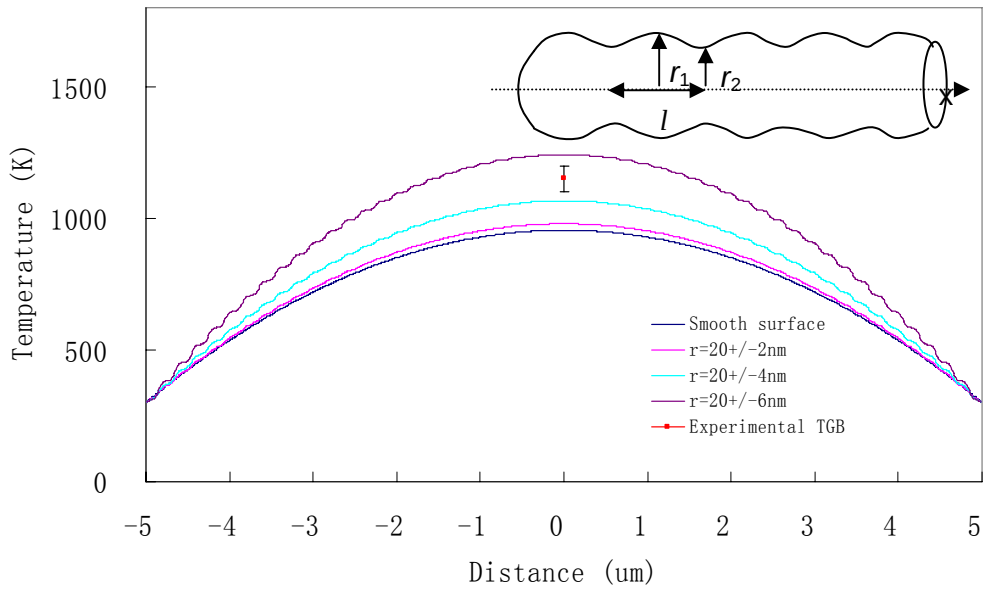

Figure B.3 Temperature profiles along a non-uniform nanowire (inset figure shows a nanowire with sinusoidal variations in radius).

b) Contact thermal resistance

The presence of contact thermal resistance is another possible cause of temperature drops at ends of the nanowire. The contact thermal resistance can be expressed by G_c^{-1}, where G_c is the thermal contact conductance that can be expressed as:

$$G_c = \kappa_c \cdot \frac{S_c}{h_c}, \qquad \text{(B.4)}$$

where S_c, h_c, are contact area and contact thickness between the nanowire and the electrode, respectively, and κ_c is thermal conductivity of the contact.

Meanwhile, the thermal conductance of the nanowire (G_w), can be expressed as:

$$G_w = \kappa \frac{S}{L_w}, \qquad \text{(B.5)}$$

Note that the contact area S_c, is proportional to the nanowire radius R, while the nanowire cross-section is proportional to R^2. Therefore, the ratio of G_c to G_w is proportional to (L_w/Rh_c). For example, in our nanowire of 40nm in diameter and 10μm in length, G_c/G_w is in order of ~10^3. It means that the temperature drop from the end of the nanowire to the Si substrate is in the order of 1K while the temperature difference between the middle and ends of the nanowire is ~1000K. This is consistent with the conclusions reached by others that the contact thermal resistance is not so significant in nanoscale systems compared to macroscale systems [Shi 2003]. Hence, in our simulation, the effect of contact thermal resistance has been ignored.

c) Variability in ρ

Using the Wiedemann-Franz law, Equation. B.1 can be simplified as:

$$-\frac{dT}{dx} = \frac{\rho x I^2}{\kappa S^2} = \frac{\rho^2 I^2}{LS^2} \cdot \frac{1}{T} \cdot x \qquad \text{(B.6)}$$

The temperature profile shown in Figure B.2 is based on the assumption of constant electrical resistivity. In fact, during the annealing process, ρ is expected to be temperature-dependant variable. The resistivity tends to increase with temperature due to electron–phonon interactions.

In present work, temperature dependence of resistivity was obtained by measuring the resistivity of tungsten nanowire through 4-termianl method.

For example, see "line 1" in Figure B.4, at temperature of about 573 K to 1073 K, the resistivity of nanowire of 40nm in diameter can be fit by a linear formula in form of: $\rho = 0.0254T + 31.372$. This relationship was then applied into Equation B.6.

It should be mentioned that measurements (line 1) in Figure B.4 is only taken after nanowire has been annealed at 1073 K for about 30 minutes. This is because that before annealing of nanowire, the temperature dependence appears non-metallic in nature as the temperature is swept up ("line 2" in Figure B.4). This arises from progressive changes in the microstructure as lattice defects are annealed out, thereby improving the electrical conductivity overall. However, above 1073 K, once a quasi-stable configuration (e.g. bamboo-like structure) has been established, (see chapter 4) the resistivity behavior shows no further gross changes when the temperature is swept up or down.

Based on the liner relationship of ρ(T), the temperature profile in nanowires of 40 nm in diameter was then be simulated. (Figure B.5) It can be found that the peak temperature in the profile is about 1085K, much closer to the T_{GB} of 1150K comparing to the simulation based on the constant ρ of 30 μΩ·cm.

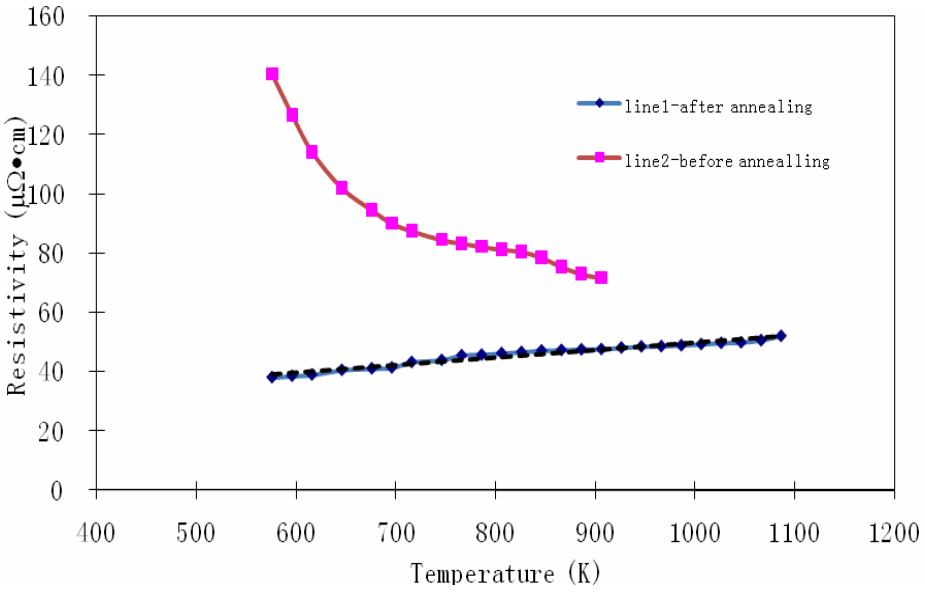

Figure B.4 Relationship between resistivity and temperature *T* reveals the resistivity of tungsten nanowire to be dependent on the microstructure.

B.2 Simulation method

Based on above discussion, it is known that the influence on temperature due to the surface non-uniformity, variable resistivity of nanowire must be taken into account in the simulation of temperature profiles. Assuming the nanowire has a sinusoidal surface and its temperature dependence of resistivity follows a linear function, the temperature along the free-standing nanowire can be calculated by solving EquationS B.3 and B.6. Below are the modified simulation procedures:

1). Under TEM, measure a series of diameter values of the nanowire and calculate a mean diameter and the standard deviation.

2). Find a current value I_0, where a bamboo-like structure forms at the middle of the nanowire.

3). Find the experimental T_{GB} from another nanowire of same specific size by method 1 and then find the linear relationship between temperature and resistivity (ρ(T)).

4). Simulate the temperature profile under I_0 from Equations B.3 and B.6 .

5). Compare the simulation curve with the experimental T_{GB}, record the error between experimental and simulation T_{GB}, which is considered as a systemic error from the measurement.

6). Finally, simulate the temperature profiles at other stress currents and adding in the systemic error to all the profiles.

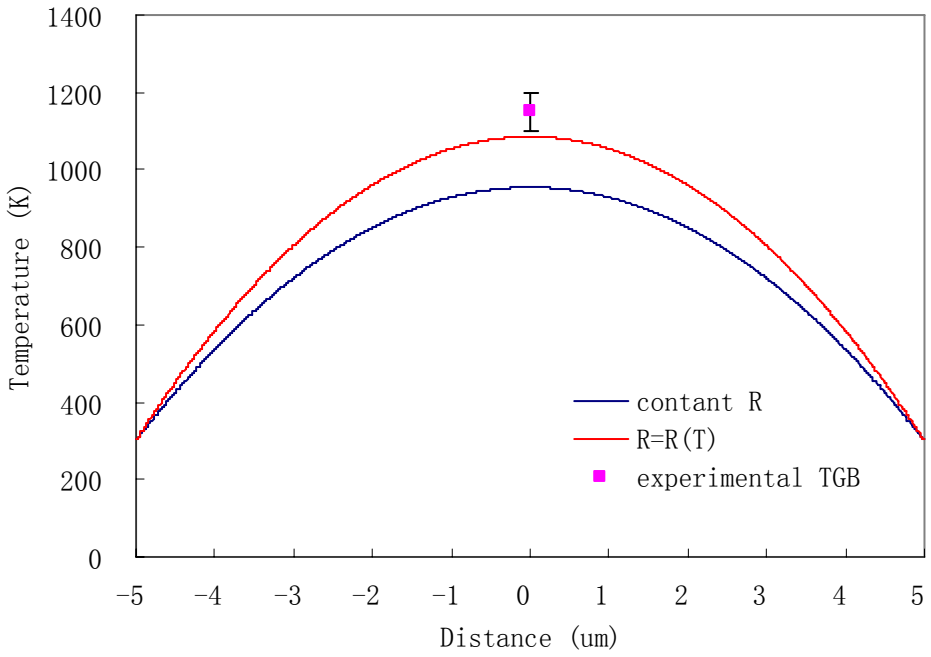

Figure B.5 Temperature profiles for the variable and constant resistivity conditions

Reference

Shi L., Li D. Y., Yu C. G., *et. al*, (2003), *Journal of Heat Transfer* **125**, 881.

Halas S., Durakiewiczt T., (1998), *Vacuum* **49**(4), 331

APPENDIX C – List of Multimedia Files

The video clips are in the CD-ROM provided. The file for the video clip will have a similar name as the appendix.

Movie-1.avi: The video clip shows how a gap (void failure) developing at initial grain boundary site in a W/C cores-shell nanowire due to the electromigration. The W/C nanowire was stressed at a current of 370 μA. The video clip begins after the nanowire has been stressed for about 5 minutes. The electron flow is from right to left with reference to the video. The video frame rate is 0.3 seconds.

Movie-2.avi: The video clip shows the development of grain grooving after the tungsten nanowire (W31) has been stressed at a current of 20μA for 15 minutes. The electron flow is from right to left with reference to the video. The video frame rate is 0.3 seconds.

Movie-3.avi: The video clip shows the development of grain grooving after the tungsten nanowire (W31) has been stressed at a current of 20μA for 20 minutes. The electron flow is from right to left with reference to the video. The video frame rate is 0.3 seconds.

APPENDIX D - Analysis of grain grooving (Klinger and Rabkin's model)

Grain grooving has been widely studied in thin film systems from the beginning of the twentieth century. Until recently, the analyses were mainly based on Mullins' model developed in 1957 [Mullins 1957], and have been verified by experiment observations that grain grooving inhibits the motion of a boundary that terminates on a surface.

In Mullins' definition, we assume the properties of the interface to be independent of their orientation with respect to the adjacent crystals and there is a negligible flow of matter out of the boundary proper. When a polycrystalline metal is hot enough to permit appreciable atomic migration, a grain groove will develop along the line where a grain boundary intersects the surface so that the resultant of the two surface tensions and the grain boundary tension will vanish along the line intersection. The driving force behind the formation of the groove is the tendency of a grain boundary to shrink in order to reduce its area and hence the free energy. The possible transport processes by which the groove may develop are evaporation, surface diffusion and volume diffusion. From his calculation, surface diffusion is the dominant process at the start of grooving (when t, annealing time, is small) [Mullins 1957]. Mullins's theory was initially developed at planar surface and extensively used in simulating grain grooving phenomena in the thin film (2D system) [Dunn 1966, Frost 1990,1992].

Recently, Klinger and Rabkin [Klinger 2005a, 2005b] extended Mullins's model to analyze grain grooving in a thin filament structure by considering the variation of the primary filament diameter in the groove region. Their analysis demonstrated that grain boundary grooving in a thin filament (1D structure) is faster than grooving in a thin-film structure (planar geometry). The lifetime of the filament is shorter by several orders of magnitude compared to thin films. This is a purely geometrical effect associated with the additional curvature of cylindrical filament. For a 1D filament structure, although Mullin's theory can be applied well at the early stages of the grooving process, however, as the groove develops, the variation in the local radius of the deformed cylinder in the groove region becomes increasingly significant. These variations provide an additional driving force for surface diffusion and accelerate the grooving process.

D.1 Klinger and Rabkin's model

In Klinger and Rabkin's analysis, the diffusion flux along the surface, J_s, is driven by the curvature gradient like in the original Mullins' model:

$$J_s = -\frac{\delta_s D_s}{KT}\nabla_s \mu_s = -B\frac{1}{\sqrt{1+(\partial_x R)^2}}\partial_x K \qquad \text{(D.1)}$$

where δ_s, D_s, and μ_s are the thickness of the surface layer in which the diffusion process occurs, the surface diffusion coefficient, and the surface chemical potential, respectively. The shape of the grooved cylinder, which is a body of revolution, can be described by a function *R(x, t)*, where *R* is the cylinder radius, *x* is the distance along

the cylinder axis (x = 0 corresponds to the grain boundary plane), and t is the annealing time. B is the Mullin's coefficient defined according to:

$$B = \frac{\delta_s D_s \Omega \gamma}{kT} \tag{D.2}$$

where Ω is the atomic volume and K is a mean curvature of the cylindrical surface:

$$K = -\frac{\partial_x^2 R}{(1+(\partial_x R)^2)^{3/2}} + \frac{1/R}{(1+(\partial_x R)^2)^{1/2}} \tag{D.3}$$

The kinetic equation for $R(x, t)$ follows the condition of mass conservation:

$$\partial_t R = -\frac{1}{R}\partial_x (R J_s) = -\partial_x J_s - \frac{\partial_x R}{R} J_s \tag{D.4}$$

To solve the equation, we use the following boundary conditions:

$$R(x,0) = R_0 \tag{D.5}$$

(R_0 is the initial radius for unperturbed cylinder)

$$\partial_x R|_{x=0} \equiv m = \tan(\theta_g) \tag{D.6}$$

(θ_g is the equilibrium groove angle)

The surface topography evolution can be described by solving the depth of the groove:

$$h \equiv R_0 - R \tag{D.7}$$

If the groove h is small enough compared to the cylinder radius:

$$h << R_0 \tag{D.8}$$

then:

$$\partial_t h = \partial_s J_s = -B(\partial_x^4 h + \frac{\partial_x^2 h}{R_0^2}) \tag{D.9}$$

Solving Equation (D.9) with the boundary conditions:

$$h|_{t=0} = h|_{x\to\infty} = 0 \tag{D.10}$$

$$\partial_x h|_{x=0} = -m \tag{D.11}$$

$$J|_{x=0} = 0 \tag{D.12}$$

The depth of groove

$$H(t) \equiv R_0 - R(0,t) \tag{D.13}$$

is:

$$H(t) = m(Bt)^{1/4} F_m\left(\frac{(Bt)^{1/4}}{R_0}\right) \tag{D.14}$$

where the function $F_m(u)$ is given by

$$F_m(u) = \frac{2}{\pi}\int_0^\infty \frac{1-\exp(-x^2(x^2-u^2))}{x^2-u^2}dx \tag{D.15}$$

Figure D.1 shows the simulation results based on Equation D.14.

In Equation D.15, if t is small, then $F_m(0) \approx 0.78$ and then

$$H(t) \approx 0.78m(Bt)^{1/4} \tag{D.16}$$

This is identical to the result derived from Mullins' solution for grooving in a planar structure [Mullins 1957]. In this case ($h << R_0$), the depth of groove ($H(t)$) is independent on the cylinder radius R_0, as shown in Figure D.1 below (dashed line).

However, when the annealing time is longer, the simulated groove for a cylindrical wire is much deeper than that for a planar structure (solid line in figure). This suggests that wire break-up can occur much earlier than predicted by Mullin's analysis.

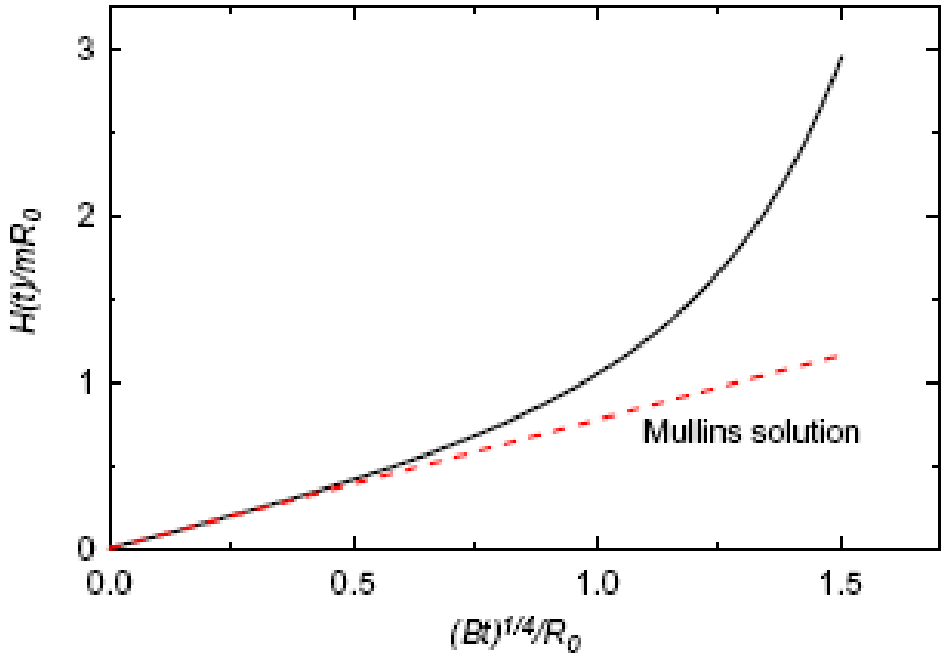

Figure D.1 Deepening kinetic of grain boundary grooves in a filament and in a planar surface [Klinger 2005a]

If the depth of the groove (H) is developed and comparable to the radius of cylinder R_0, under the assumption of small surface slopes with respect to x axis, $\partial_x R \propto m << 1$, Klinger *et al* [Klinger 2005a] used a numerical method to calculate the time dependence of the groove depth up to break-up of the filament. In their solution, Equations (D.1)-(D.4) for the filament radius can be written in the form [Klinger 2005b]:

$$\partial_t R = -\frac{B}{R}\partial_x[R\partial_x(\partial_x^2 R - \frac{1}{R})] \qquad \text{(D.17)}$$

Figure D.2 is result of the calculated time dependence of $R(0,t) = R_0 - H(t)$ for m = 0.15. If annealing time is short ($(Bt)/R_0^4 < 1$), the solution is in good agreement with the original Mullin's solution (D.1) and the shallow-groove approximation (D.14),

respectively. However, if annealing time is longer, ($(Bt)/R_0^4 > 1$) it shows that the "bottleneck" of the filament shrinks much faster.

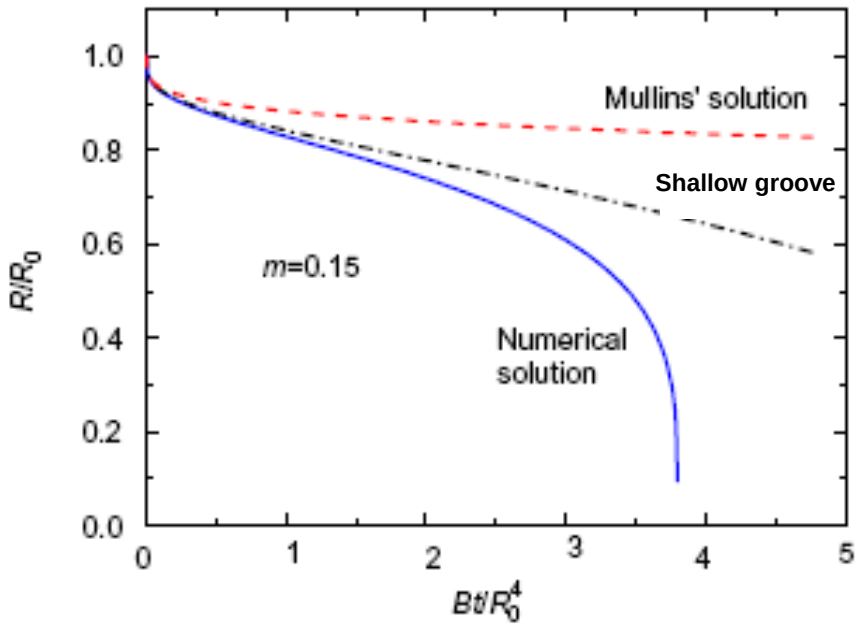

Figure D.2 Deepening kinetic of grain grooves in the filament given by numerical solution, the approximation of shallow grooves and in the initially planar bicrystal [Klinger 2005a].

D.2 Equilibrium state of bamboo-like structure

Based on this numerical solution, for a nanowire consisting of periodic grains with the grain size of radius R_0 and length $2L$ (Figure D.4), Klinger and Rabkin also analyzed its grain groove development for different L/R_0 [Klinger 2005b]. They showed that the equilibrium shape of the bamboo-structure nanowire can be achieved in a specific time (t) only for a certain size:

$$\frac{L}{R_0} \le \left(\frac{L}{R_0}\right)_{\max} \qquad \text{(D.18)}$$

For the condition of:

$$\frac{L}{R_0} > \left(\frac{L}{R_0}\right)_{\max} \qquad \text{(D.19)}$$

the nanowire will break-up in time into individual grains. The maximum ratio $(L/R_0)_{max}$ depends on the equilibrium grooving angle (θ_g) (and hence the m value) at the root of the grain boundary groove. Figure D.5 shows a stability diagram for the nanowire in the "groove angle - grain size" coordinate space [Klinger 2005b]. It can be seen that for $m \rightarrow \infty$, $(L/R)_{\max} \rightarrow \sqrt{3/2}$; for $m \rightarrow 0$, $(L/R)_{\max} \rightarrow \pi$. Figure D.5 shows that an originally uniform cylindrical nanowire with grain size $L/R_0 > (L/R_0)_{max}$ will break up into individual grains while a nanowire with shorter grains ($L/R_0 < (L/R_0)_{max}$) will asymptotical evolve to their equilibrium shape with constant curvature.

Figure D.6 shows a typical time dependence of $R(0)/R_0$ for different grain aspect ratio L/R_0 corresponding to points 1, 2, 3 & 4 in Figure D.5. For a grain whose aspect ratio is in the stable region (Point 1), $R(0)$ decreases with time and asymptotically approaches its equilibrium value. In contrast, for a grain whose aspect ratio is outside of the stable region (Points 2-4), $R(0)$ rapidly decreases until the nanowire breaks up. The larger the aspect ratio, the shorter the break-up time.

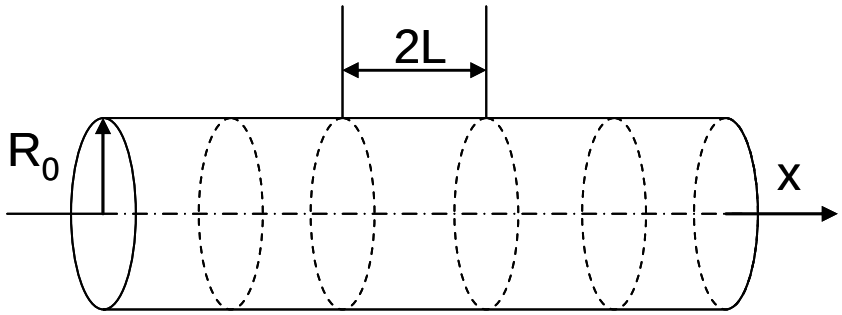

Figure D.4 Schematic of bamboo-like polycrystalline cylindrical nanowire of initial radius R_0 and grain length $2L$.

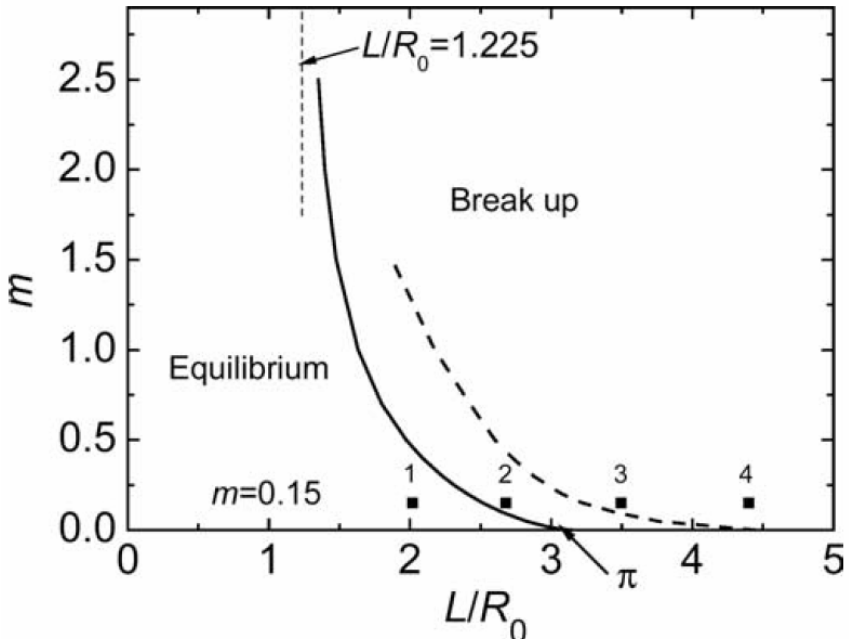

Figure D.5 Stability diagram of a nanowire. $m = \tan(\theta_g)$, L/R_0 represents the aspect ratio of the grain. [Klinger 2005b]

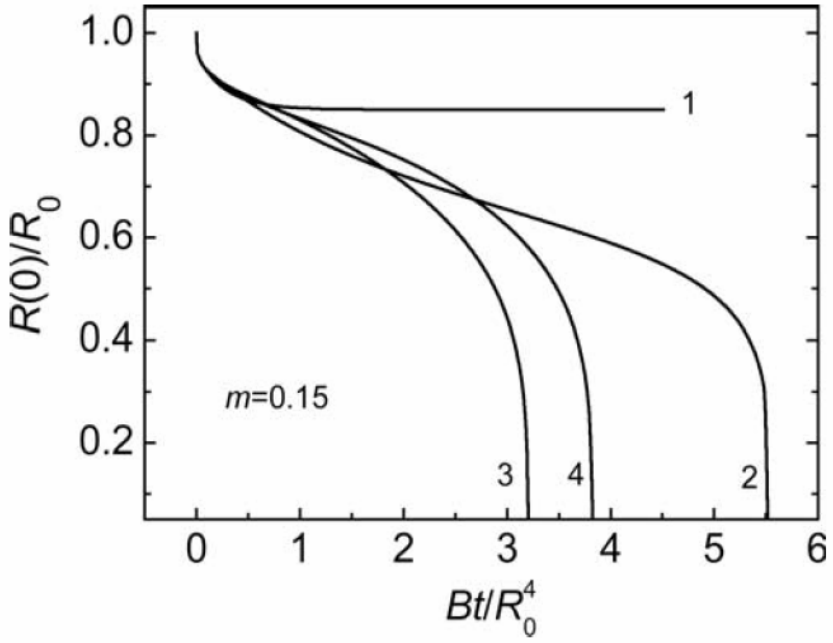

Figure D.6 Kinetic of thinning and break-up of nanowire with different grain aspect ratios. [Klinger 2005b]

References

Dunn C. G., (1966), *Acta Metall.* **14**, 221.

Frost H. J., Thompson C. V., Walton D. T., (1990), *Acta Metall*. **38**, 2455.

Frost H. J., Thompson C.V., Walton D. T., (1992), "*Grain Growth in Polycrystalline Materials"*. ed: Abbruzzese and Brozzo. Trans Tech Publns. 543.

Klinger L., Rabkin E., (2005a), *Scripta Materialia* **53,** 229.

Klinger L., Rabkin E. (2005b), *Z Metallkd* **96**(10), 1119.

Mullins W. W., (1957), *J. Appl. Phys.* **28**(3), 333.

Mullins W.W., (1958), *Acta. Metall.* **6**, 414.